NTNU
Det skapende universitet

Oppførsel av plastmaterialer ved lave temperaturer

Andreas Myrang

Bygg- og miljøteknikk
Innlevert: juni 2016
Hovedveileder: Arild Holm Clausen, KT

Norges teknisk-naturvitenskapelige universitet
Institutt for konstruksjonsteknikk

Department of Structural Engineering
Faculty of Engineering Science and Technology
NTNU- Norwegian University of Science and Technology

ACCESSIBILITY

OPEN

MASTER THESIS 2016

SUBJECT AREA:	DATE:	NO. OF PAGES: 99
Polymer engineering	09 June 2016	73 + 26

TITLE:

Behavior of thermoplastics at cold conditions

Oppførsel av termoplast i kaldt klima

BY:

Andreas Myräng

SUMMARY

The physical response of a polypropylene compound has been studied for a range of initial temperatures (-30 to $25℃$) and strain rates (10^{-2} to $1\ s^{-1}$) in uniaxial tension, to investigate the topic of material response in cold climates. Experiments were carried out using a Polycarbonate chamber and liquid nitrogen injections to imitate a cold climate, with benchmarking to verify applicability of the test rig. Deformation history was recorded with digital cameras, using digital image correlation to calculate strains.

Numerical simulations were carried out in an attempt to verify material testing. Simulations were performed with finite element software Abaqus, using an axisymmetric, dynamic explicit model and using a polymer material model produced by the Structural Impact Laboratory (SIMLab) at NTNU.

Material testing results experienced reduced cold drawing and early fracture at low initial temperature and high strain rate. Numerical simulations did not coincide with laboratory tests results mainly due to an assumption of constant plastic dilatation.

RESPONSIBLE TEACHER: Professor Arild H. Clausen

SUPERVISOR(S): Arild H. Clausen, Joakim Johnsen

CARRIED OUT AT: Department of structural engineering, NTNU

MASTER THESIS 2016

Andreas Myräng

Behaviour of thermoplastics at cold conditions

(Oppførsel av plastmaterialer ved lave temperaturer)

This master's thesis is related to an ongoing PhD project on behaviour and numerical modelling of thermoplastics at low temperatures, i.e. from 25°C down to –30°C. The knowledge about the physical behavior and appropriate material models for polymers at such conditions is limited. This calls for a research activity including material tests at different temperatures, calibration of the parameters in a material model, and validation of the model against tests involving a combined stress state.

A major challenge is to do low-temperature tests facilitating instrumentation with digital cameras for subsequent determination of the deformation of the sample with digital image correlation (DIC). It is also desirable to monitor the sample with an infrared camera in order to measure any adiabatic heating during the test. A promising approach is to cover the test sample in a chamber made of polycarbonate. An important part of the work is thus to demonstrate the applicability of this test set-up. A polypropylene (PP) material is selected for the study in this thesis.

Possible keywords for activities in this master thesis research work may include:

- Literature: Polymers in general, material models, response at cold conditions
- Test rig: Applicability of the test rig for material tests.
- Material tests: Uniaxial tension tests at different temperatures and possibly rates.
- Calibration: Identify the coefficients of a material model.
- Benchmark tests: Tests involving a combined stress and strain state.
- Validation: Simulation of benchmark tests and evaluation of the model.

The candidate may agree with the supervisors to pay particular attention to specific parts of the investigation, or include other aspects than those already mentioned.

The thesis is to be organized as a research report, recognising the guidelines provided by Department of Structural Engineering.

Supervisors: Joakim Johnsen and Arild Holm Clausen

The report is to be handed in not later than 11 June 2016.

NTNU, 12 January 2016

Arild Holm Clausen

Acknowledgements

With no previous experience in neither DIC nor eCorr, several questions and problems arose during my work with the software. I would like to thank Egil Fagerholt for his feedback and assistance with eCorr, making discretization much less troublesome. For calibrating the material model parameters and for his assistance with Abaqus simulations, I express gratitude towards associate professor David Morin.

My work with the thesis has been outstandingly well paced due to good planning and timely feedback from my supervisor Arild Holm Clausen. I thank you for your assistance, your excellent guidance of my thesis and for making my last semester at NTNU highly enjoyable.

I would like to thank Andreas Vestermo Nesje and Pål Arild Nilsen for their assistance with proofreading, discussions on mechanical theory and recommendations regarding numerical simulations.

Finally, for his continuous and invaluable assistance throughout the entire semester, I would like to thank PhD. candidate Joakim Johnsen. Your patience and assistance with my questions and constant requests for feedback is highly appreciated.

Abstract

The physical response of a polypropylene compound has been studied for a range of initial temperatures (-30 to 25℃) and strain rates (10^{-2} to $1\ s^{-1}$) in uniaxial tension, to investigate the topic of material response in cold climates. Experiments were carried out using a Polycarbonate chamber and liquid nitrogen injections to imitate a cold climate, with benchmarking to verify applicability of the test rig. Deformation history was recorded with digital cameras, using digital image correlation to calculate strains.

Material specimen became stronger and more brittle when reducing initial temperature. Higher initial strain rates caused increased yield strength, but lowered plastic strength due to specimen heating. At combinations of low initial temperatures and high initial strain rates, specimens would experience a clear reduction in cold drawing with early fracture of the initial neck in the specimen gauge. The phenomena caused a reduction in longitudinal strain and strain hardening compared to other material tests with no reduction in cold drawing. Suggested explanations for the phenomena are localized temperature softening in the initial neck and crazing.

Numerical simulations were carried out in an attempt to verify material testing. Simulations were performed with finite element software Abaqus, using an axisymmetric, dynamic explicit model and using a polymer material model produced by the Structural Impact Laboratory (SIMLab) at NTNU. Simulations and material testing results mostly agree until the material reach large plastic strains; both stress and volumetric strain curves coincide for initial plastic deformations, but diverge when approaching failure. The divergence is caused by the assumption of constant plastic dilatation in the SIMLab polymer model, which does not account for the large increase in contraction ratio as the material elongates. Simulation accuracy is expected to improve significantly by including a variable plastic dilatation parameter.

Sammendrag

Fysisk oppførsel for en polypropylen polymersammensetning har blitt testet for varierende initial temperatur (-30 til $25℃$) og tøyningsrate (10^{-2} til $1\ s^{-1}$) i enaksiellt strekk, for å studere materialrespons i kaldt klima. Eksperimentene ble utført i et Polykarbonat kammer, med injeksjoner av flytende nitrogen for å imitere kaldt klima. Benchmark tester ble utført for å teste nøyaktigheten av oppsettet. Deformasjoner ble målt ved bruk av digitale kamera, og digital bildekorrelasjon ble benyttet for å regne ut tøyning.

Prøvestykkene ble sterkere og mindre duktil når initial temperatur ble redusert. Økning av initial tøyningsrate ga høyere flytespenning, men reduserte plastisk styrke grunnet oppvarming av prøvestykket. Kombinasjoner av lav initialtemperatur og høy initial tøyningsrate ga en betydelig reduksjon i kaldtrekking og tidlig brudd av initial neck. Dette fenomenet forårsaket en reduksjon i både langsgående tøyning og tøyningsherdning sammenlignet med andre tester uten reduksjon i kaldtrekking. Temperaturmyking og crazing er foreslått som årsak til fenomenet.

Numeriske simuleringer ble utført for å verifisere resultater fra materialtestene. Simuleringene ble utført i elementmetodeprogrammet Abaqus, og brukte en aksesymmetrisk, dynamisk eksplisitt modell, samt en polymer materialmodell produsert av Structural Impact Laboratory (SIMLab) ved NTNU. De fleste numeriske simuleringer ga like resultater som materialtester frem til store plastiske tøyninger. Både spenning- og volumtøyningskurver sammenfalt i elastisk og tidlig plastisk område, men divergerer når kurvene nærmer seg brudd. Divergensen er forårsaket av at polymermodellen antar konstant plastisk dilatasjon, når materialet i realiteten har stor endring i tverrtøyningsratio med deformasjon. Ved å inkludere en variabel plastisk dilatasjonsparameter forventes det at nøyaktigheten av simuleringene forbedres betydelig.

Contents

1 Introduction

In relation to an ongoing PhD project at NTNU, this thesis studies the development of material behavior of polypropylene at cold conditions, i.e. below room temperature. Polymers are becoming an increasingly common material for construction purposes, also in northern regions were temperatures approaching minus thirty degrees are common. Understanding how polymers behave when the temperature drops is key. When used for protective purposes, such as pipeline coating, the influence of strain rate on material behavior also becomes relevant.

While the effect of both temperature and strain rate on mechanical behavior polymers have been studied broadly, knowledge of the physical behavior of semi-crystalline polymers at low temperature is somewhat limited. Relevant studies tend to focus on glassy polymers [1-4]; although related to semi-crystalline polymers, their material behavior becomes quite different at certain temperatures. More directly applicable studies include Chou et al.[5] and Jang et al.[6], the latter studying several aspects of material behavior of rubber-modified polypropylene at a wide range of both temperatures and strain rates.

Material testing herein is performed in uniaxial tension. Tests aims to verify suitability of using polypropylene in cold climates and provide an understanding of material behavior with changing temperature and strain rate. In addition to discerning material behavior, another objective of this thesis has been to verify accuracy of the material testing setup. The polymer studied, named Borcoat EA165E, is an elastomer modified polypropylene compound for use in injection molding of steel pipe coating. Primary strength of the compound lies in good impact resistance at low temperature, making the material suitable for pipe coating in cold climates [7].

Material testing was performed using digital image correlation (DIC) to capture deformations of tensile test specimens and an Instron controller to measure forces. Testing at low temperatures required a complicated test setup, including a polycarbonate (PC) chamber with a liquid nitrogen supply and more robust specimen coating. Verifying suitability and accuracy of the test setup was key for comparing material test at- and below room temperature.

Numerical simulations in ABAQUS were used to verify uniaxial tensile test results. The simulations used a polymer material model developed at SIMLab, NTNU, calibrated for each testing temperature. The model allows for modelling of relevant mechanisms in drawing, specifically strain hardening, strain softening, damage and adiabatic heating.

2 Material description and theory

The polypropylene studied (Borcoat EA165E) is an elastomer modified semi-crystalline polymer. Relevant aspects regarding the mechanical and thermal behavior of polypropylene - and semi-crystalline polymers in general - is presented in this chapter.

2.1 Polypropylene

Polypropylene, abbreviated PP, is a thermoplastic polymer. Like all thermoplastics, polypropylene consists of several identical monomers connected together to form long chains (Figure 1). The monomers of PP is propylene, also called propene. The polymer chain is created by homopolymerization of propylene [8].

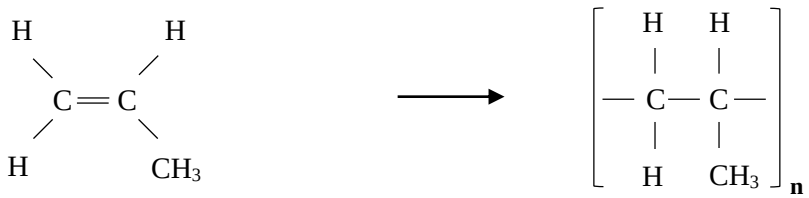

Propylene (C_3H_6) Polypropylene $(C_3H_6)_n$

Figure 1. Polymerization of propylene. PP consists of long hydrocarbon chains, with methyl side groups.

The mechanical properties of thermoplastic polymers is dependent on several aspects other than the type of polymer. The morphology of the polymer is one such aspect, and it describes the structure of the polymer chains after processing (production). In a melted state, polymers are composed of long chains in an irregular, entangled pattern. When cooled to a solid state the polymer may either retain the irregular pattern and become amorphous or form a folded, aligned chain pattern and become crystalline. The aligned regions, called lamellae, are held together by various van der Waals forces, i.e. intermolecular bonds [8, 9].

Under normal conditions, crystallization in polymers is not perfect and amorphous regions still exist in all polymers to some degree [9, 10]. Polymers that crystallize are thus described as semi-crystalline and are characterized by degree of crystallinity, typically in the range of 40-75% [10]. Together, the lamella and amorphous regions in semi-crystalline materials create larger structures called spherulites (Figure 2) [9, 10].

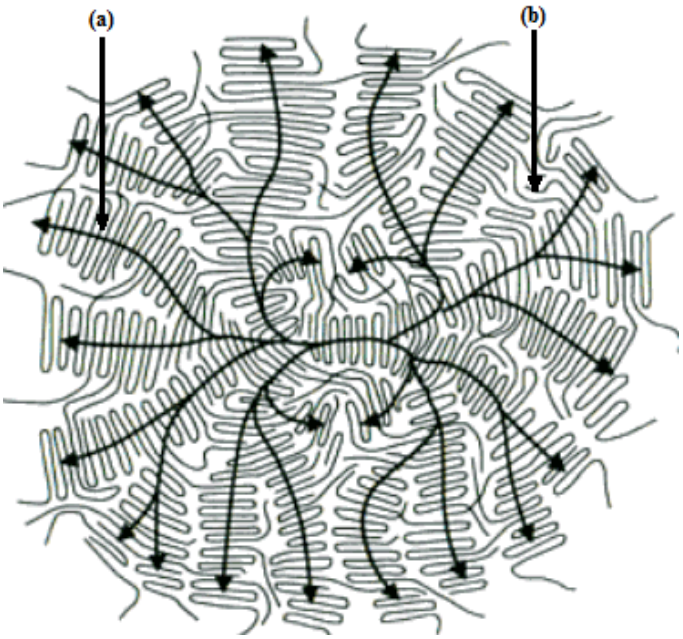

Figure 2: Polymer spherulite. Crystalline regions consist of folded chains, called lamellae (a), with amorphous regions, (b), separating them [11].

2.2 Thermal properties

Semi-crystalline thermoplastics have three states of material behavior, dependent on temperature. As the material temperature increases, thermoplastics transition from the brittle glassy state, to the rubbery state and finally the viscous liquid state (Figure 3). The states are not related to the true phase transitions: liquid, solid and gas [12], rather they describe the change in material properties as the material changes temperature. The glass-transition temperature range, T_G, marks transition between the glassy and rubbery state. Similarly, the transition between the rubbery state and viscous state is marked by the melting temperature T_m [8, 9].

The states yield different mechanical properties, the most relevant being material stiffness. As the polymer transitions between states the Young's modulus drastically decrease, marking a significant change in material behavior. Material stiffness is also temperature dependent within each state. The plateaus correspond to the glassy and rubbery state respectively.

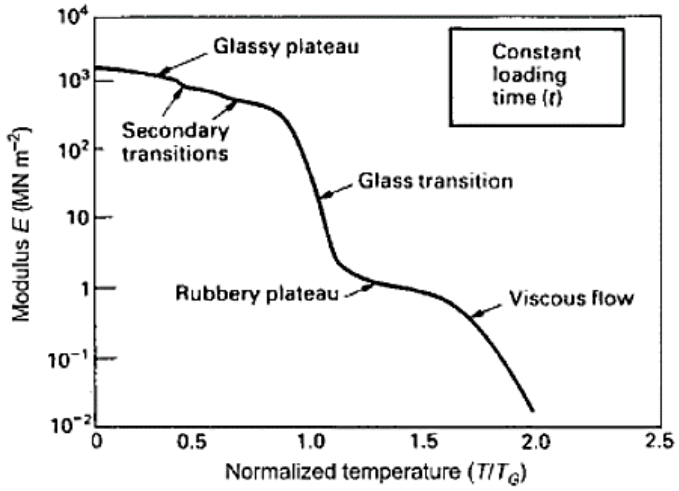

Figure 3. Schematic showing change in Young's modulus with temperature. Increasing the temperature yields lower stiffness. Significant change in stiffness during transitions [8].

During the glass transition ($T = T_G$) the secondary bonds within the amorphous regions of the material will melt, allowing the molecular chains to move relative to each other. The transition effectively softens the material, reducing stiffness and density while increasing ductility. Following the glass transition the material passes through a rubber-elastic state, before arriving at the melting temperature, T_m, which marks the transition to viscous flow [9].

Elastomer modification refers to the addition of an elastomer in the PP polymer blend. As advertised [7], the elastomer modification should provide better impact resistance at lower temperatures. More specifically, the elastomer reduces the glass transition temperature of the material, ensuring that the specimen remains within the rubbery regime for all material test performed in this thesis.

2.3 Mechanical behavior

Describing mechanical behavior of semi-crystalline polymers is complicated as many of the deformation mechanisms are simultaneous or competing. Semi-crystalline polymers consist of both amorphous and crystalline regions and the total material response include mechanisms from each. Total deformation response in the glassy regime may be viewed as stretching two intermingling networks of crystalline lamellae and the amorphous phase [13-15].

Polypropylene is classified as a tough plastic (Figure 4) as long as it remains within the glassy regime [10]. In addition to initial elastic stiffness, the plastic behavior of polymers also depend on temperature regime, including ultimate strength, draw ratio, and failure type.

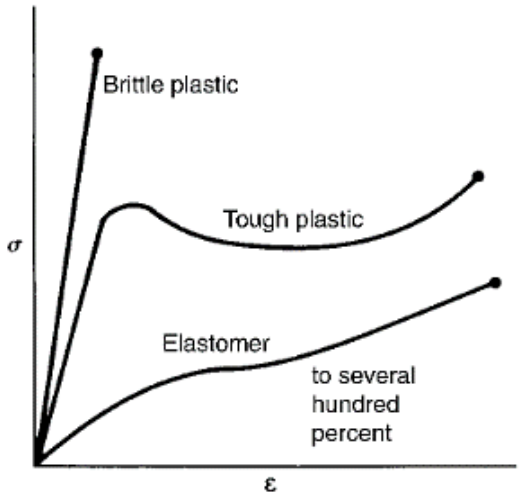

Figure 4: Stress-strain behavior of three types of polymeric materials. Polypropylene is a tough plastic, with a lower initial stiffness than brittle plastics and substantially larger plastic deformation [10].

The stress-strain behavior of a tough plastic follows a typical progression. Initial deformations are elastic until the material can no longer sustain the level of stress, at which point the material becomes unstable and yields [16]. During yielding, the material will plastically deform at the point with the highest stress concentration. This phenomena is referred to as necking, observable as a slight narrowing of material test specimen cross section. After yielding, the material generally undergoes substantial plastic deformation at almost constant engineering stress, where the neck propagates over the length of the test specimen. Neck propagation and corresponding specimen elongation is referred to as cold drawing. [8, 10, 17].

In semi-crystalline polymers, drawing constitutes a thorough reorientation of polymer chains. As the material draws, the neck propagates by shear yielding of the cross section adjacent to the initial neck. Necking by shear yielding orients polymer chains in the draw direction and breaks the spherulittic structure, reducing the number of chain folds [10, 17]. The process effectively strain hardens the material were the new, oriented fibrils with more tie molecules provides increased strength in the drawn direction (Figure 5).

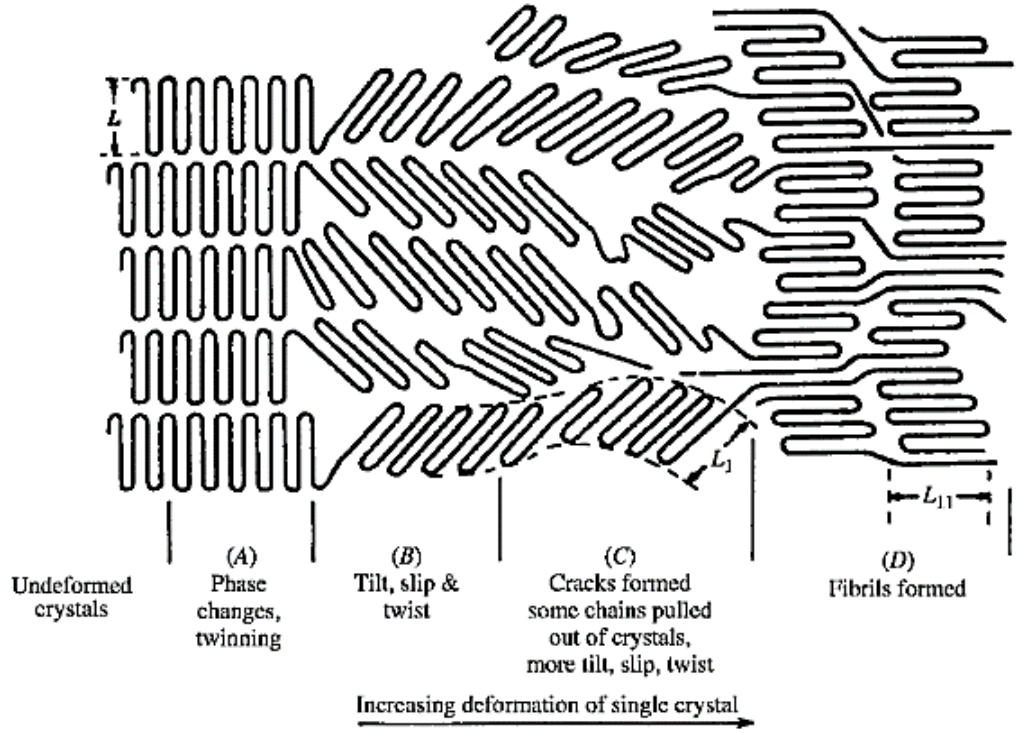

Figure 5: Realignment of crystalline structure by shear yielding. Necking results in polymer chain orientation in the draw direction [10].

A semi-crystalline polymer will generally undergo both intrinsic strain softening and strain hardening during plastic deformation. Intrinsic strain softening occurs immediately after yielding, causing a slight decrease in stress with increasing deformation and may be observed as a 'dip' in the stress-strain curve [18, 19]. The process is followed by strain hardening where the material becomes stronger with increasing plastic deformation due to polymer orientation in the draw direction [17, 20].

Crazing, cavitation and stress whitening

At certain ranges of temperature and strain rate, polymers may be subjected to crazing. A craze refers to the formation of microscopic voids in the material, caused by stress concentrations from imperfections such as flaws, cracks, particles etc. Crazes generally form perpendicular to the draw direction, with ligaments of oriented polymer chains holding material together despite the void space (Figure 6) [10]. Crazing is considered a precursor to fracture when it serves as the dominant deformation mechanism, generally noted brittle since crazing is highly localized [21]. Sufficient crazing may eventually cause crack formation and –nucleation, resulting in material failure [3, 4, 8, 22].

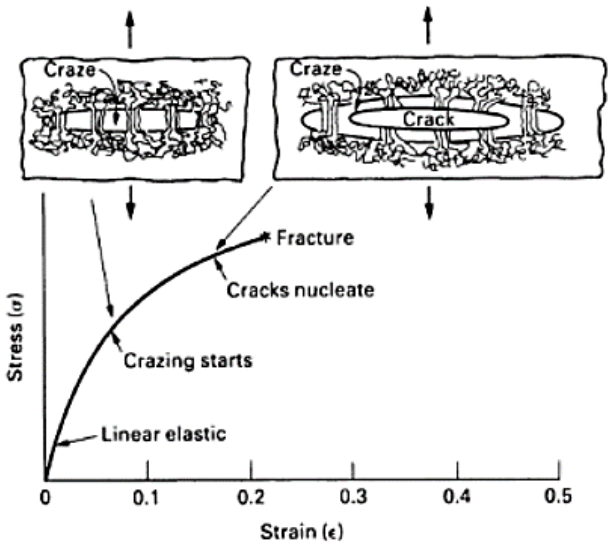

Figure 6: Crazing in a linear polymer. Crazes form as void space between fibrils of oriented polymer chains, perpendicular to the draw direction [8].

Cavitation refers to the formation of cavities (voids) in the material, formed only in drawing and never in compression or shearing [23, 24]. They form in the amorphous phase of the material when crystal plasticity is sufficiently high, and generally initiate close to yielding [15, 23]. Similar to crazing, cavities form voids inside the material but unlike crazing they are not connected by fibrils and do not transfer stresses. Cavities form as void space and elongate in the draw direction and may be mistaken for crazes, especially at large strains [23].

Stress whitening is a consequence of the formation and development of crazes and cavities in the material, their light-scattering effects causing a whiter appearance [10, 22]. Although it might not directly cause material fracture, crazing or cavitation (or both) are usually present in the material to some degree, easily observable as whitening of the material.

Shear yielding

Shear yielding constitutes one of the polymer strength limitation in tension, competing with crazing and void formation [21, 23]. In semi-crystalline polymers, shear yielding takes place in the form of slip, twinning and martensitic transformation of the crystal lamellae [3, 21]. Shear deformation leads to change of material shape with little change in volume, thus shear yielding itself causes little change in volume [21]. Conversely, crazing and cavitation are dilatational, forming voids in the material, and causes increasing volume [21, 23, 24]. Polymers will

generally exhibit either a ductile or a brittle response, with crazing related to brittle failure and shear yielding and cold drawing related to ductile failure.

2.4 Strain rate and temperature dependence

Mechanical behavior of most polymers is highly dependent on both the strain rate and temperature during testing [2, 25, 26]. In general, higher strain rates elevate material stiffness and increases both polymer yield stress and initial Young's modulus. Another consequence of increasing strain rate is material heating. Due to the low thermal diffusivity of most thermoplastics [2], higher strain rates may cause a significant temperature increase as the material is elongated.

In addition to strain rate affecting temperature during testing, the initial temperature is also highly relevant. Material behavior becomes increasingly ductile with increasing temperature, causing lower yield stress and stiffness while increasing draw ratio [9]. Large changes in initial temperature and strain rate might cause the material to transition between glassy, rubbery or viscous states during drawing.

The failure mechanisms discussed in chapter 2.3, i.e. crazing, cavitation and shear yielding are all dependent on initial strain rate and -temperature. In tensile deformation studies of polypropylene by Jang et al. [6], it was summarized that high temperature and low strain rate encourage shear yielding with ductile fracture, while low temperature and high strain rate encourage crazing with brittle fracture. Similar trends have been reported for cavitation by Pawlak et al. [23, 24], presenting cavitation as a competition to crystal plasticity. Therein, high strain rates and low initial temperatures reportedly increased the stress at which plastic deformations of crystals occur, which caused the amorphous phase to break instead and resulted in cavitation. Accordingly, material tests of Borcoat PP are expected to form cavitations, with possible crazing under brittle testing conditions.

3 Material model

For calculation and numerical simulation purposes, this thesis uses a material model developed for brittle and ductile polymeric materials, produced by the Structural Impact Laboratory (SIMLab) at NTNU [27]. The model has several features included in the material model, but not all of them are relevant for this project. Utilized features of the material model is presented in this chapter.

The rheological model for uniaxial stress consists of a series connection with a viscoelastic region (left) and viscoplastic region (right) (Figure 7). The viscoelastic region consists of a linear elastic spring with stiffness E_0, and N_M number of Maxwell elements with linear spring stiffness E_α and relaxation time τ_α. The viscoplastic region consists of a friction element to represent yielding and isotropic hardening, $\sigma_T + R$, a nonlinear spring to represent kinematic hardening, χ, and a nonlinear dashpot to represent viscous stress, σ_v.

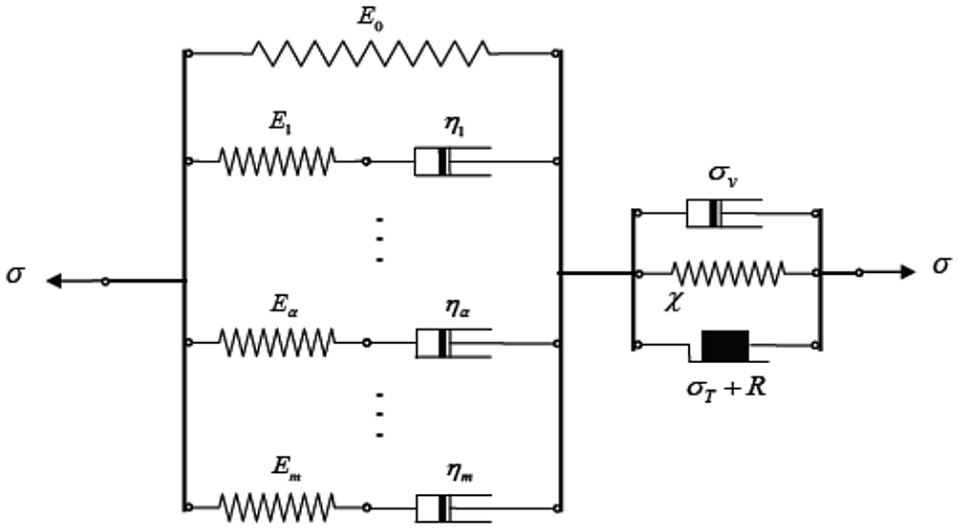

Figure 7: Rheological illustration of the constitutive model.[27]

Using additive strain decomposition, the total strain in the model may be expressed as:

$$\varepsilon = \varepsilon^e + \varepsilon^p \tag{3.1}$$

Where ε is the total strain, ε^e is the viscoelastic strain and ε^p is the viscoplastic strain. Similarly, the viscoelastic strain in each Maxwell element can be decomposed into an elastic and inelastic part:

$$\varepsilon^e = \varepsilon_\alpha^e + \varepsilon_\alpha^i \tag{3.2}$$

Where ε_α^e and ε_α^i expresses the elastic and inelastic strain in Maxwell element α.

3.1.1 Viscoelasticity

The elastic behavior of the model is described using Maxwell elements as illustrated in the rheological model. The viscosity of dashpot α may be expressed as:

$$\eta_\alpha = E_\alpha \tau_\alpha \tag{3.3}$$

Yielding the stress distribution in the elastic part:

$$\sigma = \sigma_0 + \sum_{\alpha=1}^{N_M} \sigma_\alpha \quad \text{where} \quad \begin{cases} \sigma_0 = E_0 \varepsilon^e \\ \sigma_\alpha = E_\alpha \varepsilon_\alpha^e = \eta_\alpha \dot{\varepsilon}_\alpha^i \end{cases} \tag{3.4}$$

Where σ_0 is the stress in the linear spring and σ_α is the stress in Maxwell element α. Herein, only the elastic part used, i.e. the material is modeled as linear elastic.

Yield function

To model the influence of pressure on the yield behavior of polymers, the Raghava yield criterion is used. This yield criterion is a modified von Mises yield criterion that accounts for the effect of pressure on yield strength [28]. The criterion may be written as:

$$(\sigma_1 - \sigma_2)^2 + (\sigma_2 - \sigma_3)^2 + (\sigma_3 - \sigma_1)^2 + 6(C - T)\sigma_m = 2CT \tag{3.5}$$

Where σ_1, σ_2, σ_3 are principal stresses, σ_m is the mean stress and C and T are the absolute values of the compressive and tensile yield strength, respectively.

The criterion can be simplified by introducing the total stress invariant, I_1, the deviatoric stress invariant, J_2 and the pressure sensitivity α:

$$I_1 = \sigma_1 + \sigma_2 + \sigma_3 \tag{3.6}$$

$$J_2 = \frac{1}{6}[(\sigma_1 - \sigma_2)^2 + (\sigma_2 - \sigma_3)^2 + (\sigma_3 - \sigma_1)^2] \tag{3.7}$$

$$\alpha = \frac{C}{T} \tag{3.8}$$

Using the expressions in equations (3.6) to (3.8), the Raghava yield function may be written as:

$$f(I_1, J_2) = \alpha T^2 - (\alpha - 1) I_1 T - 3J_2 \tag{3.9}$$

Solving for the tensile stress yields an expression for the Raghava equivalent stress:

$$\sigma_{eq} = \frac{(\alpha - 1) + \sqrt{(\alpha - 1)^2 I_1^2 + 12 J_2 \alpha}}{2\alpha} \tag{3.10}$$

If the material exhibits no pressure sensitivity ($\alpha = 1$), the equation reduces to the von Mices yield criterion.

Contraction ratio

In this material model, the contraction ratio is an elastic parameter and may be written as:

$$\nu = -\frac{\varepsilon_T}{\varepsilon_L} \tag{3.11}$$

Where ε_T and ε_L is the transverse and longitudinal strain, respectively.

3.1.2 Viscoplasticity

The yield function for the material model may be written as:

$$f = \sigma_{eq} - (\sigma_T + R) \tag{3.12}$$

Where σ_{eq} is the Raghava equivalent stress, σ_T is the yield stress in uniaxial tension and R is the isotropic hardening variable. This equation determines the onset of yielding and current domain of the material:

$$f \leq 0 \ \rightarrow \text{Elastic domain}$$

$$f > 0 \ \rightarrow \text{Plastic domain}$$

In the plastic domain, the yield function is strain rate dependent and the constitutive relation must account for the viscous stress: σ_v . Herein, the Johnson cook flow stress model is used [29, 30]:

$$\sigma_{eq} = [\sigma_T + R]\left[1 + C \ln\left(\frac{\dot{p}}{\dot{p}_0} + 1\right)\right] \tag{3.13}$$

Where C is rate sensitivity of the material, $\dot{p}$ is the equivalent plastic strain rate and $\dot{p_0}$ is the reference plastic strain rate. Temperature sensitivity is not included for the flow stress. It is accounted for by calibrating work hardening parameters for each initial temperature.

The non-associative flow rule is used to estimate the equivalent plastic strain. On tensor form, the expression for the plastic flow rule may be written as:

$$\dot{\varepsilon}_{ij} = \dot{\lambda}\frac{\partial g}{\partial \sigma_{ij}} \tag{3.14}$$

The plastic flow potential g is identical to the Raghava yield function (3.10), apart from pressure sensitivity α. Instead of pressure sensitivity, the flow potential accounts for volumetric plastic strain through the dilatation parameter β_D. The flow potential is defined as:

$$g = \frac{(\beta_D - 1) + \sqrt{(\beta_D - 1)^2 I_1^2 + 12 J_2 \beta_D}}{2\beta_D} \tag{3.15}$$

The dilatation parameter $\beta_D \geq 1$ controls the volumetric strain. Isochoric plastic behavior is obtained when $\beta_D = 1$. Similarly, associated flow ($g = f$) is obtained if $\beta_D = \alpha$. For positive plastic dissipation to occur, α must be larger than β_D, yielding an upper limit to the plastic dilation in addition to the lower limit.

Work hardening

The material model uses the Voce rule to calculate the hardening variable, which may be written as [31]:

$$R = \sum_{i=1}^{N_R} R_i = \sum_{i=1}^{N_R} Q_{Ri}\left(1 - \exp\left(-\frac{\theta_{Ri}}{Q_{Ri}}\right)p\right) \tag{3.16}$$

Where N_R is the number of isotropic hardening terms ($N_R \leq 3$ in the model), Q_{Ri} is the saturation value of R_i, θ_{Ri} is the initial hardening modulus and p is the accumulated plastic strain. The different R_i terms describe hardening, softening and re-hardening of the material, depending on the sign of θ_{Ri} and Q_{Ri}. Hardening occurs when $\theta_{Ri} > 0$ and $Q_{Ri} > 0$ and softening when $\theta_{Ri} < 0$ and $Q_{Ri} < 0$, both with an initial slope θ_{Ri} and saturation value Q_{Ri}.

3.1.3 Damage

The material model accounts for ductile damage and fracture. Damage may be either uncoupled or coupled depending on whether the volumetric strains are small or large, respectively.

Uncoupled damage only affects the constitutive equation at fracture. Coupled damage results in a softening of the material as the damage increases.

Coupled damage is modeled by substituting the stress tensors $\boldsymbol{\sigma}$ with an effective stress tensor:

$$\boldsymbol{\sigma} \rightarrow \frac{\boldsymbol{\sigma}}{1 - D} \tag{3.17}$$

Where D is the damage variable, $0 \leq D < 1$. The effective stress tensor replaces the stress tensor in all constitutive equations.

Ductile damage

If the plastic flow rule g is modeled with dilatation, i.e. $\beta > 1$, the material will expand during plastic flow. This will decrease material density and might cause material softening. Ductile damage may be written as:

$$D = 1 - (1 - D_I)\exp(-\varepsilon_{vol}^{p}) \tag{3.18}$$

Where D_I is the initial damage and ε_{vol}^{p} is the volumetric plastic strain, expressed as:

$$\varepsilon_{vol}^{p} = \int_0^t \dot{\boldsymbol{\varepsilon}}^{\boldsymbol{p}}\, dt = \varepsilon_1^p + \varepsilon_2^p + \varepsilon_3^p \tag{3.19}$$

The damage evolution is entirely dependent on the flow rule, and will not occur if the plastic flow is isochoric ($\beta = 1$). Damage propagation only occurs in the plastic domain.

Fracture

Failure by fracture occurs when the damage variable D reaches a critical value $D_C < 1$ in an integration point. The stress tensor at this point is set to zero and may no longer carry any load. The fracture criteria is defined as:

$$D = D_C$$

3.1.4 Adiabatic heating

The mechanical energy from plastic deformation will transform partially into heat, and may cause a noticeable increase in temperature. The rise in specimen temperature given adiabatic conditions may be written as [30, 32]:

$$\dot{T} = \beta_T \frac{\sigma_{ij}\dot{\varepsilon}_{ij}^{p}}{\rho C_p} \tag{3.20}$$

Where β_T is the Taylor-Quinney coefficient, ρ is the material density and C_p is specific heat capacity. By using the energy conjugate, the numerator may be expressed using the equivalent stress and plastic strain rate $\dot{p}$:

$$\sigma_{ij}\dot{\varepsilon}_{ij}^{p} = \sigma_{eq}\dot{p} \tag{3.22}$$

The material model is used in numerical calculations with Newton Raphson iterations. As a result, the equation is rewritten on incremental form:

$$\Delta T = \beta_T \frac{\sigma_{eq}\Delta p}{\rho C_p} \tag{3.22}$$

Substituting equivalent stress with equation (3.13), we arrive at an iterative equation for the increase in material temperature due to adiabatic heating:

$$T_{n+1} = T_n + \frac{\beta_T}{\rho C_p}\left[\sigma_{T,n} + R_n\right]\left[1 + C\ln\left(\frac{\dot{p}_n}{\dot{p}_{0,n}} + 1\right)\right]\Delta p \tag{3.23}$$

Adiabatic heating calculated post analysis, i.e. it does not affect the stress and strain calculations.

3.1.5 Model summary

The model itself assumes isothermal conditions (system temperature is constant) to reduce the number of parameters. In reality, this contradicts the adiabatic heating assumption; however, the adiabatic heating effect is not included in the calculations themselves but is calculated after stresses and strains have been determined. For tests with high strain rates, the process is assumed adiabatic since specimen will reach failure too quickly to dissipate the thermal energy. For low strain rates the assumption may cause erroneous simulation results.

The model also assumes material isotropy, both for the constitutive equations and the yield criterion. Some features from the SIMLab polymer model has not been implemented in this thesis. They are presented below:

- Viscoelasticity
- Kinematic hardening
- Brittle damage and ECL ductile damage

Several constants were used for calculation in the elastic, plastic and damage part of the model. All the parameters are presented in Table 1:

Table 1: SIMLab Material model constants.

Elastic parameters	
Constants	Description
E	Young's modulus
ν	Contraction ratio
Plastic parameters	
Constants	Description
α	Pressure sensitivity
σ_T	Yield stress in uniaxial tension
β_D	Plastic dilatation
θ_{Ri}	Initial isotropic hardening moduli $(i = 1,2,3)$
Q_{Ri}	Saturation value of R_i $(i = 1,2,3)$
C	Rate sensitivity
$\dot{p_0}$	Reference strain rate
Damage	
Constants	Description
D_I	Initial damage
D_C	Critical damage
Adiabatic Heating	
Constants	Description
β_T	Taylor-Quinney coefficient
C_p	Specific heat capacity
ρ	Material density

4 Material Testing

Several material tests were performed to determine various properties of the polypropylene compound. Uniaxial tension tests constitute the central tests of this thesis, performed at range of different temperatures and strain rates. In addition, a series of compression and laser flash tests to determine material parameters required for numerical simulation. Benchmark test were performed in conjunction with uniaxial tension tests to verify material isotropy, as well as controlling the test setup.

This chapter presents the material setup, measurement method and data calculations for the uniaxial tension tests. Other test setups are presented briefly together with their respective results, in chapter 5.

4.1 Test specimen

The following cylindrical test specimen were used for all uniaxial tension test in this thesis. It has a total length of 60 mm, with a convex specimen gauge to control the location of necking (Figure 8). Each end was fastened to the test machine through the threaded area, effectively shortening the specimen to 20 cm and assuring uniform stress conditions. The specimen gauge was used for all measurement purposes.

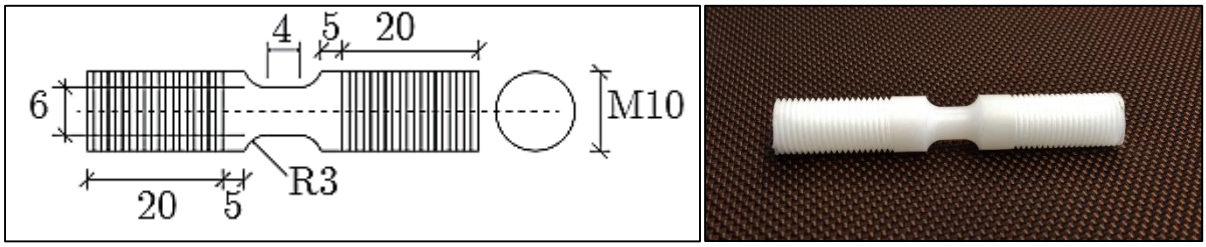

Figure 8: Geometry of tensile test specimen. Specimen gauge has an initial length of 4 mm and a diameter of 6 mm.

Specimens were machined from an extruded polypropylene pipe in both the longitudinal and circumferential direction of the pipe (Figure 9) and named according to their mill direction, with longitudinally milled specimen yielding the test names $L1, L2, L3, \ldots$ and circumferentially milled specimen $C1, C2, C3, \ldots$ and so on.

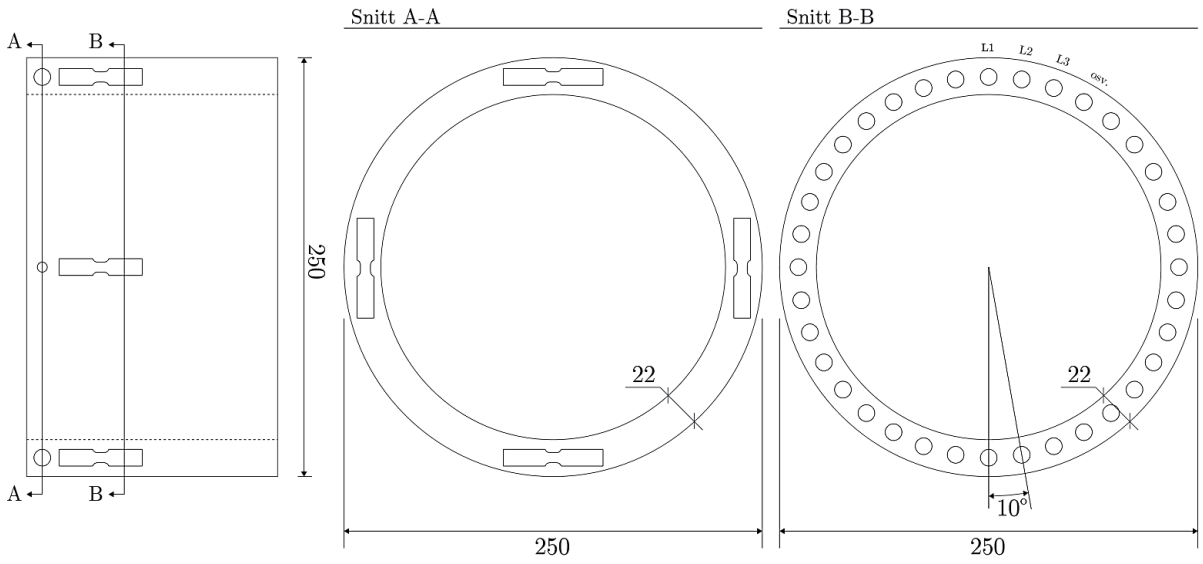

Figure 9: Polypropylene pipe dimensions. Test specimen are outlined according to their mill direction. Circumferential mill direction is illustrated in cross-section view A-A and longitudinal is illustrated in view B-B.

4.2 Test setup

All test specimen were elongated using an Instron 5944 single column testing system (Figure 10). Specimens were fastened to the machine at both ends using the threaded area. Keeping the lower end secured, the machine elongates the specimens by pulling the upper part with a constant velocity until fracture.

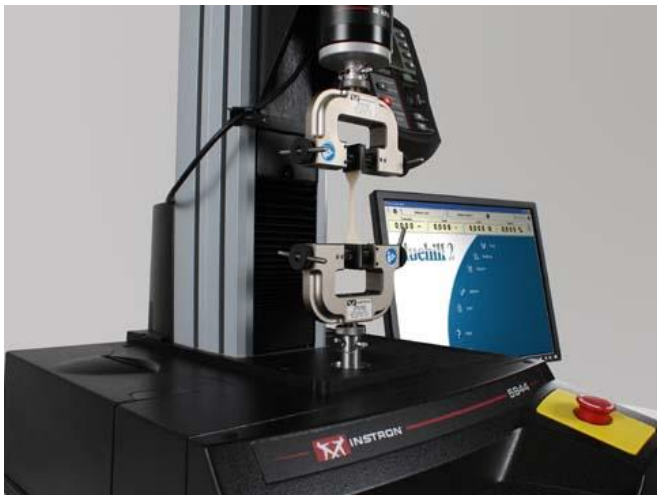

Figure 10: Instron 5944[33].

Three different elongation velocities were used for the uniaxial stress tests, ranging from low to high speed. For calculation and interpretation purposes, velocity is expressed in the form of initial strain rate, which may be expressed as:

$$\dot{\varepsilon}_0 = \frac{v}{l_0} \tag{4.1}$$

Where v is the machine velocity and l_0 is the initial gauge length of the specimen. The machine velocities, along with the corresponding initial strain rates and test name suffix is presented in table 2. The lowest strain rate is assumed to simulate quasi-static conditions.

Table 2: Strain rates used for uniaxial stress tests.

Machine velocity $[v]$	Initial strain rate $[\dot{\varepsilon}_0]$	Test name suffix
$2.4\ \mathrm{mm/min}$	$10^{-2}\mathrm{s}^{-1}$	$V1$
$24\ \mathrm{mm/min}$	$10^{-1}\mathrm{s}^{-1}$	$V2$
$240\ \mathrm{mm/min}$	$1\ \mathrm{s}^{-1}$	$V3$

Deformation history of the specimens were recorded by taking pictures at a constant frequency, using two Prosilica GC2450 cameras with macro lenses Nikon 105 mm and Sigma 105 mm. These cameras are denoted as "DIC cameras" henceforth. Principal strains were calculated using digital image correlation (DIC) by comparing the images as the specimen was elongated. To use DIC, the surface of the specimen must have a random dot pattern: a speckled surface. Patterns were initially provided by coating the specimen with white paint, and then lightly spraying it with black paint, however the paint became cracked and unsuitable for use at lower temperatures. For material test below room temperature, test specimens were instead covered in white grease then lightly coated in black powder ($75 - 125\mu m$ grain size) to provide the speckled surface.

Excepting tests performed at room temperature, the setup is identical for all uniaxial testing (Figure 11). To achieve lower temperatures, the machine clamps and test specimen were encased in a polycarbonate (PC) chamber produced by SABIC Innovative plastics, named Lexan Exell D. The chamber was cooled by injections of liquid nitrogen, with a thermocouple temperature sensor to regulate injections. Surface temperature of the specimens was measured continuously with an IR-camera of type FLIR SC 7500, providing a pixel map of temperature variation in specimens as they deform.

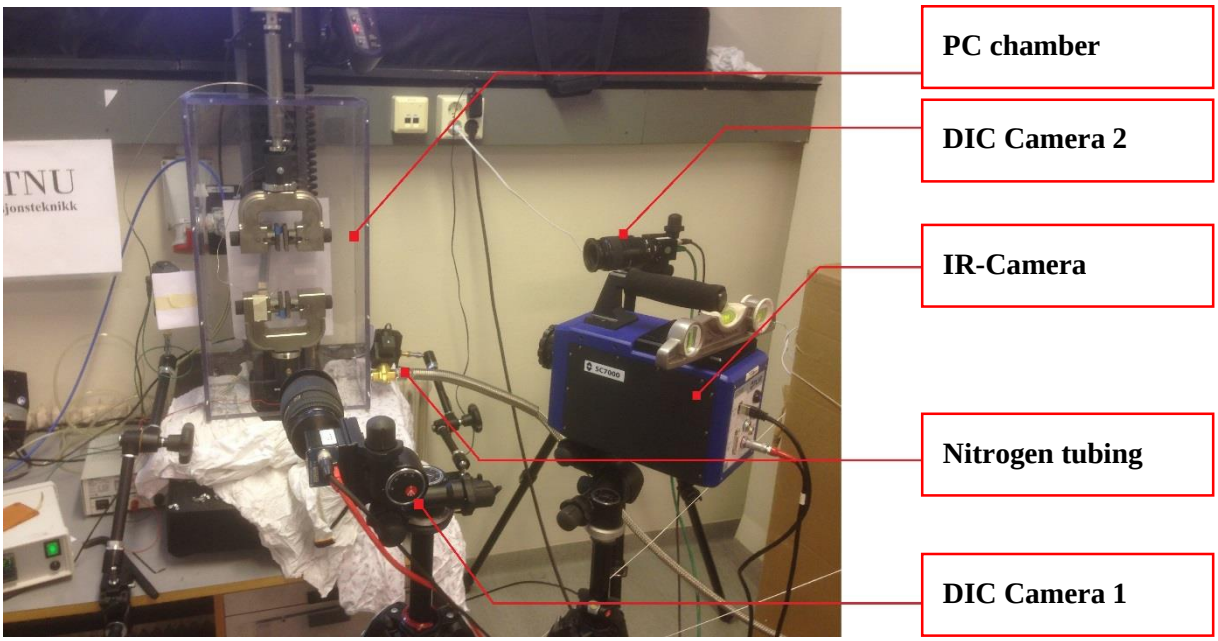

Figure 11: Test setup with polycarbonate chamber. Picture shows test setup for all uniaxial tensile tests below room temperature. The nitrogen tubing is connected to a large storage tank containing liquid nitrogen (not shown in picture).

4.3 Post processing

Primary results of the material testing are true stress-strain curves at each test condition. The Instron machine provided the force history, while DIC was used to obtain the strain history, both longitudinal and transversal. The capture frequency of the DIC cameras are equal to the sampling frequency of the Instron logger, providing coinciding data values for the force and principal strains.

Strain history

Digital image correlation was performed by using eCorr, a software created by PhD. Egil Fagerholt at NTNU [34]. As described in chapter 4.2, DIC calculates the strain history of a specimen by comparing successive images using the speckled pattern. The first image, i.e. when the specimen is undeformed, constitutes the reference picture in eCorr. This picture is discretized by meshing it with a specified element size and element type that covers the specimen gauge (Figure 12). By using cross correlation of the grey scale value within each subset (mesh-element), the mesh will shift along with the specimen, providing the strain history based on the displacement of the mesh.

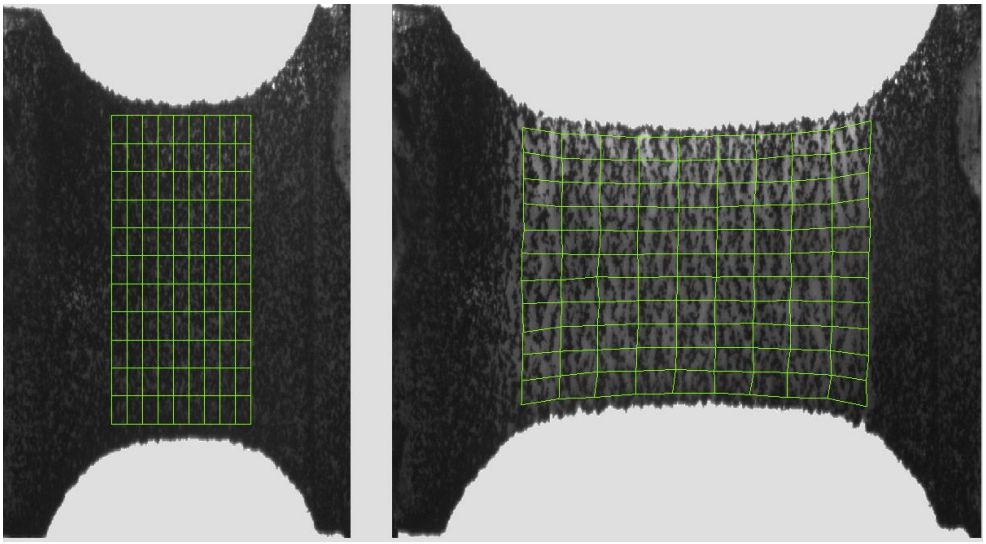

Figure 12: Mesh deformation in eCorr. Undeformed specimen shown on the left. The mesh follows specimen deformation by using the speckled pattern.

The test setup includes two DIC cameras positioned at 90 degrees relative to each other (Figure 11). Each camera provides an individual series of images, producing two instances of strain history data in eCorr for both longitudinal and transversal true strain (Table 3).

Table 3: Camera specific strain history variables.

Camera	Longitudinal true strain	Transversal true strain
Camera 1	ε_{l1}	ε_{t1}
Camera 2	ε_{l2}	ε_{t2}

Each camera have their own set of images and thus their own mesh and strain history data. Number of mesh elements and mesh position may differ between the cameras. Strain values were always selected from the mesh column with the lowest cross sectional area during drawing. With the specimen shape controlling the onset of necking, this was always in the middle of the gauge.

Strain history was measured in the form of principal strains since the test is uniaxial. Comparing rotationless to principal strains, i.e. ε_{xx} and ε_{yy} compared to ε_{11} and ε_{22}, we observe that the curves coincide with almost no error (Figure 13), indicating negligible shear strains and justifies averaging of principal strains in each mesh column.

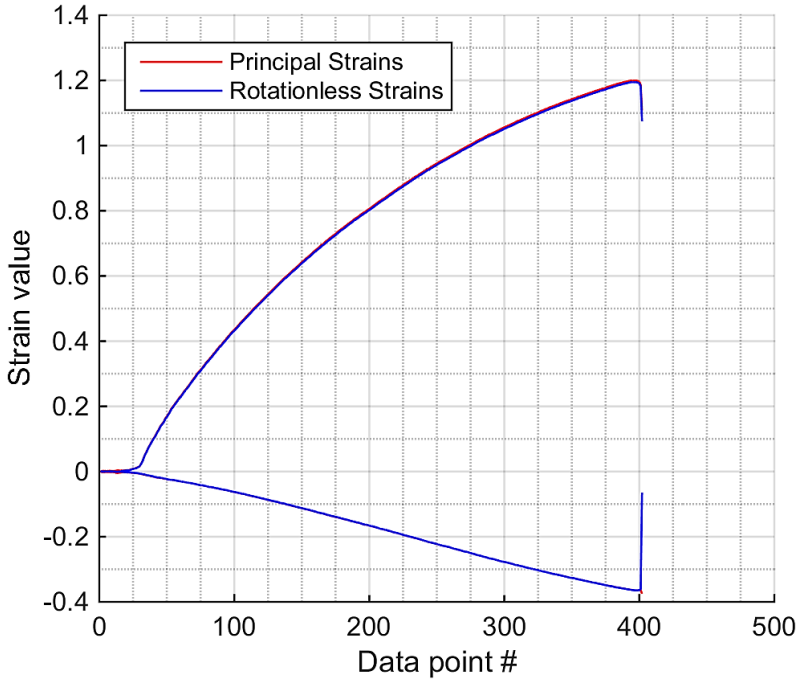

Figure 13: Comparison between principal and rotationless strain. Figure show principal and rotationless strain values from camera 1 at -30℃ and quasi static strain rate. Longitudinal strain values are positive, transverse strain values negative.

Stress history

Since true stress uses the updated cross sectional area rather than the initial one, the transverse strain history is required for stress calculations. Logarithmic (true) transverse strains may be written as:

$$\varepsilon_t = \ln\left(\frac{d}{d_0}\right) \qquad \text{yielding } d = d_0 \exp(\varepsilon_t) \tag{4.2}$$

Where d_0 and d is the initial and deformed specimen diameter, respectively. Substituting for the cross sectional area, the true stress may then be expressed as:

$$\sigma = \frac{F}{A} = \frac{4F}{\pi d_0^2 \exp(\varepsilon_{t1}) \exp(\varepsilon_{t2})} \tag{4.3}$$

Where F is the force history, while ε_{t1} and ε_{t2} denotes the transversal strain from DIC camera 1 and 2 respectively.

Since equation (4.3) uses the transversal strain from two different cameras, but is plotted against one dataset of longitudinal strain, any camera specific discretization error must be accounted for when calculating the stress-strain curve. Data points $(\varepsilon_{t,i}, \varepsilon_{l,i})$ calculated from each camera may vary slightly (Figure 14 a)). Consequently, the data points are linearly interpolated such

that the longitudinal strain coincide (Figure 14 b)). The camera with the largest maximum longitudinal strain is always chosen for interpolation.

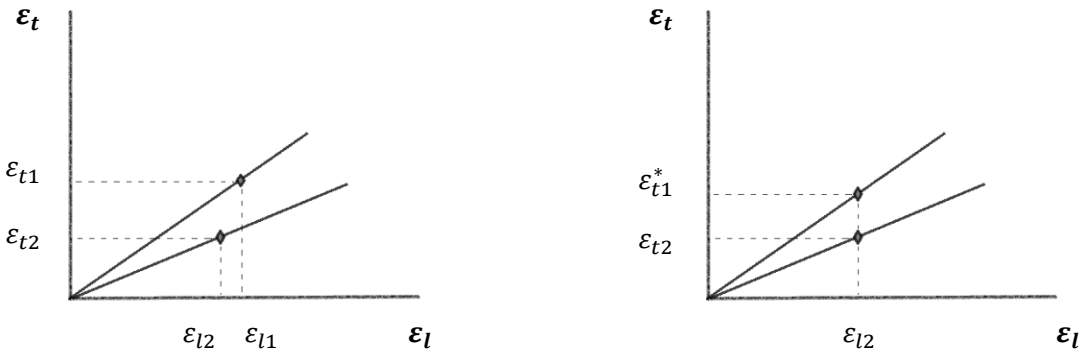

a) Default strain values

b) Interpolated strain values

Figure 14: Interpolation of camera specific strain. In this figure, default transversal strain from camera 1 (upper line) is interpolated such that the longitudinal strain coincide with camera 2.

5 Material testing results

This chapter presents the results from the various material test performed. Each test series is briefly summarized, followed by a presentation of the results for each material test. Uniaxial tension test were performed to determine general material behavior of polypropylene at different temperatures and strain rates. Compression and laser flash tests were performed to determine material parameters required for numerical simulations.

5.1 Temperature varied uniaxial tensile tests

The uniaxial tensile test were performed using the test setup described in chapter 4, using the strain rates described in Table 2. Specimen were tested at four different initial temperatures, each designated a test name suffix (Table 4).

Table 4: Initial temperatures used for uniaxial stress tests.

Initial specimen temperature [℃]	Test name suffix
25	$T1$
0	$T2$
-15	$T3$
-30	$T4$

Using the test name suffixes presented, all the material tests may be expressed in an abbreviated form. For instance, test $L31/T3/V2$ describes a longitudinally milled specimen, performed at -15℃ with an initial strain rate of $10^{-1}\ s^{-1}$. All material plot legends are presented this way, with additional suffixes for PC-chamber, grease and camera numbering were relevant.

Results

Every uniaxial tension test was performed twice, yielding 24 tests in total. Stress-strain curves are plotted categorically with respect to either temperature or strain rate for easy comparison and efficiency. Results from benchmarking, temperature variation and scanning electron microscope (SEM) are also presented. Larger versions of all stress plots and strain plots may be found in Appendix: 9A for uniaxial tests and 9B for compression tests.

5.1.1 Specimen deformation pictures

All Specimens deformed in a similar manner, starting with yielding and initial necking in the middle of the gauge, followed by varying degrees of cold drawing (Figure 15)

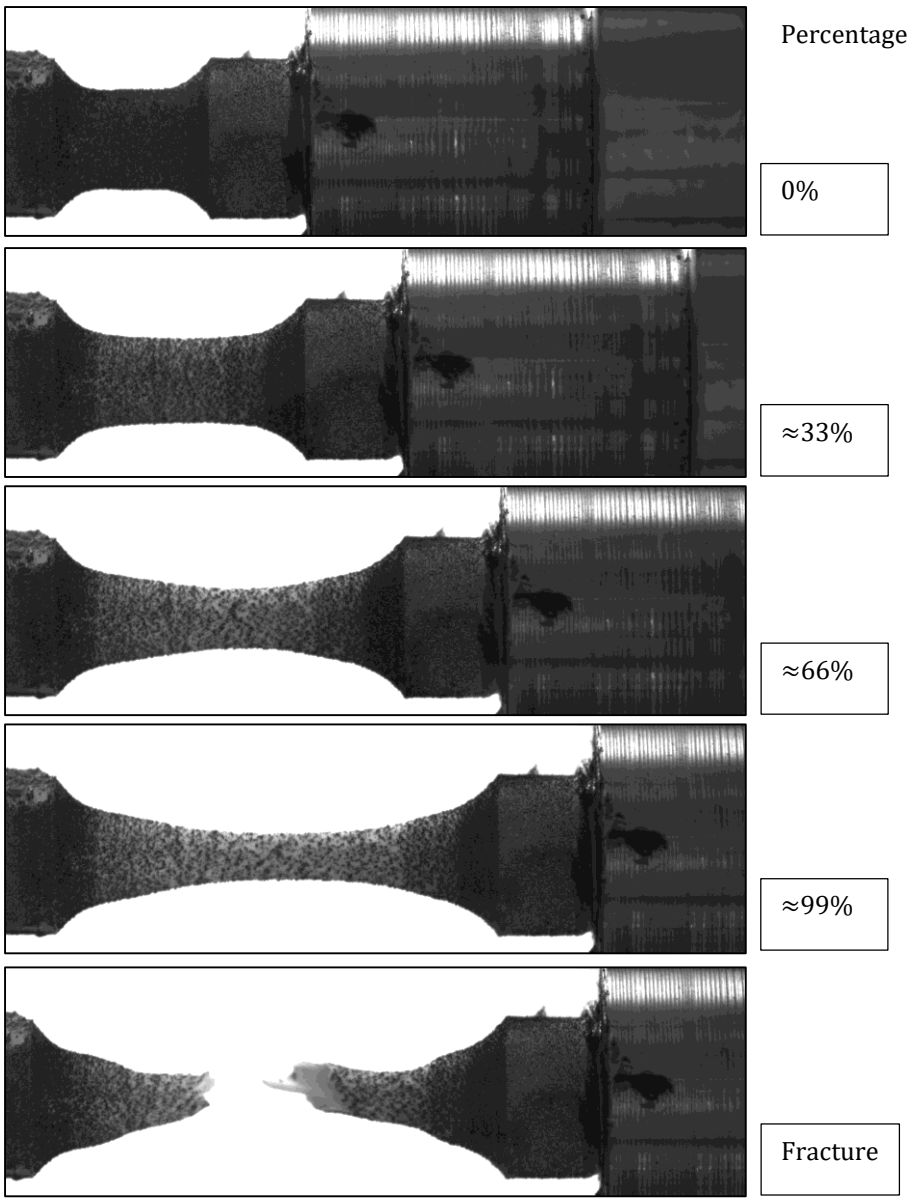

Figure 15: Specimen deformation for L40/T2/V3. Figure shows DIC pictures from camera 1 for test performed at 0℃ with strain rate $1s^{-1}$.

Most specimen fractured in the middle of the specimen gauge as shown in figure 15, where the cross sectional area is the smallest. Some test would fracture in other places of the gauge where the cross section is larger, likely due to weaknesses or imperfections in the material.

5.1.2 Benchmark

A series of benchmark test were performed to verify that using a PC-chamber and grease has little to no impact on test accuracy. The tests also checks for material anisotropy by comparing circumferential and longitudinal test specimens (Figure 16). Benchmark tests are performed at room temperature, using quasi-static strain rate.

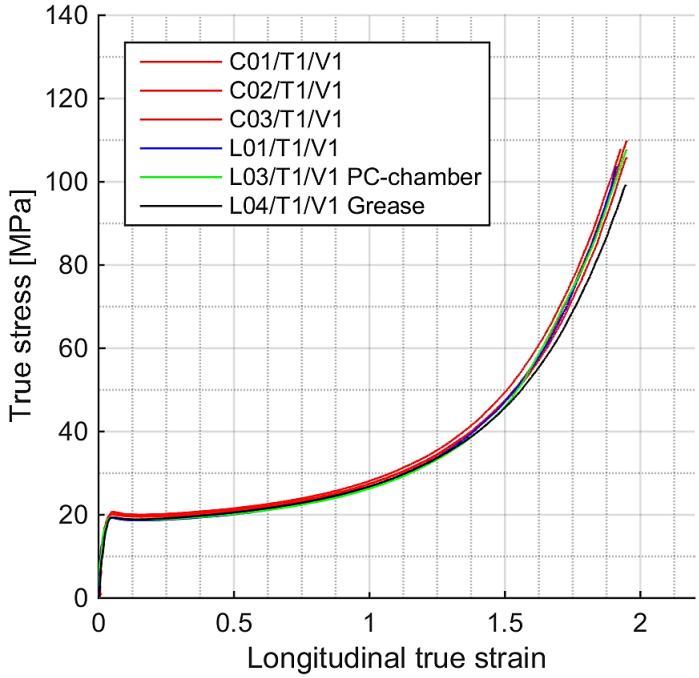

Figure 16: Stress-strain plot for benchmark tests. Largest difference in stress, 11 MPa, is found between C01 and L04 at strain values between 1.85 and 1.9.

The benchmark test results are largely identical, indicating little impact by using a polycarbonate chamber and grease and supporting the assumption of material isotropy. Consequently, every material tests series other than benchmarking uses longitudinal specimen only. It is assumed that the effect of using PC-chamber and grease can be neglected when comparing testing results at and below room temperature.

Two additional plots from the benchmark tests can be found in Figure 17. The camera specific transverse strain (fig. a) shows the transverse strain from both camera 1 and camera 2 for each benchmark test. The plot indicates almost no difference in camera specific transverse strain. Figure 17 b) complements the conclusion from Figure 16, showing little difference in volumetric strain between tests.

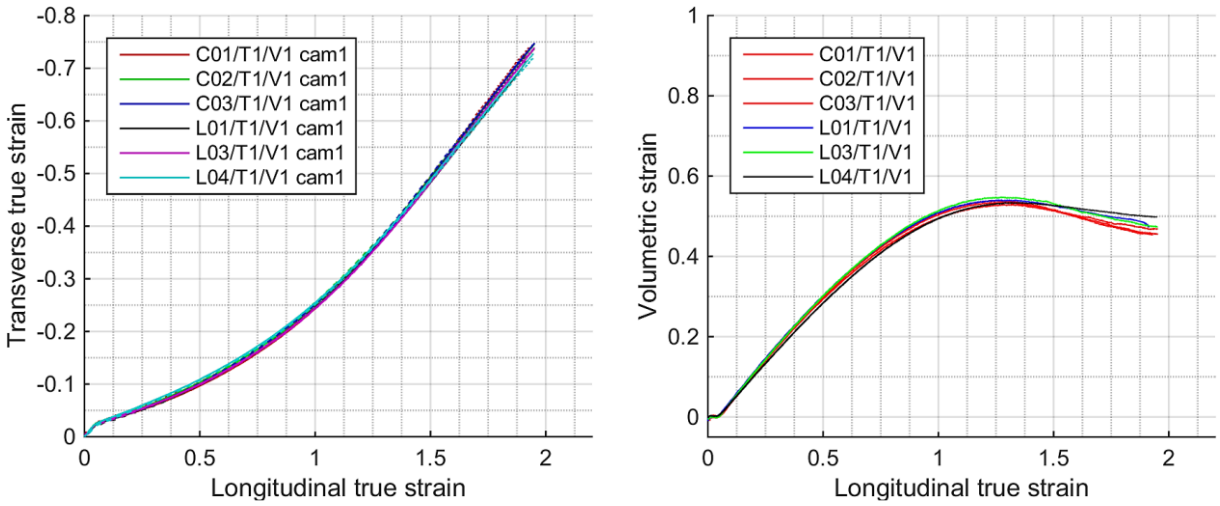

a) Camera spesific transverse strain

b) Volumetric strain

Figure 17: Benchmark strain plots. In figure a), each material test have a continuous line to represent camera 1 and a dashed line to represent camera 2.

Camera specific strain

In addition to the benchmark tests, camera specific transverse strain was plotted against longitudinal strain at varying test parameters to verify camera accuracy (Figure 18). The sampled strain curves for 25 and −30℃ show very little variation between DIC cameras, and any difference in camera specific transverse strain is assumed negligible when reviewing test accuracy. The plots for 0℃ and −15℃ can be found in Appendix: 9A.

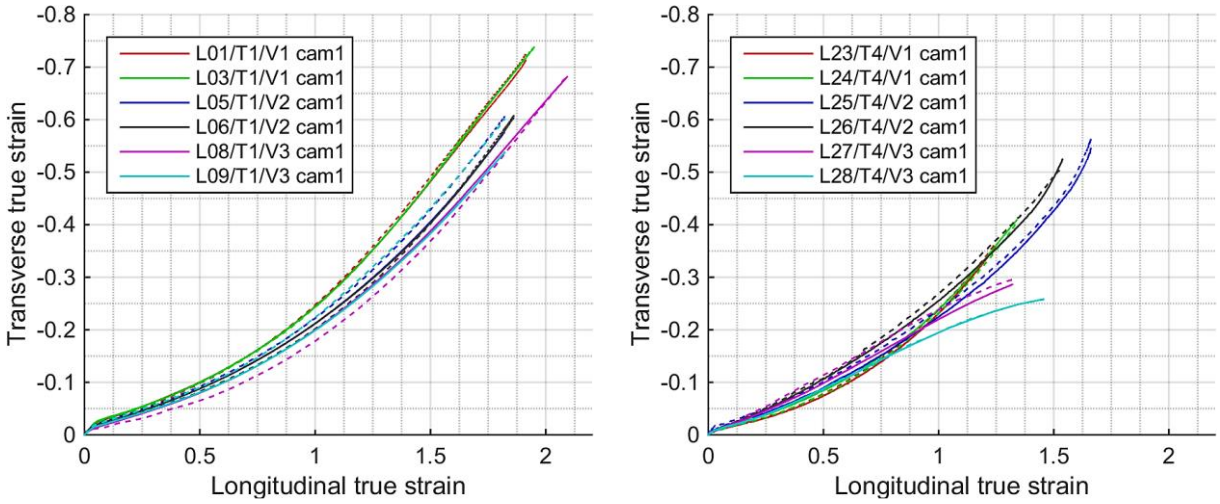

a) 25℃

b) − 30℃

Figure 18: Camera specific transverse strain. Each material test has a continuous line to represent camera 1 and a dashed line to represent camera 2. Largest difference in transverse strain between camera 1 and 2 was found in test L09: 0.06.

5.1.3 Stress strain curves

This section present the results of the 24 uniaxial tension material testing, categorized by either temperature or strain rate for easy comparison. Continuous lines are used to represent the characteristic material tests, i.e. the test chosen to represent the material for that strain rate and temperature. Dashed lines indicate the other material test with identical strain rate and temperature. With the exception of $L01$ versus $L02$, material test with the highest ultimate stress have been chosen as characteristic.

Effect of strain rate

Temperature categorized curves (Figure 19) shows that the behavior of the PP specimen is clearly dependent on strain rate during testing. We observe that increasing the strain rate results in higher yield stress and reduced strain hardening at all temperatures, as expected. The reduction in strain hardening is primarily ascribed to specimen heating; high strain rates causing significant temperature increase during drawing, reducing strain hardening as the specimen deforms.

Comparing the plots categorically reveals a reduction in longitudinal strain as the initial temperature is lowered, and it is clear that specimen temperature affects elongation of the material. No consistent trend is observed when correlating initial strain rate and longitudinal strain, however some plot lines indicate increased drawing when increasing the initial strain rate, possibly caused by specimen heating. Jagged plot lines (see $L35$ in particular) is the result of nitrogen injections, causing noticeable temperature fluctuation for a short period.

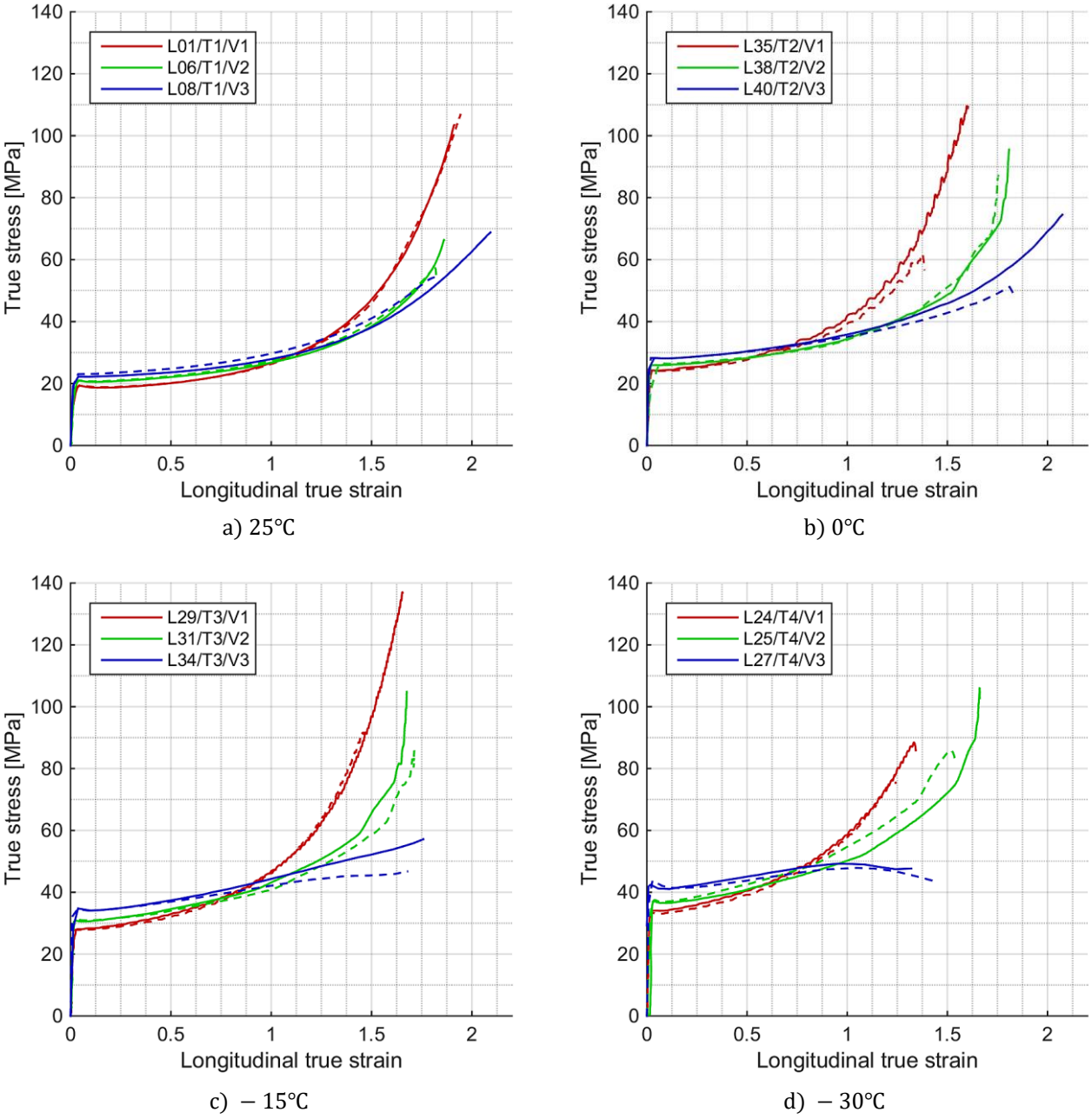

Figure 19: Temperature categorized stress-strain plots. Curves in figures a) through d) are categorized by initial temperature. Dashed line represent corresponding material test performed at the same temperature and strain rate. Increasing strain rate yields higher yield stress and less strain hardening.

Effect of initial temperature

Strain categorized curves (Figure 20) illustrates the effect of changing initial temperature of the specimen. The choice of characteristic curve is unchanged. We observe that increasing initial temperature causes lower yield stress and higher longitudinal strain, indicating increasingly ductile behavior. Although ultimate strength varies with initial temperature, the slope gradient

during plastic flow is similar for most curves. Compared to strain rate, it seems initial temperature has less impact on strain hardening

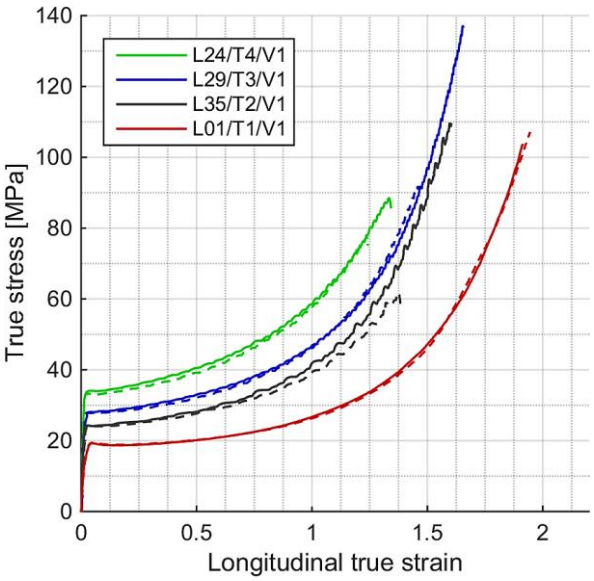

a) $10^{-2}s^{-1}$

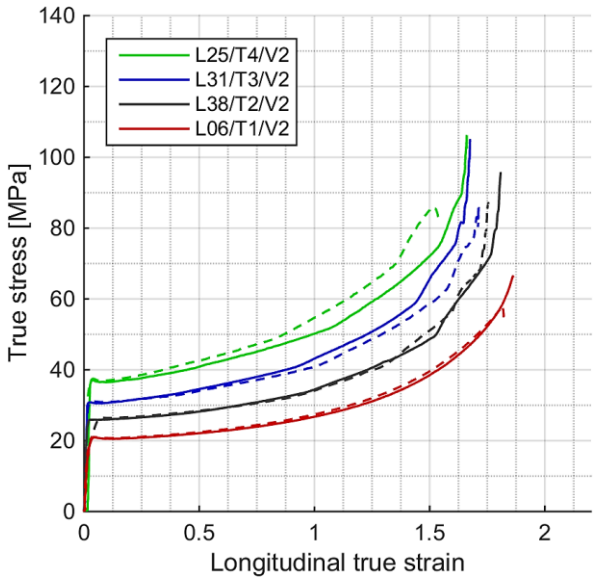

b) $10^{-1}s^{-1}$

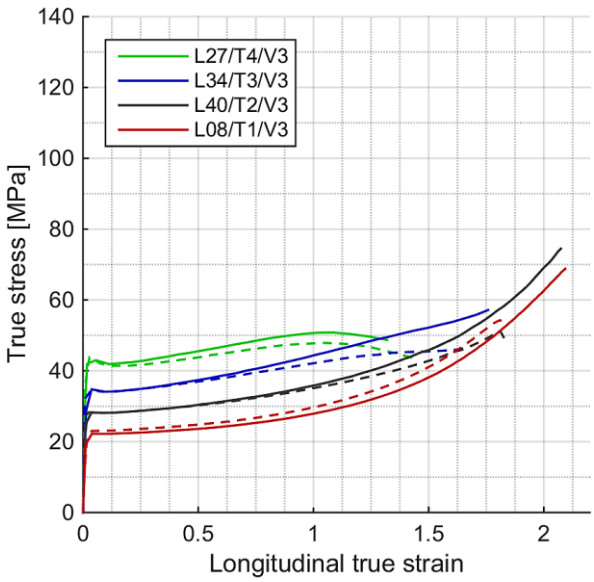

c) $1s^{-1}$

Figure 20: Strain rate categorized stress-strain plots. Curves in figure a) through c) are categorized by initial strain rate. Increasing temperature causes lower yield stress and higher longitudinal strain. Dashed line represent corresponding material test performed at the same temperature and strain rate.

The only stress-strain curves that differ from the general trend of steadily increasing strain hardening until fracture is $L27/T4/V3$ and $L34/T3/V3$, i.e. -30 and -15℃ at the highest strain rate. Both test specimens fractured at lower stress levels, and both show declining strain hardening when approaching failure.

As mentioned in chapter 2.4, sufficiently low initial temperature and high strain rate may cause material failure by crazing rather than shear yielding. This transition, coined "ductile-to-brittle transition phenomenon", has been observed in both glassy[4] and semi-crystalline[6] polymers. Material test performed by Jang et al. [6] shows a transition from ductile to brittle fracture, by either predominant shear yielding or crazing, respectively. Therein, reducing temperature and increasing strain rate gradually reduced ductility, bringing the material into the transition zone where crazing and shear yielding would coexist. The transition is described as follows:

> A transition zone is noted in the spectrum of rates and temperatures where crazes and shear bands coexist and the samples exhibit crazing subsequent to the initial viscoelastic regime, followed by general yielding, a yield drop and a small extent of cold drawing. As the temperature is further decreased or strain rate increased, the extent of cold drawing is reduced and the shear yielding gradually gives way to crazing.
>
> Jang et al. 1984: p. 3412

This description has some resemblance to material behavior observed from Figure 20, in particular the reduction in cold drawing. The resulting conjecture is that crazing possibly occurs when decreasing initial temperature and increasing strain rate, but not sufficiently to cause brittle fracture for test performed in this thesis. Neither does it explain material softening for $L27$ and $L34$ approaching failure, which is discussed in chapter 5.1.4.

Reduced neck propagation

The dissimilar material test $L27$ and $L34$ are studied further by looking at camera images exactly prior to failure, i.e. the next image shows specimen fracture. The specimens experience local necking at the middle, but rather than cold drawing, they simply fracture with substantially less neck propagation (Figure 21). For comparison, test $L40$ exactly prior to failure shows clear neck propagation. Significant reduction in neck propagation only occurs for material test at the highest strain rate with initial temperatures -15 and $-30℃$.

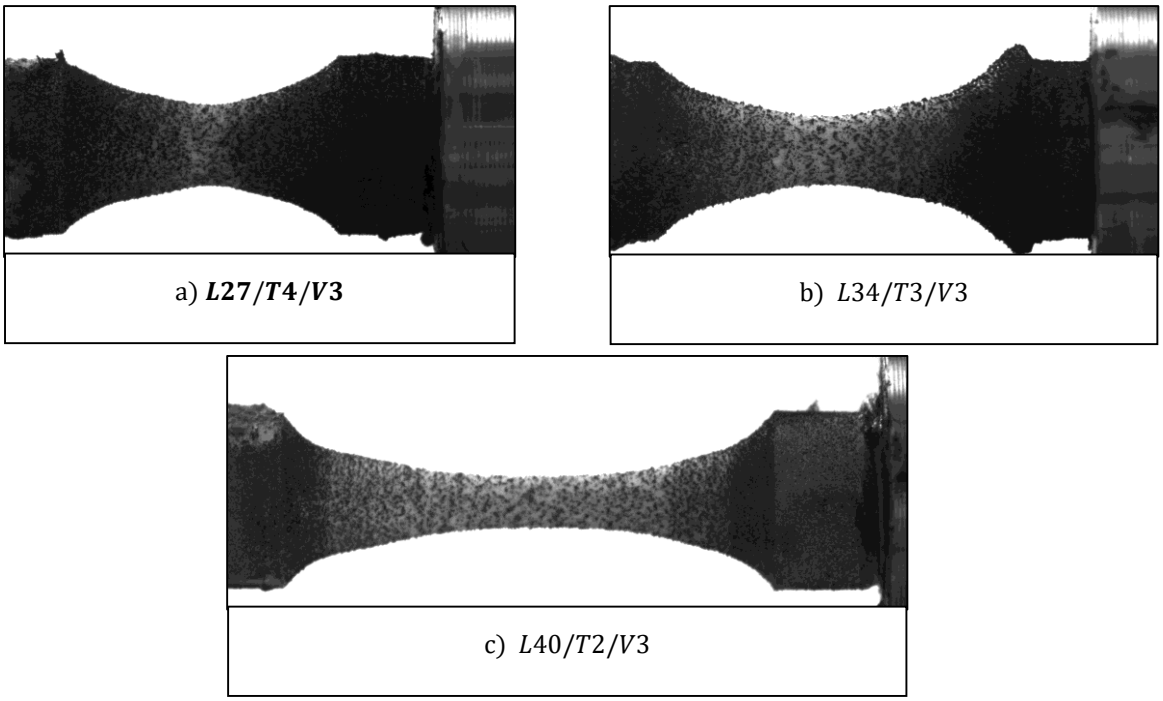

Figure 21: Reduced neck propagation for different test specimen. Figure a) and b) depicts material tests at -30℃ and -15℃, with initial strain rate $1s^{-1}$, just prior to failure. Figure c) depicts material test at 0℃, with initial strain rate $1s^{-1}$, just prior to failure. Combination of high strain rate and low initial temperature limits neck propagation.

Serving as a complementing or competing explanation of early failure in material tests $L27$ and $L34$ is reduced neck propagation by localized temperature softening. The mechanisms of neck propagation, in short, consists of work softening of the convex profile surrounding the specimen neck, followed by strain hardening of the concave profile adjacent to the neck (Figure 22). During cold drawing, the necked region remains stable while the neck propagates along the entire specimen.

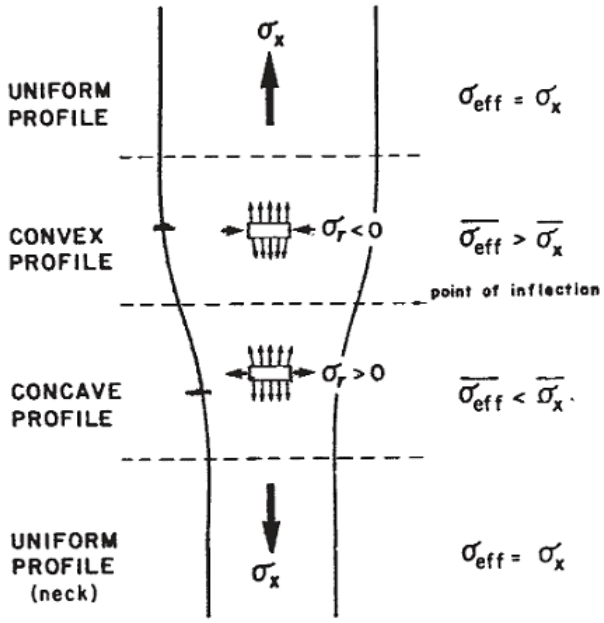

Figure 22: Sketch of neck development in linear polymer.[17] Softening occurs in the convex profile and hardening in the concave profile.

Increasing the strain rate results in specimen heating based on the theory of adiabatic heating. With decreasing initial temperature, it is suspected that this heating becomes increasingly localized to the initial neck profile. Due to the low thermal diffusivity of polymers, the heat is poorly conducted in the specimen and remains localized to the neck instead.

The resulting conjecture is that with sufficient localization and magnitude of specimen heating, the neck profile temperature softens sufficiently to cause early fracture. Rather than propagating the neck through strain softening and hardening of the convex and concave profile, the initial neck profile develops and critically temperature softens before the neck can fully develop. Specimen heating and heat localization is studied further by looking at IR-camera results (chapter 5.1.4).

Volumetric strain

Volumetric strain curves are categorized by initial temperature, similar to the previous stress-strain curves, and uses the same choice of characteristic material tests. Material behavior is similar for most curves. Initially, increase in volumetric strain is near constant, leveling off as it is further drawn and sinking slightly just prior fracture (Figure 23).

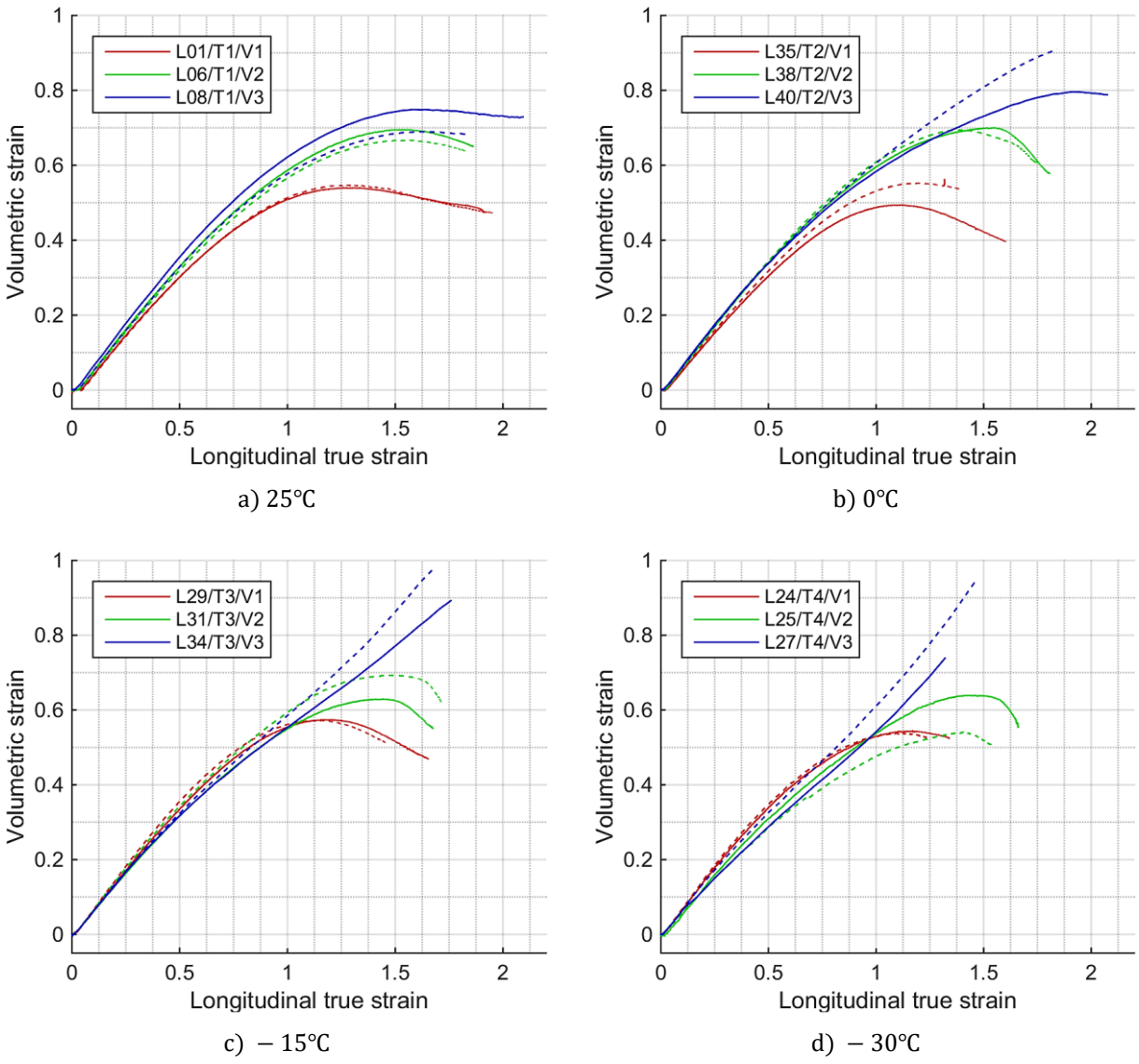

Figure 23: Temperature categorized volumetric strain. Curves in figures a) through d) are categorized by initial temperature. Dashed line represent corresponding material test performed at the same temperature and strain rate.

The dissimilar behavior of material tests $L34$ and $L27$ is observed again in Figure 23 c) and d). While all other material curves level off as they approach failure and most of them with declining volumetric strain just prior to fracture, aforementioned tests experience almost no change in dilatational response during elongation.

The volumetric response curves seem indicative of a change in physical response as initial temperature and strain rate is changed. With little existing literature on the topic of volumetric response in semi-crystalline polymers specifically, it is difficult to discern exactly what changes for test $L34$ and $L27$, and void contraction is the only proposed explanation for this phenomenon.

Generally, ductile failure in polymers is attributed to shear yielding of the material, accompanied by void growth by cavitation [21, 23]. Presented in chapter 5.1.5, scanning electron microscope (SEM) results for one uniaxial tension tests clearly shows void formation, which together with the dilatational response (related to the contraction ratio ν) should constitute the total volumetric response [35]. For specimen that properly cold draw, it is proposed that the voids and coalesced voids contract in the final stages prior to fracture, causing the observed decline in volumetric strain as the voids in the material shrink. For test $L34$ and $L27$, this contraction possibly does not occur since the material does not fully draw, but rather experience an early onset of fracture as discussed earlier. This early onset of fracture occurs before the voids can contract, and the dilatational response consequently does not change.

Yield stress

Yield stress is herein equivalent to the peak stress, alternatively intrinsic yield stress: the highest measured stress before strain softening in the material. For most tests, this stress value is observable as a slight peak in the stress-strain curve prior to the plastic domain (see Figure 19, Figure 20).

The yield stress is dependent upon both the initial temperature and –strain rate. Increasing strain rate results in higher yield stress, while increasing the temperature lowers yield stress (Figure 24). Yield stresses were used in determining the rate sensitivity of polypropylene, denoted C. Using characteristic curves, yield stress was plotted against the common logarithm of initial strain rate, providing three data points for each temperature (Figure 25). Rate sensitivity was calculated using equation (3.13), using yield stress from the quasi-static tests as equivalent stress.

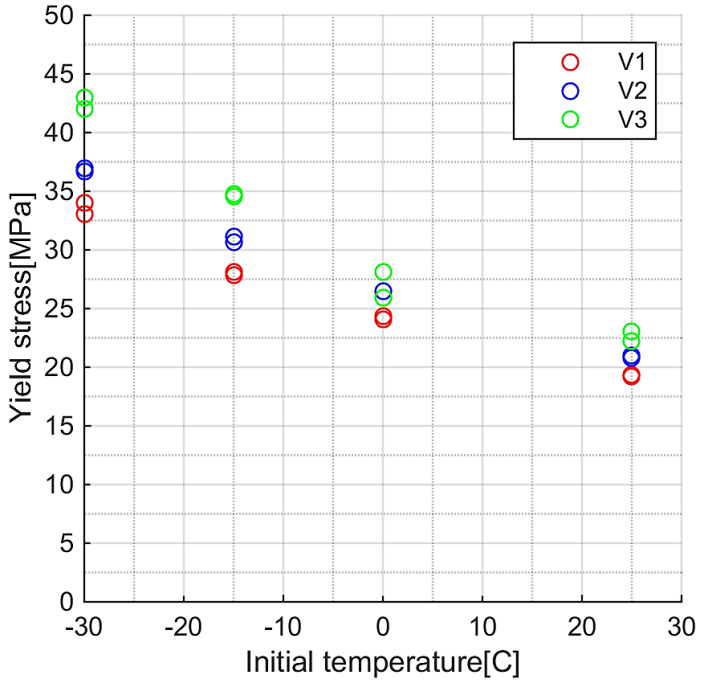

Figure 24: Yield stress for different initial temperature and strain rate. Large difference in yield stress when increasing strain rate and decreasing temperature.

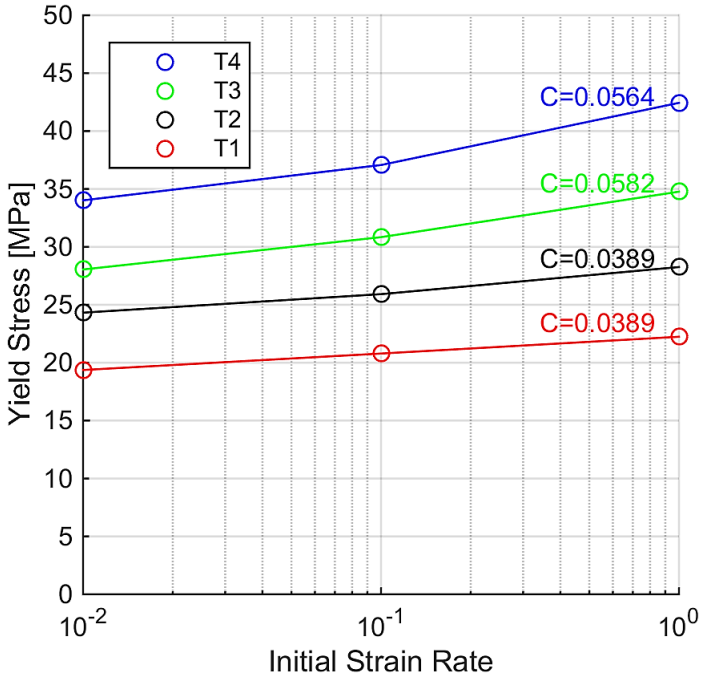

Figure 25: Calculation of rate sensitivity. Yield stress from characteristic tests are used. Superposed number is the calculated rate sensitivity for each initial temperature.

Young's modulus

The initial Young's modulus was found by using a segment of the material curve in the elastic domain. Due to transverse rigid body movement of the test specimen at the start of elongation, caused by poor fastening mechanisms (Figure 26), most material curves are irregular prior to yielding. This is especially critical for initial strain rates of 240 mm/min due to a low number of data points in the elastic domain. All specimen stabilize after the initial rigid body motion.

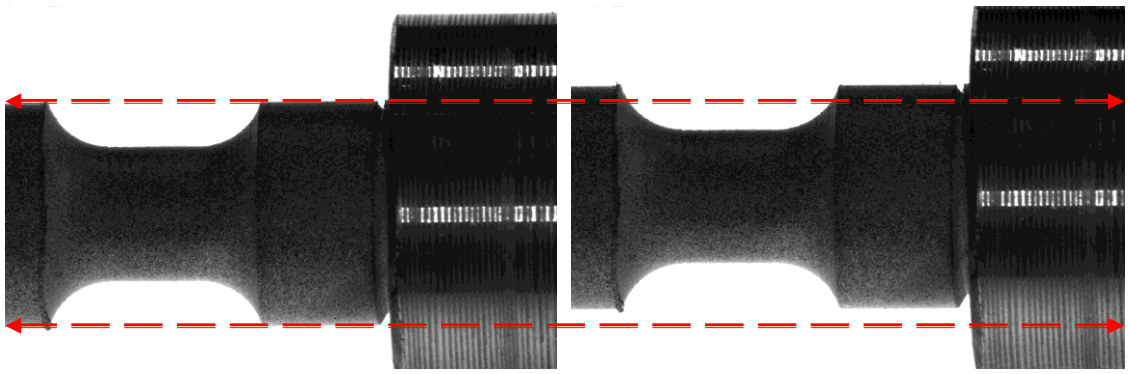

a) Specimen before onset of tension b) Specimen after initial rigid body motion

Figure 26: Initial rigid body movement of test specimen. As the Instron machine starts pulling on the specimen, it moves slightly in the transversal direction due to poor fastening mechanisms. Specimens remain still (transversally) after the initial movement. Draw direction is to the right.

Rigid body movement causes measurement inaccuracy for the stress strain curves prior to yielding (Figure 27). For some tests, transverse movement during initial deformations is quite substantial. Rigid body movement was the main limitation when choosing mesh size and placement; choosing an excessively fine mesh would render it unable to follow the speckled surface during rigid body motion. Reducing or removing initial rigid body motion will undoubtedly improve accuracy in the elastic domain.

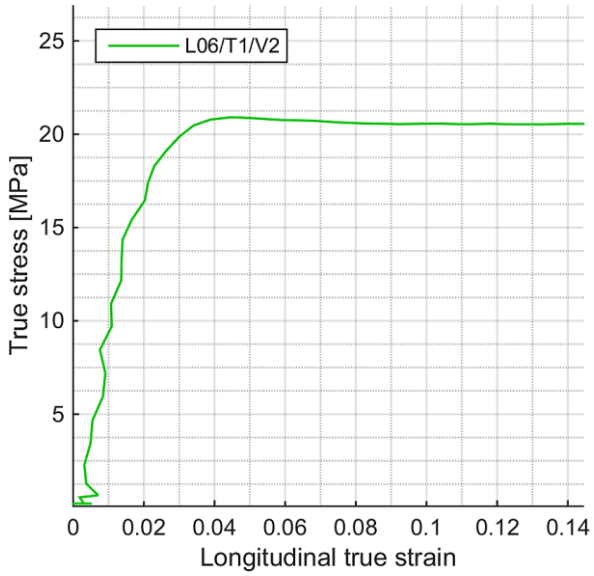

Figure 27: Elastic domain for material test L06. Results are irregular due to rigid body movement of specimen during initial deformations.

Young's modulus is calculated by using stress and strain values roughly between 10 % and 80 % of yield stress, using linear interpolation. Calculated values should be evaluated critically, especially when compared to the yield stress at which point the material curves have stabilized. Despite the inaccuracy, we may still observe the trend of increasingly ductile behavior as initial temperature is increased and initial strain rate is decreased (Figure 28).

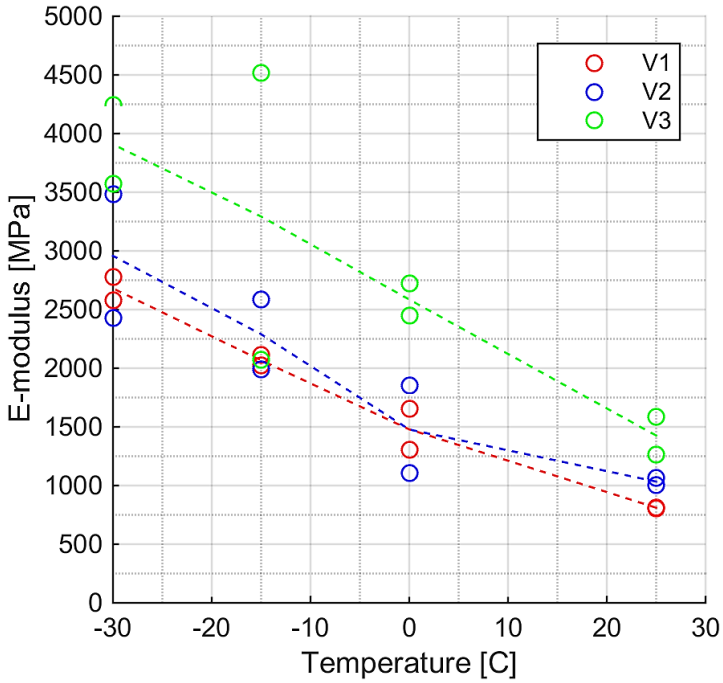

Figure 28: E-modulus for different initial temperature and -strain rates. Dashed lines are line plots using average value at each initial temperature.

Contraction ratio

Using transverse and longitudinal strain values, the contraction ratio, ν, was calculated for each material test. Results are categorized by temperature with the same choice of characteristic curves as previous plots. Due to rigid body movement, data values at 0.1 longitudinal strain or lower is not included. For all initial temperatures, there is significant variation in the contraction ratio as the specimen elongate (Figure 29).

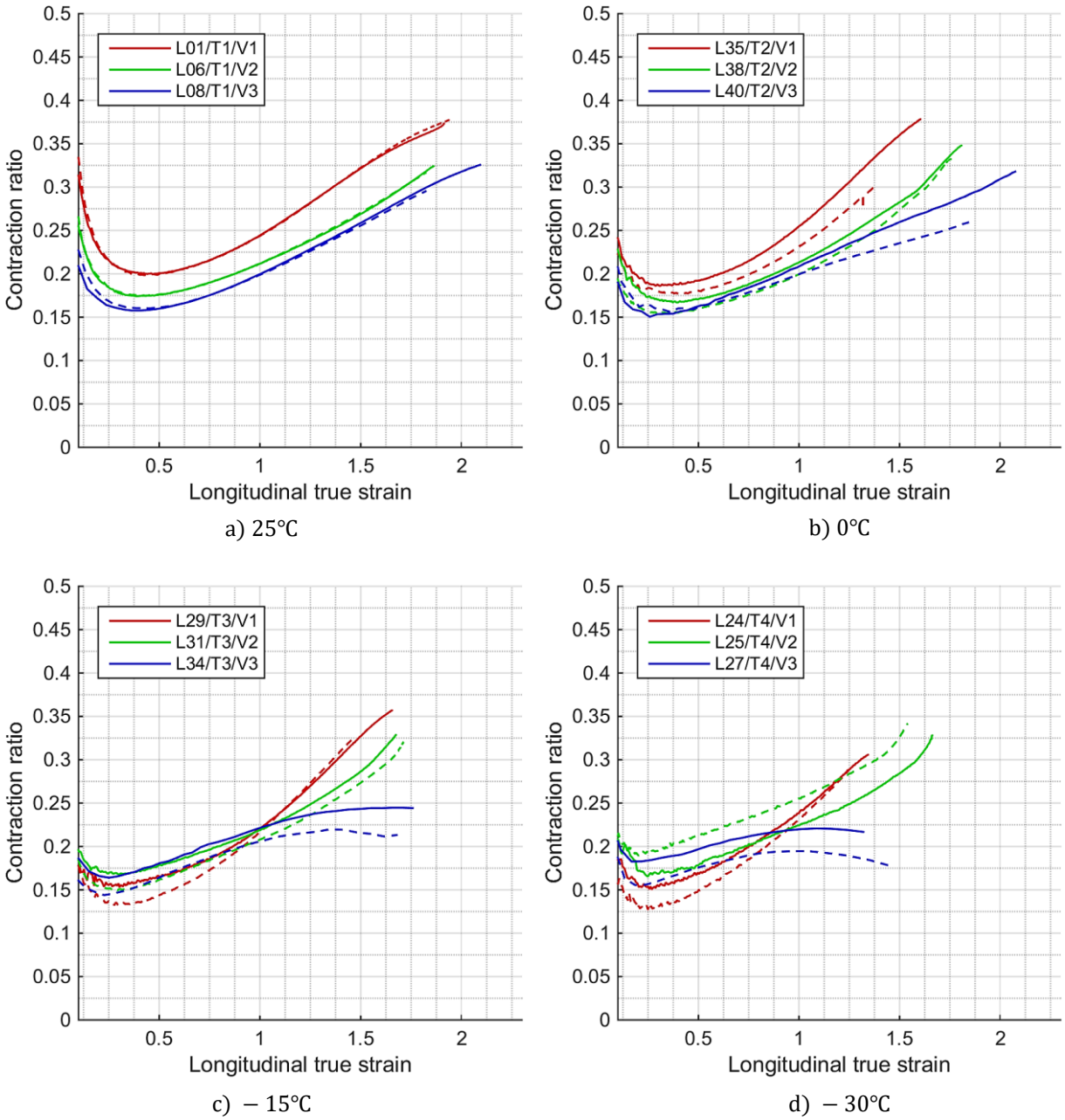

Figure 29: Contraction ratio for all material tests. Results are categorized by initial temperature. Dashed lines represent corresponding material test performed at the same temperature and strain rate.

The contraction ratio constitutes one of the material parameters used in numerical simulations later in this paper. In these simulations, contraction ratio is modeled as a constant elastic parameter and does not account for the strain dependent variation in the plastic domain. In the plastic domain, the dilatational response is modeled using a constant plastic dilatation parameter. Effect of contraction ratio on numerical simulation is discussed in chapter 6. Since the contraction ratio only affects the elastic domain for analyses, which already have an inaccurate Young's modulus, an average value of $\nu = 0.24$ was used for all initial temperatures.

5.1.4 Temperature variation

During plastic flow, test specimens will experience heating as they are deformed. An IR-camera was raised to measure specimen heating, providing a temperature map of the test specimen that continuously visualizes image-by-image temperature variation (Figure 30 a)). Maximum temperature in the gauge was calculated for each image, providing a temperature-by-image plot to illustrate material heating (Figure 30 b)).

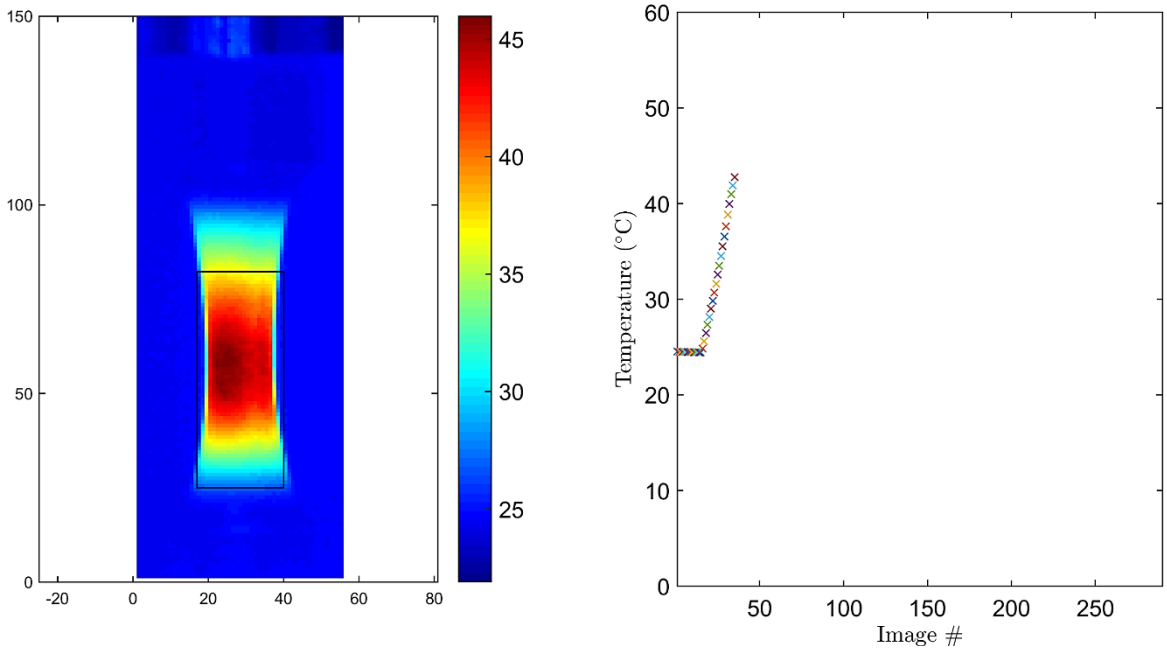

a) Temperature variation in specimen

b) Measured maximum temperature

Figure 30: Maximum specimen temperature and temperature map. As the specimen deforms, the IR-camera measures temperature in each pixel and provides a temperature map for each image (fig. a)). Maximum temperature was recorded from each temperature map by defining a rectangle enclosing the specimen gauge. Fig. b) plots the largest recorded temperature within the specified rectangle, for each image.

Using the temperature-by-image plot, maximum temperature difference was calculated for each characteristic material test. While the chamber temperature was controlled correctly by the temperature sensor, the IR-camera did not correctly measure temperatures below $-20℃$.

Consequently, all $T4$ material test have an assumed initial specimen temperature of -30℃. Test $L24/T4/V1$, i.e. the lowest strain rate at this temperature does not experience sufficient heating for specimen temperature to rise above -20℃, and is disregarded.

As expected, increasing the strain rate yields significantly increased heating during plastic flow (Table 5). In fact, the maximum temperature prior to fracture for $10^{-2}s^{-1}$at initial temperatures -30℃ and -15℃ both surpass room temperature, while specimen temperature for the quasi-static test at 25℃ remains largely unchanged.

Table 5: Temperatures measured with IR camera.

Measured specimen temperatures				
Test names	Initial strain rate [$\dot{\varepsilon}_0$]	Initial temperature [℃]	Max. temperature [℃]	Max. temperature difference [℃]
$L01$	$10^{-2}s^{-1}$	27.5	28.5	1.0
$L06$	$10^{-1}s^{-1}$	24.5	37.8	13.3
$L08$	$1\ s^{-1}$	25.0	71.9	46.9
$L35$	$10^{-2}s^{-1}$	-0.5	5.0	5.5
$L38$	$10^{-1}s^{-1}$	0.4	26.5	26.9
$L40$	$1\ s^{-1}$	0.5	58.4	58.9
$L29$	$10^{-2}s^{-1}$	-19.0	-7.5	11.5
$L31$	$10^{-1}s^{-1}$	-14.0	16.0	30.0
$L34$	$1\ s^{-1}$	-17.3	34.2	51.5
$L24$	$10^{-2}s^{-1}$	–	–	–
$L25$	$10^{-1}s^{-1}$	-30.0*	3.2	33.2
$L27$	$1\ s^{-1}$	-30.0*	28.1	57.9

* Initial temperature is assumed.

Specimen heating also seems affected by initial temperature for the initial strain rates used (Figure 31). Reducing initial temperature generally increases largest measured temperature difference, although to a smaller extent than increasing the strain rate. Variations in heating with initial temperature is expected as several material parameters are temperature dependent.

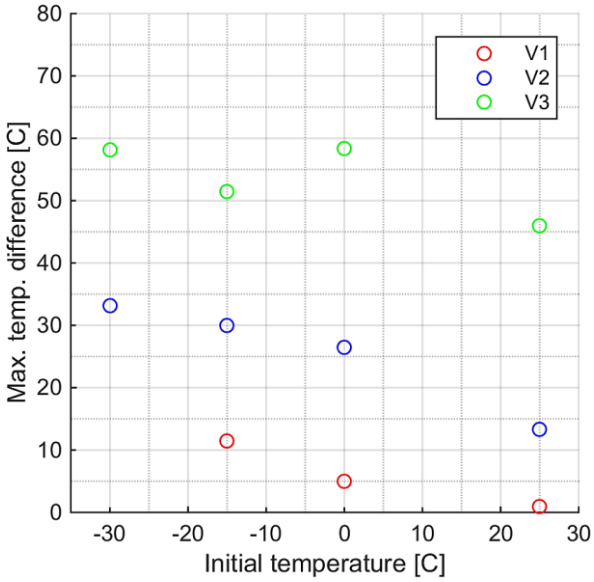

Figure 31: Maximum measured temperature difference in characteristic specimen. The quasi-static test at -30℃ is not included.

Localized temperature softening

The aspect of reduced neck propagation is studied in further detail by comparing temperature development of two material test with the same strain rate and different initial temperatures, namely test $L40/T2/V3$ and $L27/T4/V3$. As illustrated by the material curves in Figure 20 c), test $L27$ experience a reduction in strain hardening approaching failure, exhibiting different behavior than other tests. In Figure 21, specimen images just prior to failure revealed that both test $L27$ and $L34$ does not fully propagate the neck, but rather experience failure with limited cold drawing.

By comparing specimen heating for test $L27$ and $L40$ at the same amount of elongation (Figure 32), the heat localization phenomena is easily observed. Plastic deformation, and thus heating, affects the entire gauge in Figure 32 a) while it remains confined to the initial neck in Figure 32 b). The temperature difference is substantially higher in the localized region: 58℃ for $L27$, compared to 18℃ for $L40$.

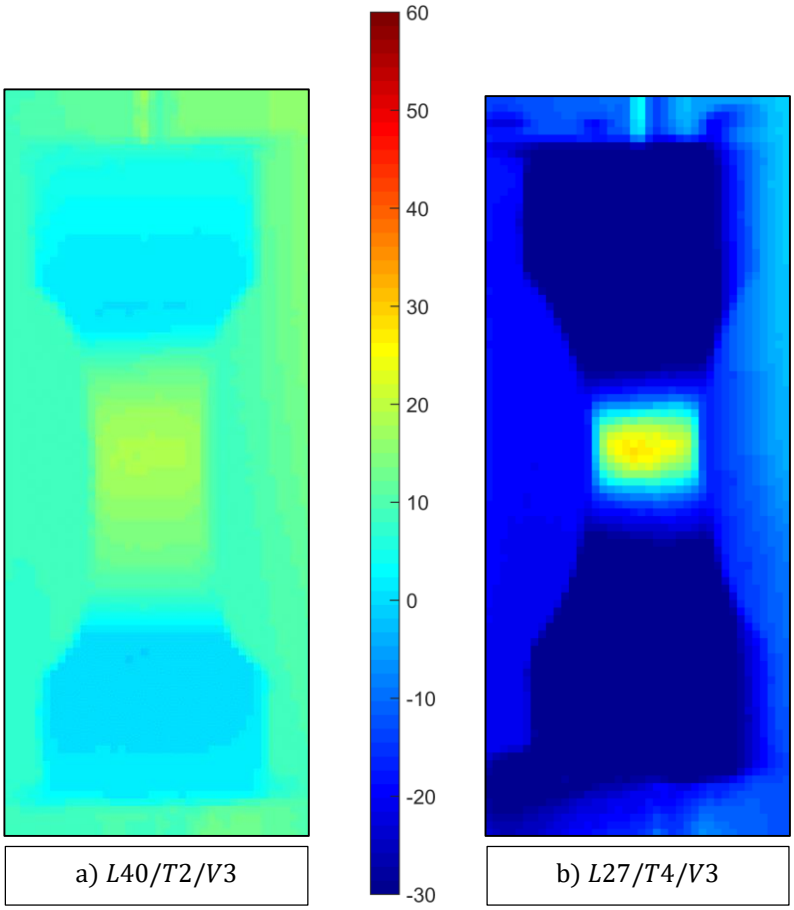

Figure 32: Temperature map comparison for different initial temperatures at equal elongation. Figure a) and b) shows temperature map for initial temperatures $0℃$ and $-30℃$, respectively. Figure b) shows the temperature map just prior to fracture, while figure a) shows the temperature map at corresponding amount of deformation. Strain rate for both tests is $1s^{-1}$.

As stated by P. I. Vincent [16], cold drawing is prevented by insufficient strain hardening, and may be caused by adiabatic heating from high strain rates. Based on the temperature map in Figure 32, it seems plausible that the necked region experience enough heating such that the strain hardening is insufficient for futher drawing. This in turn will cause the specimen to fail before full cold drawing is achieved, as observed for the material tests herein. Is it also possible that plastic deformation is localized to the neck by other mechanisms, with increased heating as a consequence rather than a cause for failure.

Comparing temperature maps exactly prior to fracture for both test also indicates localization of specimen heating in test $L27$ (Figure 33). Results indicate that low initial temperature may limit neck propagation in polypropylene drawn at high strain rates, caused by localizing heating and plastic flow of the initial neck with little subsequent cold drawing.

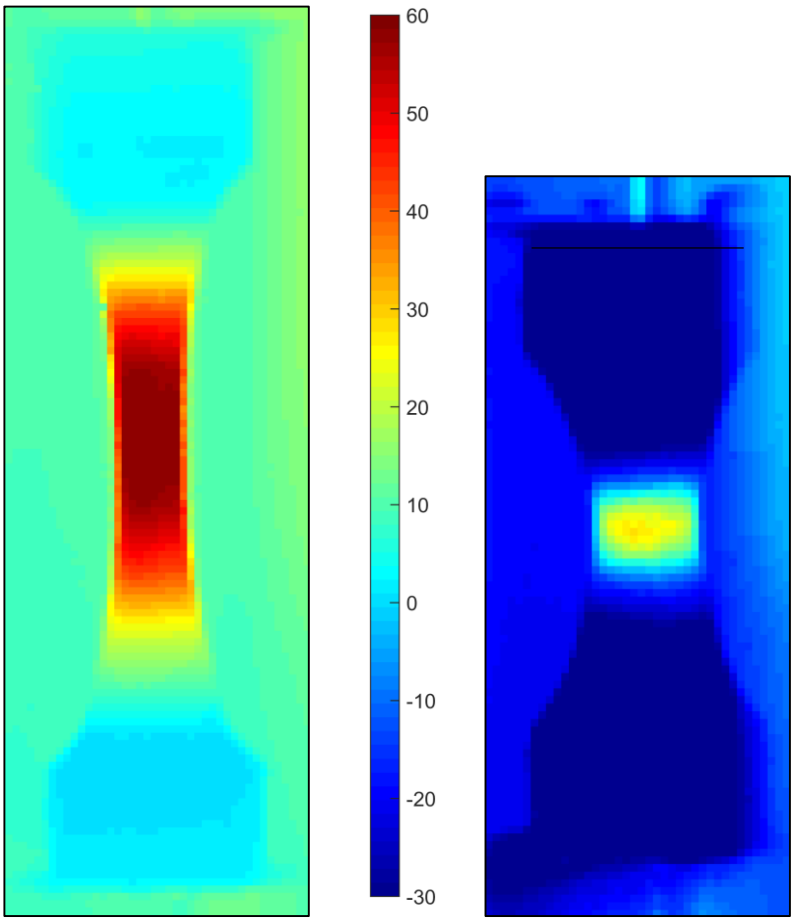

Figure 33: Temperature map comparison for different initial temperatures. Figure a) and b) show specimen temperature map immediately prior to fracture for initial temperatures 0℃ and -30℃, respectively. Heating is restricted to specimen gauge in figure b), with limited neck propagation. Strain rate for both tests is $1s^{-1}$.

5.1.5 SEM results

Using a scanning electron microscope (SEM) the microscopic structure of polypropylene specimen was examined for cavitations and possible crazing (Figure 34). A tensile test specimen was used, drawn at quasi-static strain rate (10^{-2} s^{-1}) at room temperature. The specimen was drawn a total of 12.5 mm, sufficient for both yielding and some plastic flow, before being unloaded. For overview, deformation of 12.5 mm for test $L01$, another test performed with the same test conditions, caused approximately 1.2 longitudinal true strain.

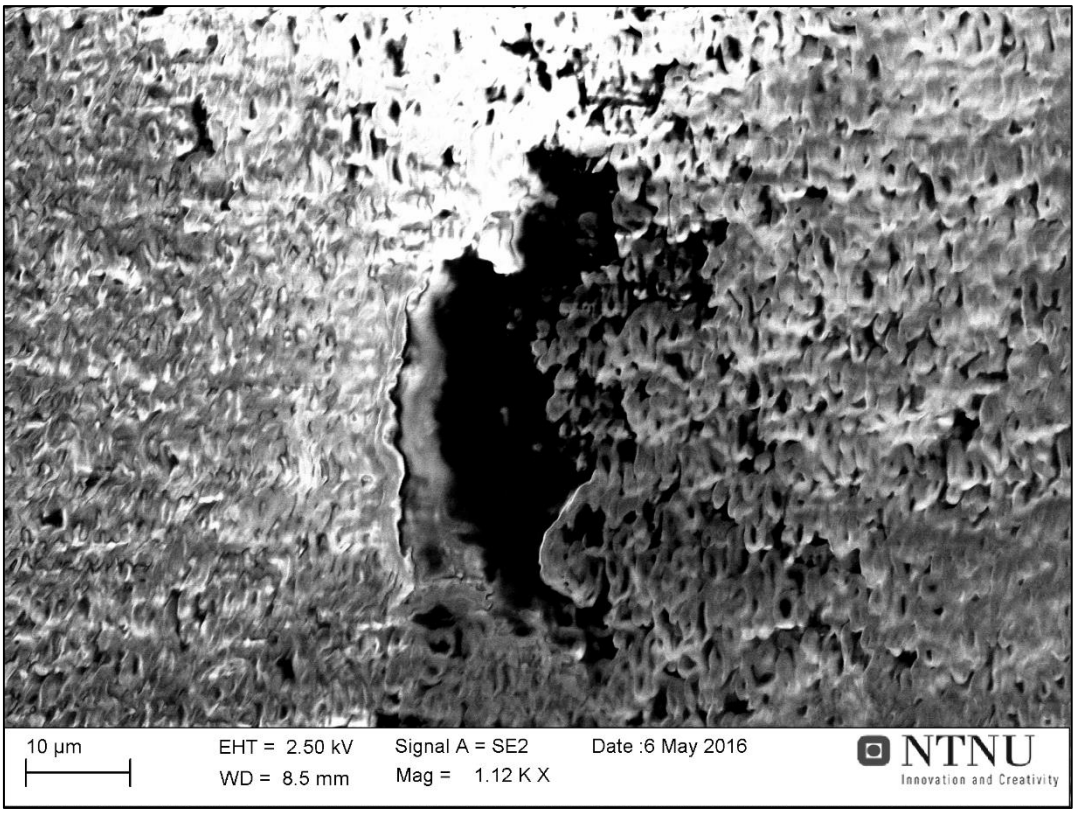

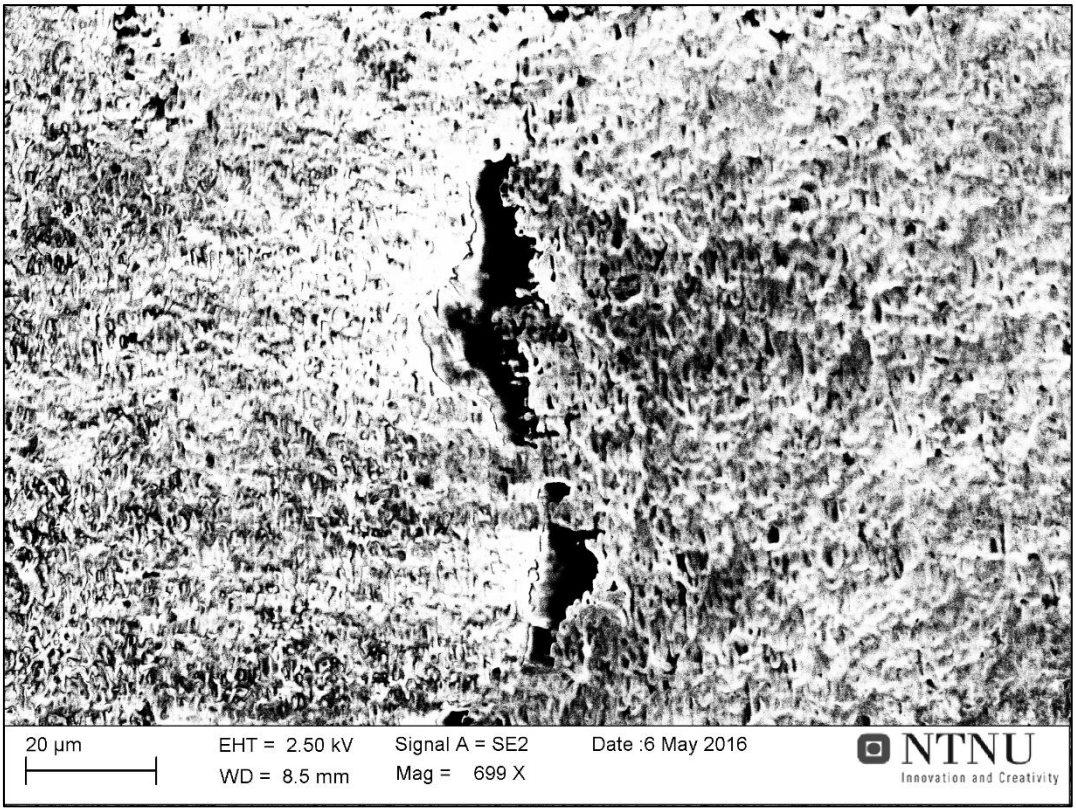

Figure 34: SEM pictures for tensile specimen with quasi-static strain rate, at room temperature.Draw direction of specimen is north/south. Small voids (black 'dots') are observed everywhere in the specimen. Voids are assumed to coalesce, forming the large cracks observed in both pictures.

SEM pictures from figure 32 clearly shows cavitation of the specimen, as indicated by the small black ‘dots’ evenly distributed in specimen. When drawing polymers, some voids will coalesce, forming larger cavities or crazes [21]. The larger black shaped regions are assumed such cavities formed through coalescence, which will further develop with specimen elongation. The specimen experienced noticeable stress whitening, and stress whitening was reported for preliminary test at other temperatures. It is assumed that voids are formed for all combinations of initial temperature and strain rate.

With no voids perpendicular to the draw direction, it is suspected that little to no crazing occurs for the specimen presented in Figure 34. Whether crazing occurs at lower initial temperatures and higher strain rates is unknown, as only one SEM test is included herein.

5.2 Compression tests

Compression tests were performed to determine material pressure sensitivity, denoted α. Small cylindrical test specimen where used for the compression test (Figure 35), using eCorr point tracking to measure specimen deformation, and edge trace to measure transverse displacement. The test setup is otherwise similar to the uniaxial tensile tests, using the Intron machine to load the specimen and the PC-chamber and nitrogen to lower the temperature (Figure 36). Specimen were not fastened to the machine, but used a combination of tape and oil in an attempt to recreate frictionless boundary conditions.

Figure 35: Compression test specimen. The specimen has a diameter and height of 6 mm. The top and bottom surface is layered with tape to reduce friction.

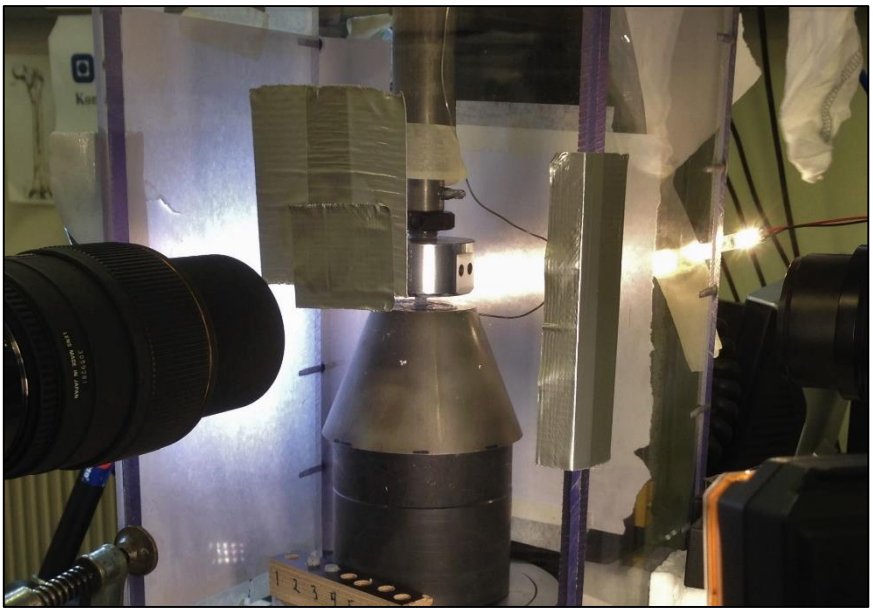

Figure 36: Compression test setup. The specimen is enclosed in a polycarbonate chamber and cooled using nitrogen.

Stress-strain curves from compression test are categorized by initial temperature (Figure 37). Curves are plotted for a reduced range of values, since data measured in the plastic domain quickly becomes erroneous and irrelevant. Compression tests use the same yield definition as tension test, i.e. intrinsic yield stress. Yield stresses are calculated from the characteristic tests (continuous curves).

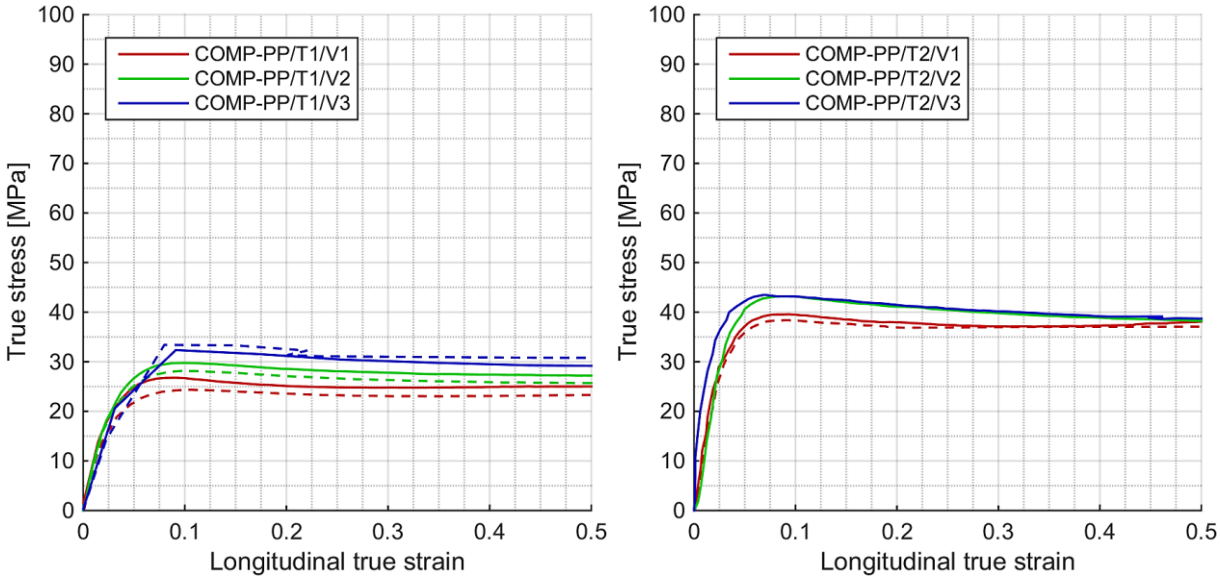

a) 25℃

b) 0℃

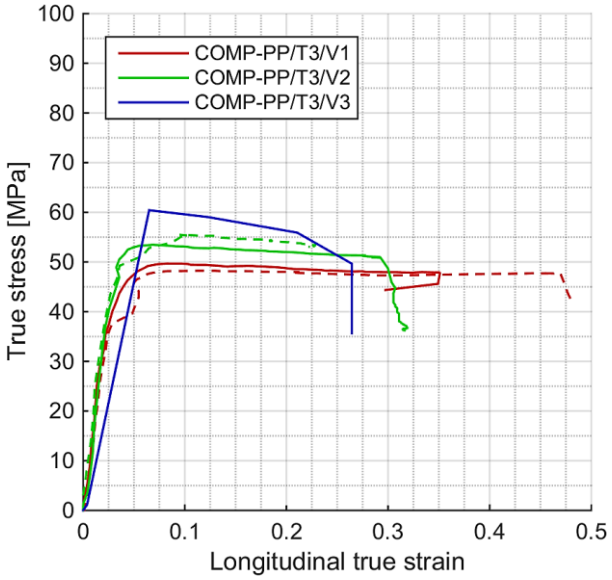

c) − 15℃

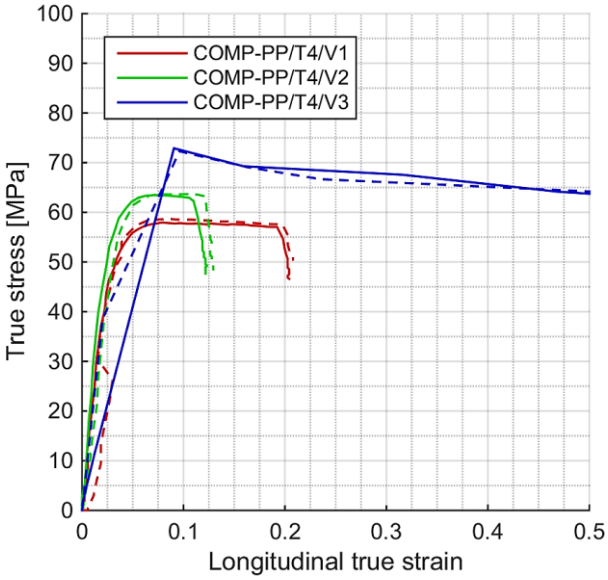

d) − 30℃

Figure 37: Temperature categorized stress-strain plots for compression tests.. Dashed line represents a corresponding material test performed at the same temperature and strain rate.

Comparison of tension and compression test T1/V1 shows that the elastic domain is quite similar (Figure 38). Both curves has almost equal initial slope, indicating similar values of Young's modulus and both curves show slight strain softening.

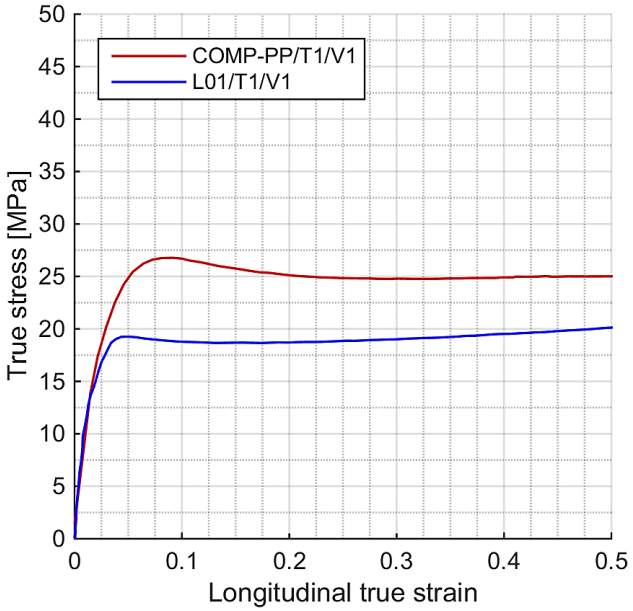

Figure 38: Comparison of compression and uniaxial tension tests. Both tests are performed at room temperature, using initial quasi-static strain rate.

Using yield stresses from both tension tests (Figure 24) and compression tests, the pressure sensitivity may be calculated for each combination of initial temperature and strain rate (Table 6). Note that material tests with the highest strain rate have very few data points and may yield imprecise yield stress values.

Table 6: Calculated presurre sensitivity

	T1: 25℃	T2: 0℃	T3: −15℃	T4: −30℃
V1: $10^{-2}s^{-1}$	1.38	1.63	1.77	1.70
V2: $10^{-1}s^{-1}$	1.43	1.67	1.73	1.71
V3: $1\ s^{-1}$	1.45	1.54	1.74	1.72

5.3 Laser flash tests

Specific heat capacity, one of the parameters required for numerical simulations, was determined by the laser flash method [36]. The analyses were performed by SINTEF, using five cylindrical specimens with a diameter of $12.7\ mm$ and a thickness of $0.5\ mm$. The specimen were tested at temperatures $25℃, 35℃$ and $50℃$. Due to limitations of the testing apparatus, no test were performed below room temperature. Calculated specific heat capacity:

$$C_p = 2756 \frac{J}{kg \cdot K}$$

6 Numerical simulation

Using FEA software Abaqus, numerical simulations of the uniaxial tension tests were performed for every combination of initial temperature and –strain rate. The primary goal of the simulations is to validate laboratory tests results by comparing stress-strain curves and volumetric strain curves..

Simulations uses the material model presented in chapter 3, with plasticity parameters calibrated for each initial temperature. Accuracy of the model is assessed by comparing results to material testing and through sensitivity analysis.

6.1 Abaqus setup

In terms of deformation, most uniaxial tension test are similar irrespective both initial strain rate and temperature. For the uniaxial tension test performed herein, all specimens neck in the middle gauge and elongate with varying degrees of cold drawing with some barely drawing at all. As a result, the same underlying Abaqus model have been used for all simulations of uniaxial tension tests, i.e. same mesh size, element type and analysis type.

6.1.1 Dynamic explicit

The chosen method of analysis is dynamic explicit for its suitability in modeling large deformations and adiabatic heating [37]. The main drawback of explicit integration method is the conditionally stable time increment, resulting in an increasing number of required iterations as mesh element size decreases. This may be alleviated by mass scaling, increasing the size of the stable time increment:

$$\Delta T_{CR} = L_e \sqrt{\frac{\rho}{E}}$$

Where L_e is the length of a critical size mesh element, ρ is density and E is Young's Modulus. Since adiabatic heating is rate dependent, mass scaling is preferred to other scaling methods as it preserves the natural time scale [37]. Mass scaling used herein is uniform, i.e. the material density is scaled for the whole model. No dynamic effects of mass scaling has been observed for simulations performed.

6.1.2 Mesh

The test specimen were discretized using an axisymmetric model with CAX4R elements[1]. Using symmetry, the specimen was modeled as 2D planar upper section of the element, with sweep and mirror features to illustrate the specimen in 3D (Figure 39). With no bending or buckling, linear order elements are well suited for the analysis, providing sufficient accuracy at low computational cost. The elements are also well suited for dynamic explicit analysis [37].

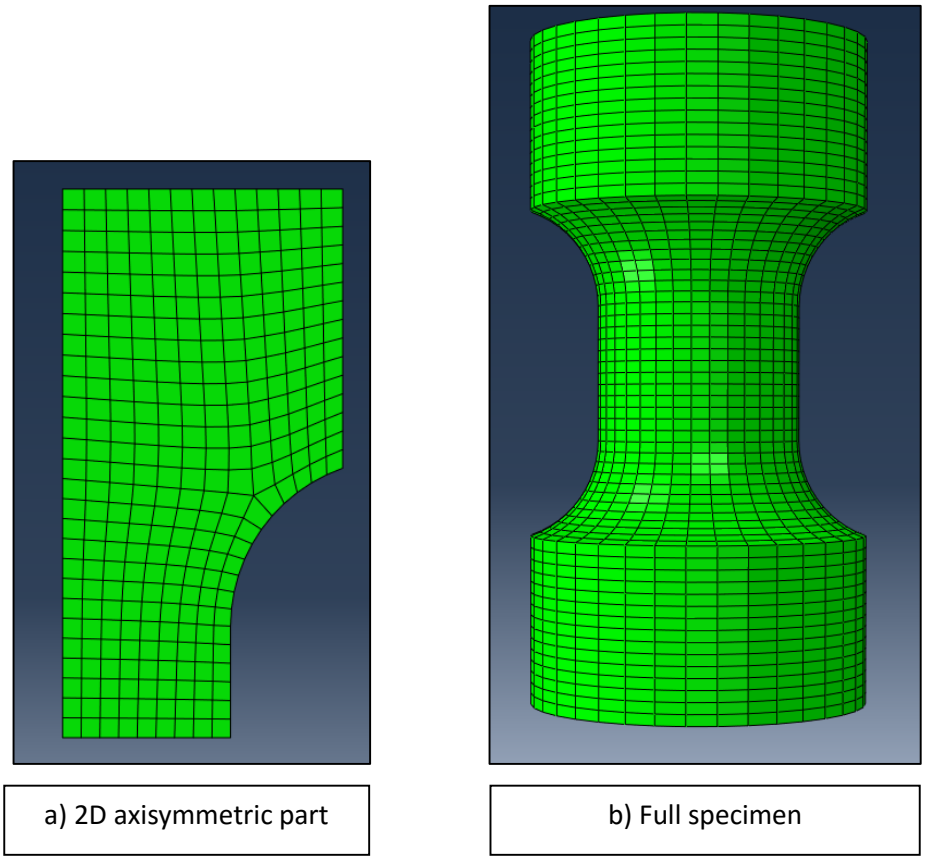

Figure 39: Mesh seed illustration. Figure a) shows the 2D planar view of the mesh, as modeled on the axisymmetric part. Figure b) shows a full 360-degree sweep and mirror visualization of the axisymmetric element.

Sensitivity analysis

Mesh element size is particularly important for an explicit analysis. A coarse mesh consisting of larger elements will reduce increase the critical time step, but might also reduce accuracy. Optimal mesh size was estimated using mesh sensitivity analysis; the goal is to find a number of mesh elements that provide sufficient accuracy.

[1] CAX4R: A 4-node bilinear axisymmetric quadrilateral, reduced integration, hourglass control.

Mesh sensitivity is evaluated by comparing reaction force and logarithmic strain values for different mesh densities. Strain values are calculated from the bottom right mesh element (Figure 40).

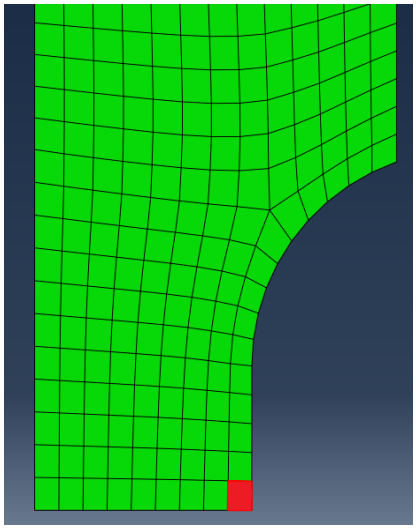

Figure 40: Mesh sensitivity strain element.

The mesh sensitivity analysis were complicated by influence of mesh size on material fracture. Increasing the mesh size caused earlier onset of fracture, making is difficult to use maximum stress values to evaluate mesh sensitivity. Instead, values for reaction force and longitudinal strain are calculated from same amount of specimen elongation in each mesh analysis (Table 7).

Table 7: Reaction force and longitudinal strain for various mesh densities.

Number of mesh elements	Reaction force [kN]	Longitudinal strain
160 (coarse)	493.8	1.6426
251 (average)	487.8	1.6149
432 (fine)	491.8	1.6094
608 (very fine)	495.6	1.6135

There is some variance in both strain and reaction force as the mesh is refined, and the results does not seem to converge towards a single value for either. It is likely that the coupling between mesh element size, damage and stresses causes the variance in fracture, and consequently in calculated reaction force and longitudinal strain. Changing damage evolution to uncoupled might reduce this problem. The analysis results are similar nonetheless, and it is assumed that

mesh size has little influence on the accuracy of the analysis. Average mesh size has been used in all further simulations.

6.1.3 Material parameters

Most material model parameters are calculated based on the material testing results in chapter 5, including Yield stress, Young's modulus, contraction ratio, rate sensitivity, pressure sensitivity and specific heat capacity. Density is given in the product data sheet[7]. Associate professor David Morin at the department of structural engineering, NTNU, performed calculations of the remaining plasticity parameters for each initial temperature.

The only parameters not directly calculated are D_C, β_D and β_T, i.e. critical damage, plastic dilation and the Taylor Quinney coefficient. The critical damage parameter is determined iteratively such that it causes material fracture at approximately the same amount of longitudinal strain as laboratory tests. Iterations were performed individually for every temperature-strain rate combination. The plastic dilation parameter is not determined analytically due to the viscoelastic nature of polypropylene, making it unfeasible to separate elastic strain contributions from plastic ones. The Taylor Quinney coefficient is simply assumed one.

Regarding determination of plastic dilation, we know from Figure 29 that the contraction ratio is not constant but increases steadily in the plastic domain. Additionally, the volumetric strain has been shown to "level off" and even decline as it approaches failure for most test conditions (Figure 23). The material testing results indicate significant changes in the dilatational response as the specimen deform, and it becomes apparent that a constant β_D is a large assumption, and a possible weakness for simulations of PP. Consequently, a sensitivity analysis of β_D was performed (Figure 41).

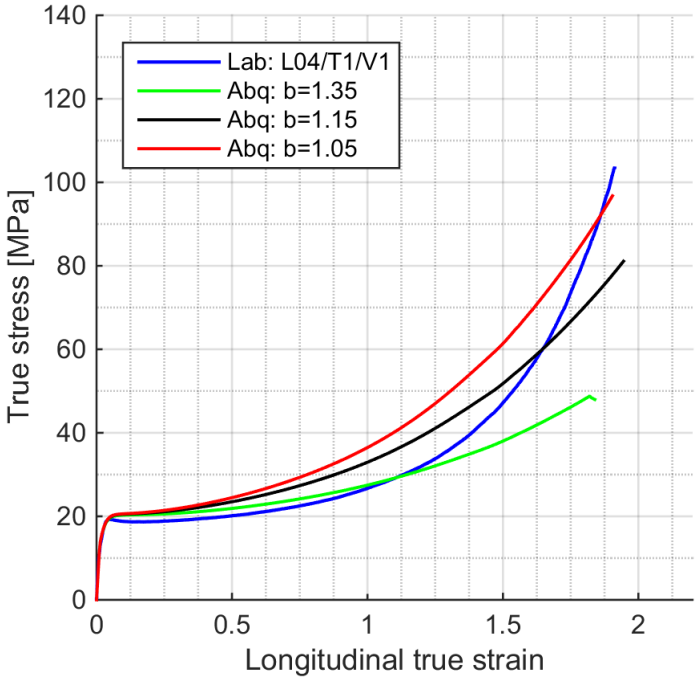

Figure 41: Sensitivity analysis of plastic dilatation. Blue curve shows the laboratory uniaxial tension test. Remaining curves shows numerical simulation results in Abaqus for different values of β_D. All curves use initial temperature 25℃ and quasi-static strain rate.

Dilatational response is clearly dependent on β_D. Reducing the parameter yields an increase in transverse strain, which in turn yields larger stresses in the plastic domain. For correct simulations of the material response, β_D must change as the specimen deforms. Additionally, the model currently cannot account for the decline in volumetric strain when approaching failure, as shown for some tests in Figure 23.

The choice of β_D and D_C values in simulations was based on the following criteria: the combination of β_D and D_C must cause fracture at roughly the same amount of longitudinal true strain as laboratory material tests. Parameters were determined iteratively by running simulations and updating the parameters. As this strategy was very time consuming, only a few iterations were performed for each test. Further iterations to determine β_D and D_C might provide more coinciding results between simulations and material testing early in the plastic domain. All material parameters used in Abaqus simulations are presented in Table 8.

Table 8: Material parameter values used in numerical simulations

Elasticity				
Parameters	25℃	0℃	−15℃	−30℃
E	1100	2030	2250	3200
ν	0.24	0.24	0.24	0.24
Plasticity				
Parameters	25℃	0℃	−15℃	−30℃
α	1.38 , 1.43 , 1.45	1.63, 1.67 , 1.54	1.77 , 1.73 , 1.74	1.70 , 1.71 , 1.72
σ_T	12.67	23.93	20.0	15.83
β_D	1.20 , 1.40 , 1.40	1.34 , 1.55 , 1.50	1.55 , 1.60 , 1.68	1.41 , 1.43 , 1.70
θ_{R1}	759.8	3996.0	5070.0	2848.0
θ_{R2}	−231.3	20.49	−4314.0	22.51
θ_{R3}	10.16	−2529.0	24.7	13.6
Q_{R1}	10.3	31.89	17.81	8.344
Q_{R2}	−3.141	−15.1	−9.786	−14.61
Q_{R3}	−6.581	−23.96	−17.45	$-1.548e6$
C	0.0393	0.0390	0.0582	0.0565
$\dot{p_0}$	0.02	0.02	0.02	0.02
Damage				
Parameters	25℃	0℃	−15℃	−30℃
D_I	0	0	0	0
D_C	0.57 , 0.58 , 0.63	0.66 , 0.69 , 0.69	0.72 , 0.72 , 0.70	0.61, 0.65 , 0.62
Adiabatic Heating				
Parameters	25℃	0℃	−15℃	−30℃
β_T	1	1	1	1
C_p	2756	2756	2756	2756
ρ	900	900	900	900

Comma separated values denote parameters used for each strain rate, ranging from V1 to V3.

Units are [N], [mm], [s], [kg]

6.2 Results and comparison

Specimen deformed similar to the laboratory tests: initial necking followed substantial drawing and neck propagation of the specimen (Figure 42). At sufficient levels of damage ($D = D_C$), the material fractures.

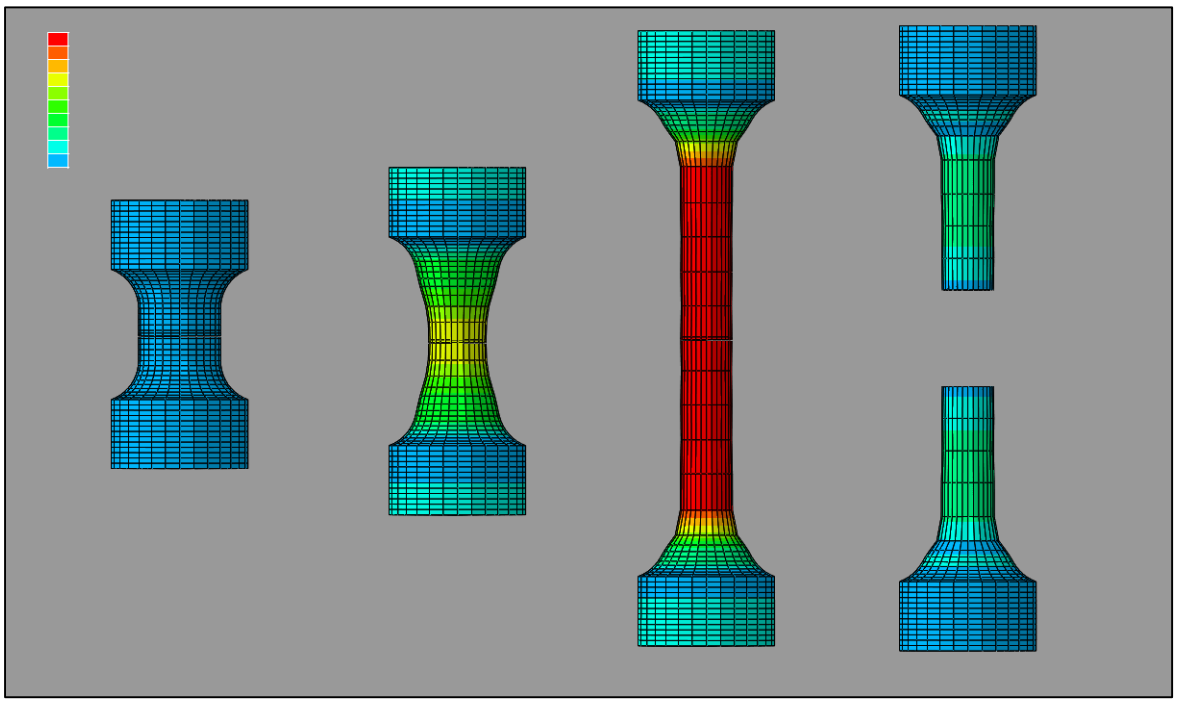

Figure 42: Specimen deformation in Abaqus. Figure shows specimen deformation history for test using room temperature and quasi-static conditions ($T1/V1$): from undeformed element on the left, to fractured element on the right. Color gradient shows stress levels in draw direction, from zero to high.

Abaqus simulations are compared with the corresponding uniaxial tension tests for every combination of initial strain rate and temperature. Only the characteristic material testing curves are used for comparison. The simulations uses reaction force to calculate stress-strain curves, such that the method of calculation is equal to laboratory tests. Both longitudinal strains and transverse displacement are measured from bottom right mesh element (Figure 40). All comparisons of true stress and volumetric strain are shown in figures 42-53. Larger versions of all figures may be found in Appendix: 9C.

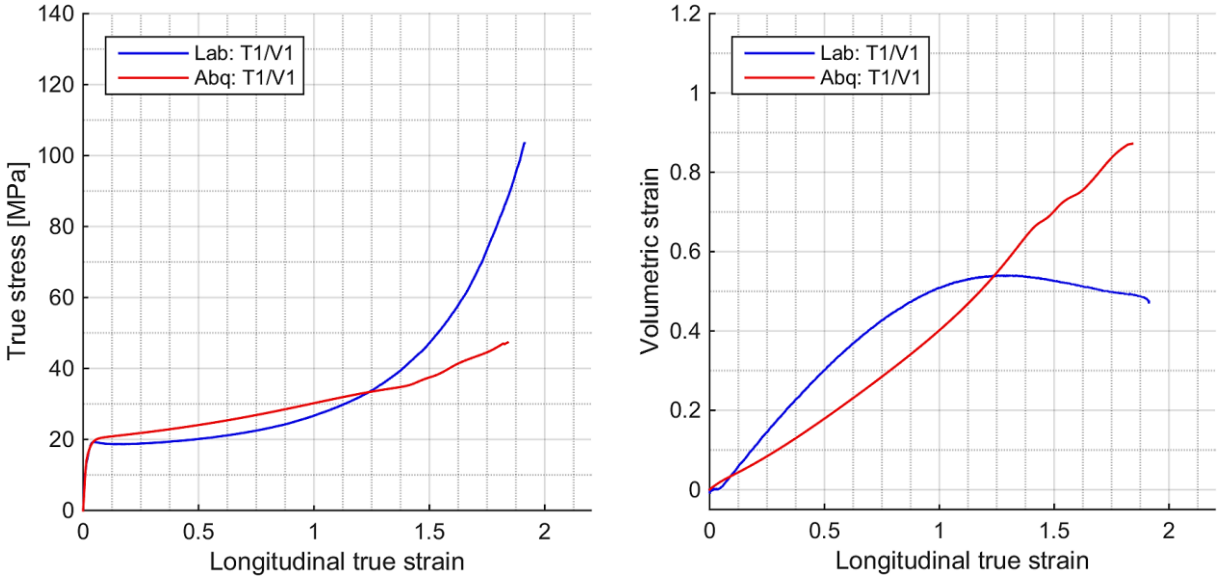

Figure 43: Comparison T1/V1.

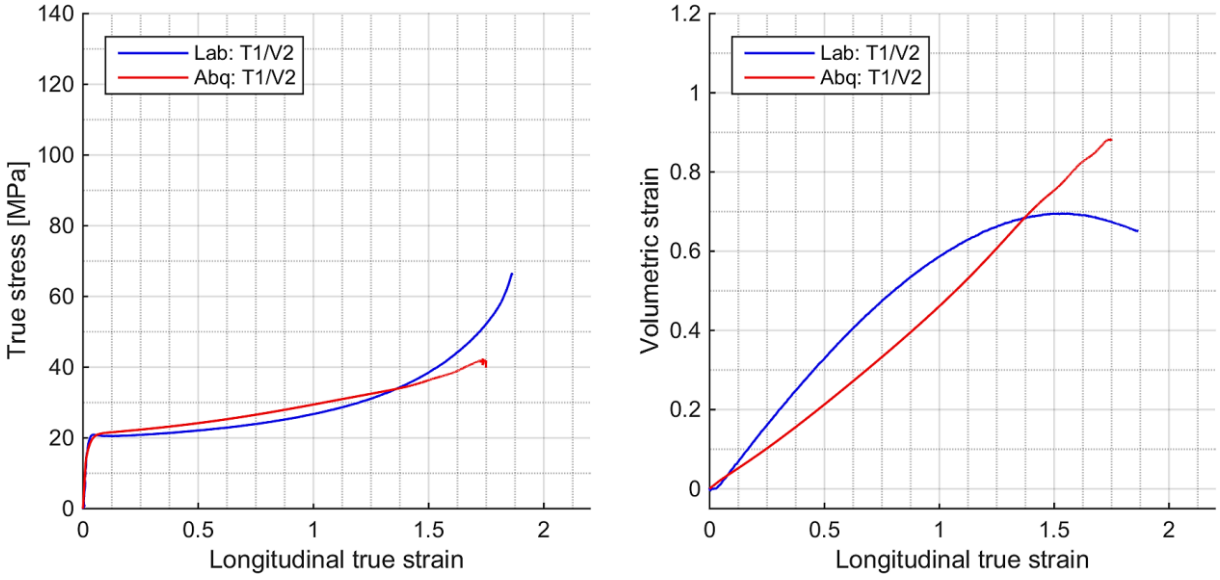

Figure 44: Comparison T1/V2.

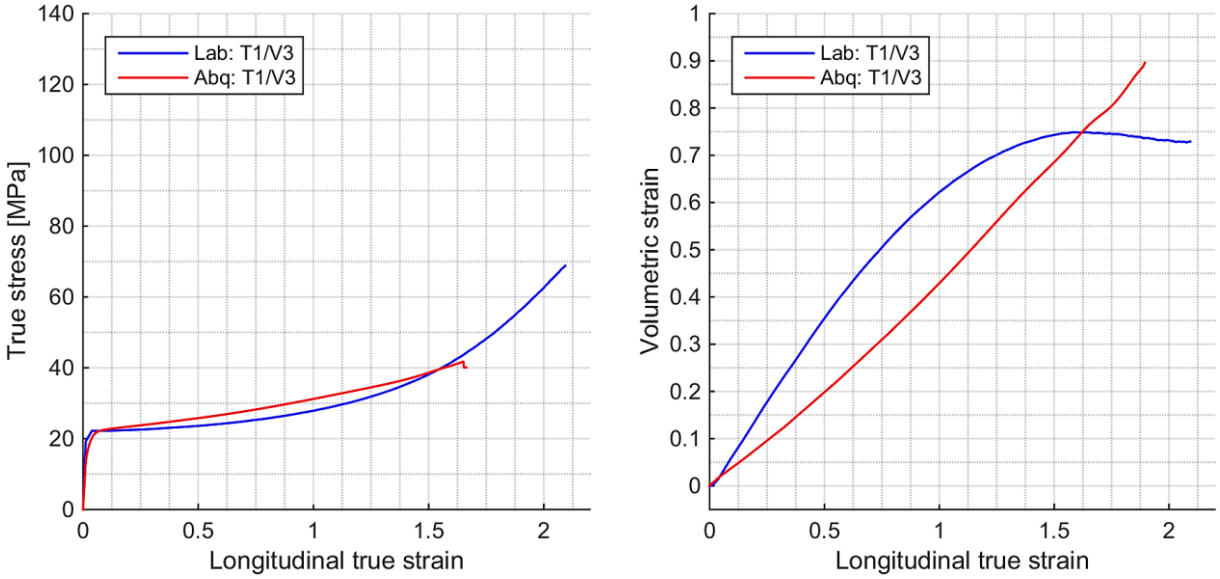

Figure 45: Comparison T1/V3.

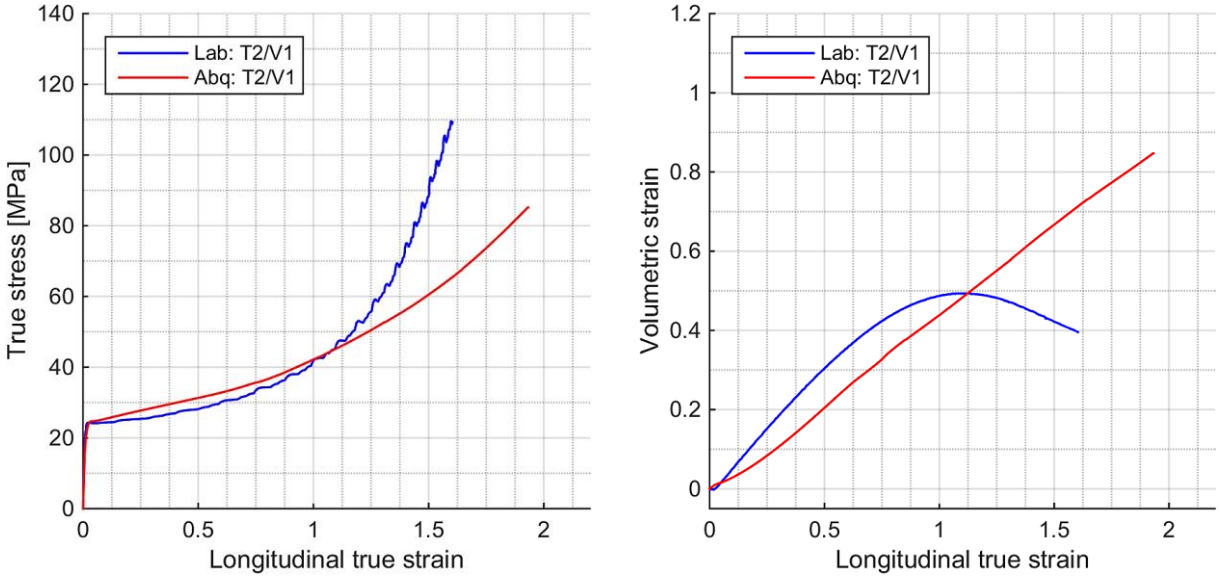

Figure 46: Comparison T2/V1.

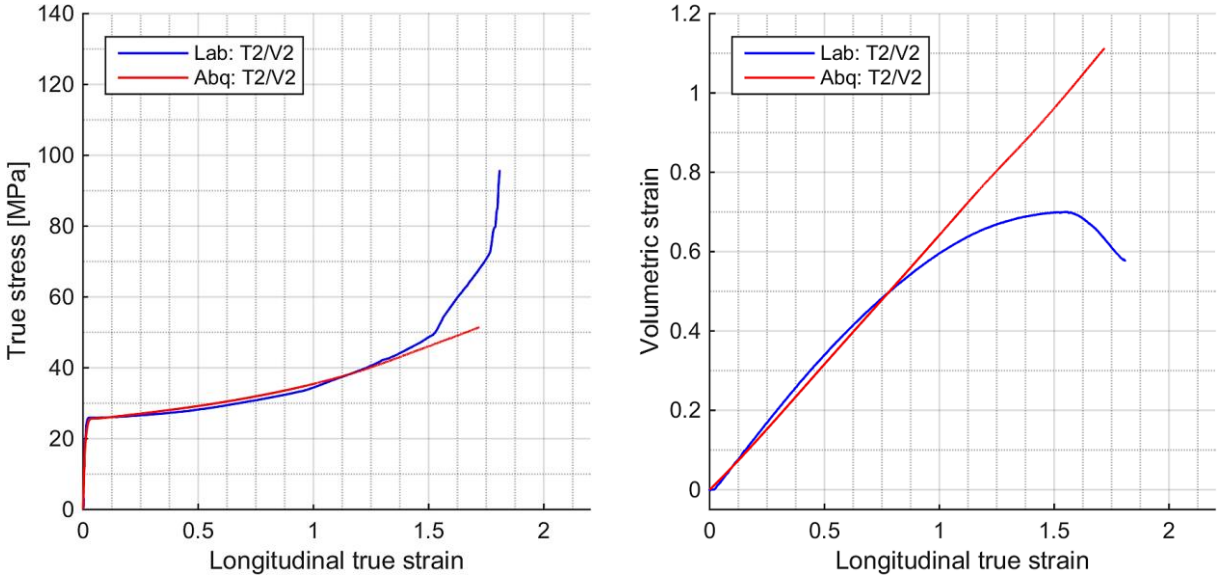

Figure 47: Comparison T2/V2.

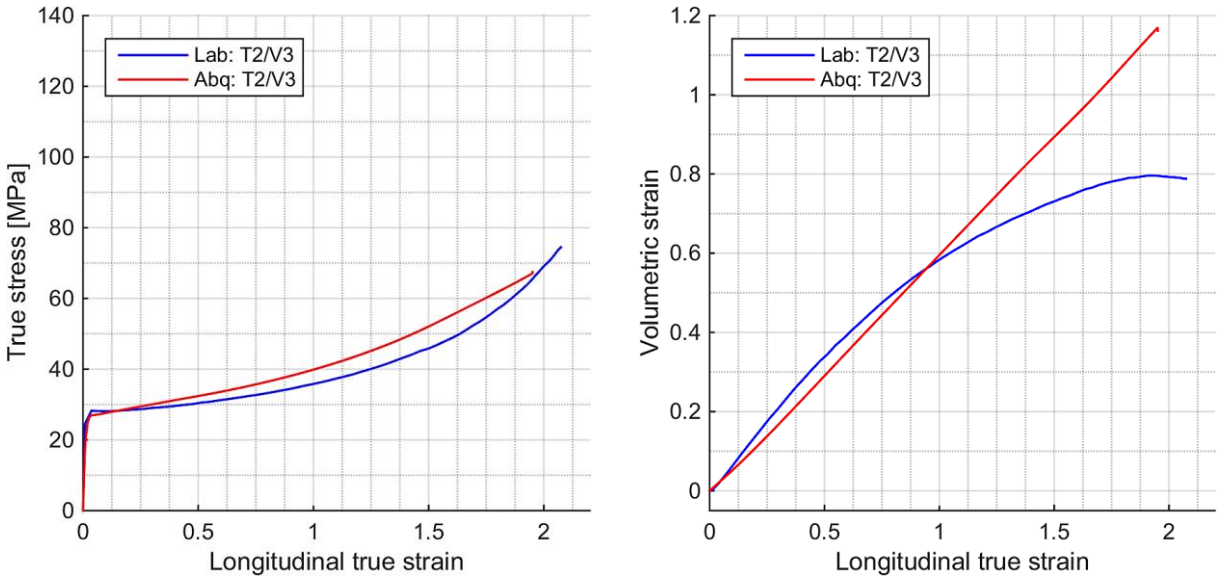

Figure 48: Comparison T2/V3.

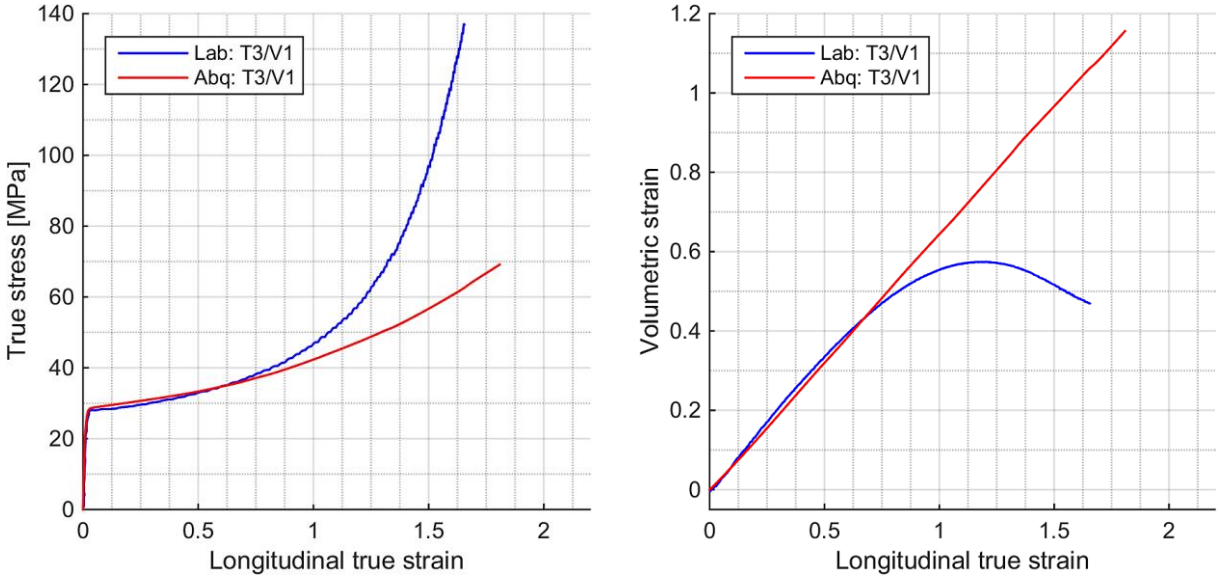

Figure **49: Comparison T3/V1.**

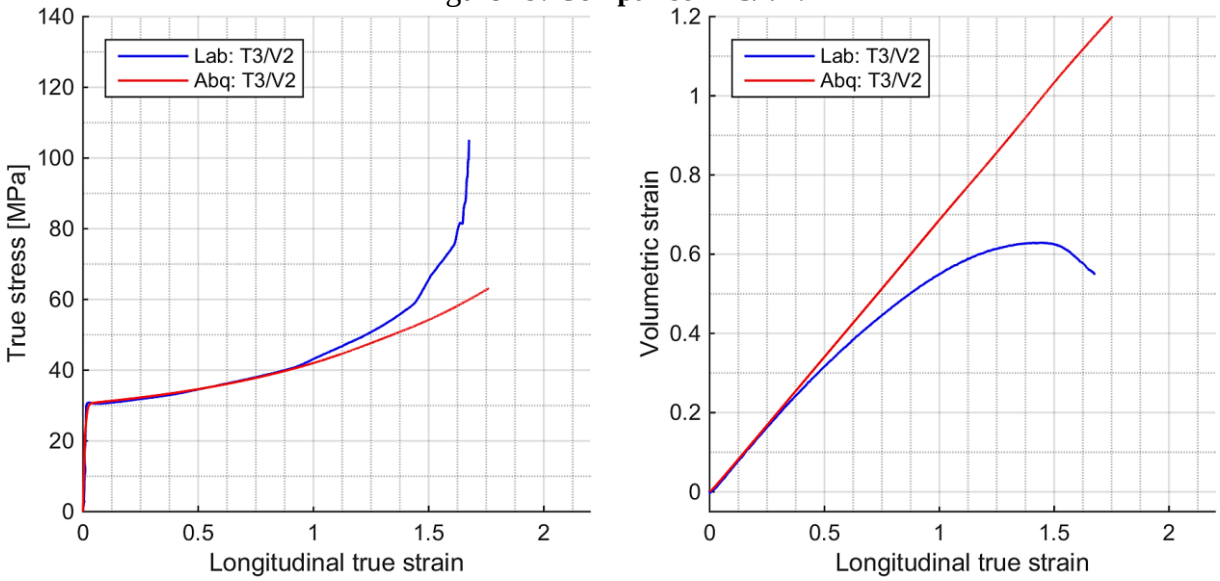

Figure 50: Comparison T3/V2.

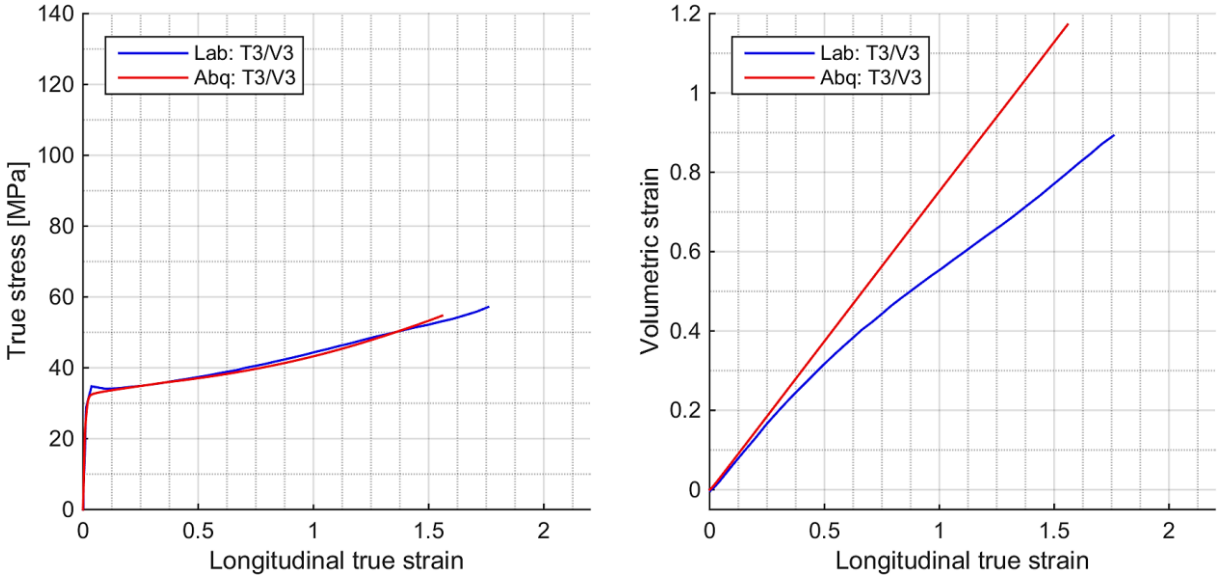

Figure 51: Comparison T3/V3.

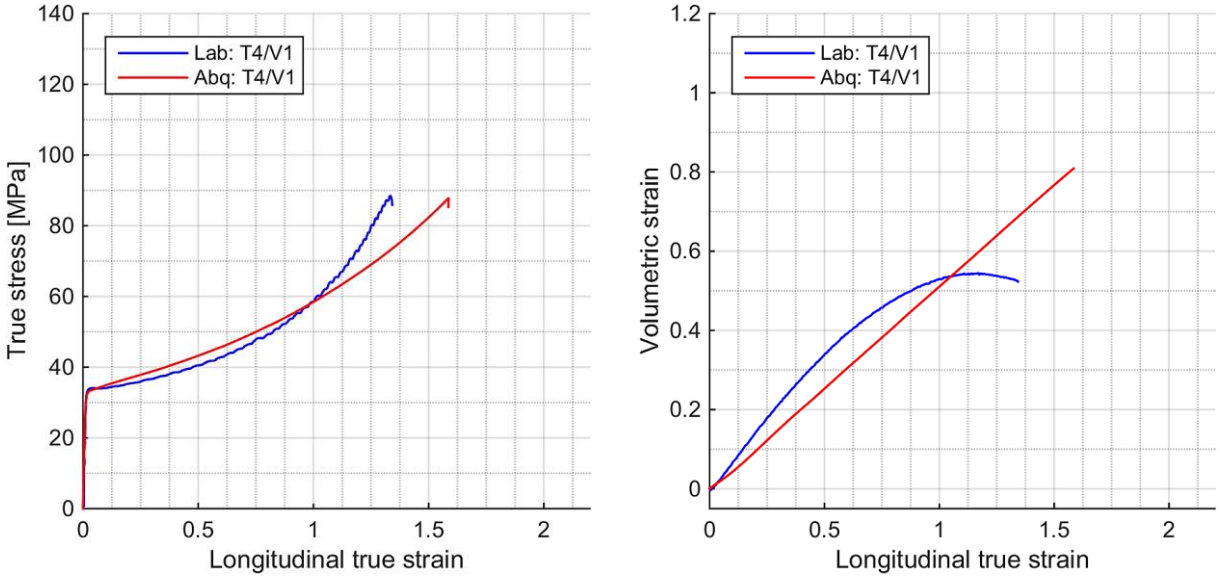

Figure 52: Comparison T4/V1.

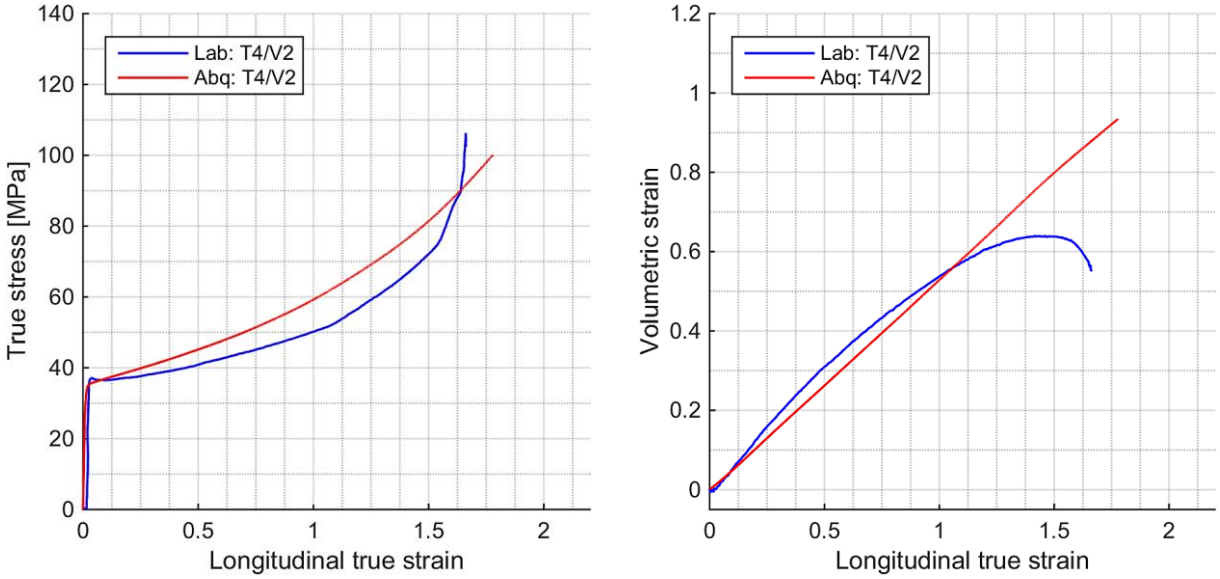

Figure 53: Comparison T4/V2.

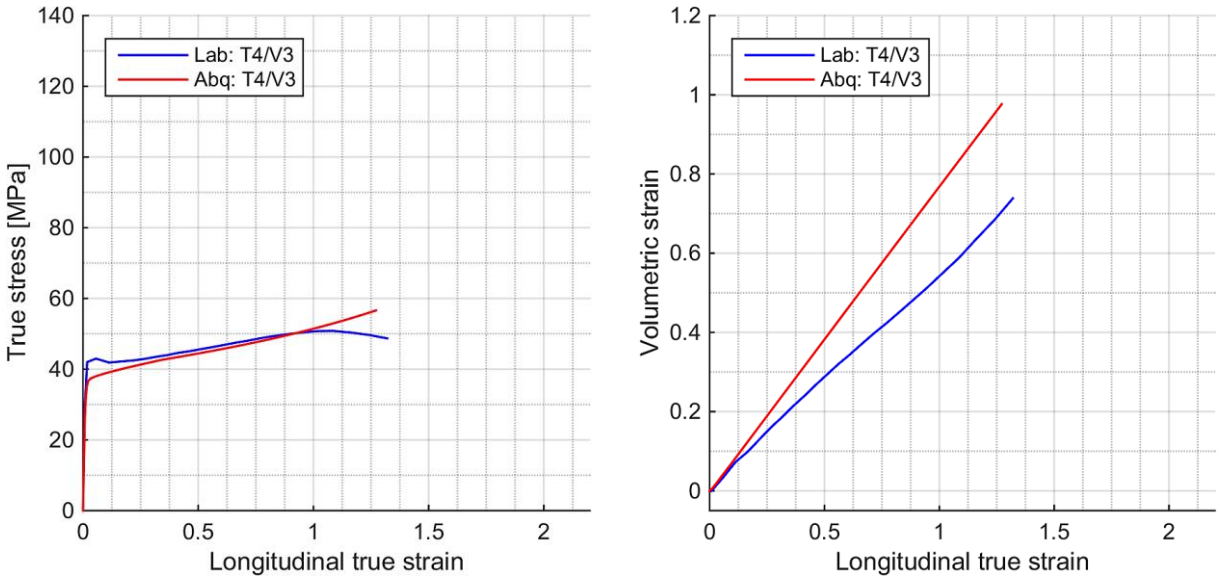

Figure 54: Comparison T4/V3.

Temperature

With the poor accuracy for most stress-strain curves, temperature calculations in Abaqus will be imprecise. The maximum temperature difference is reported for initial temperature of 25℃ and −15℃ (figure 49-51). Temperature was calculated from the bottom right mesh element (Figure 40). Results are presented in Table 9.

Table 9: Maximum temperature difference for simulations at −15℃

	V1	V2	V3
Initial temp. 25℃ (T1)	32.11	29.36	45.14
Initial temp. −15℃ (T3)	59.97	58.14	48.68

For low strain rates the heating is vastly overestimated when compared to heating measured with the IR-camera (Table 5). The material model uses an adiabatic heating assumption for calculations, i.e. no heat transfer, but it seems that for lower initial strain rates the material indeed dissipates a lot heat to the surroundings. When initial strain rate is increased, assuming adiabatic heating becomes less erroneous since the material has little time to dissipate the heat.

For the highest strain rate, the values in Table 5 and Table 9 are similar in order of magnitude. Likely source of error between them are incorrect stress and volumetric strain values simulations. Additionally, the mesh element chosen for temperature calculations in Abaqus may have a different position than maximum measured temperature for laboratory results.

6.3 Discussion

Comparison between Abaqus simulations and material testing results reveal that the SIMLab polymer model does not accurately capture the material behavior of the polypropylene compound for the material parameters used. Observations and model strategy is discussed below.

The largest weakness of the model is the assumption of constant plastic dilatation (β_D). All the simulations elongate with an almost constant increase in volumetric strain, yielding incorrect values for the transverse strain – and consequently the true stress – when approaching failure. This effect is well illustrated in figures 47-50; initially, simulations and laboratory tests values

coincide for both volumetric strains and stresses. As the specimens deform, contraction ratio of laboratory specimen increases while Abaqus simulations do not, and the results diverge.

Effect of constant β_D may also be observed in figures 45, 48, 51 and 54. Simulation with the highest initial strain rate seem to yield better approximations of the stress at all initial temperatures even though the volumetric strain is incorrect. Most of these curves have significantly less change in contraction ratio approaching failure, and assuming constant plastic dilatation becomes less erroneous.

Response of test $T3/V3$ and $T4/V3$ has dissimilar accuracy between the stress and volumetric strain response, where simulation results closely correspond for stresses but not for volumetric strains. Material testing results in 5.1 showed that specimen experience reduced neck propagation, possibly due to either localized temperature softening or a ductile to brittle transition, neither which is included in the material model. Some dissimilarity is expected. Additionally, temperature dependence during elongation is not included in simulations; the material is calibrated for each initial temperature instead. This might affect material tests at high strain rates, which have been shown to experience quite substantial heating (Table 5).

Simulation accuracy will undoubtedly improve by including variable β_D to capture the change in dilatational response, especially for lower strain rates. Specimen heating might still cause some inaccuracy between material tests and simulations. Another potential source of error is mesh density, which has been found to affect the onset and location of fracture.

7 Conclusions

Overall, the material response of the polypropylene compound agree with existing theory for semi-crystalline polymers in the glassy domain, having shown strong dependence on both temperature and strain rate. Uniaxial tensile testing revealed that the material response becomes increasingly brittle when lowering initial specimen temperature, as indicated by the increase in yield stress, increase in plastic stresses and reduction in longitudinal strain. Increasing the strain rate would also increase yield strength, while decreasing plastic stresses due to specimen heating.

The only large deviation from this general trend was reduced cold drawing for specimen with low initial temperature at the highest initial strain rates, where the specimens would fracture at lower levels of strain and stresses than expected. Localized temperature softening and increasing influence of crazing have been proposed as possible explanations. Lack of SEM results for specimen at low initial temperature and high strain rates makes it difficult to evaluate if the material crazes, and is recommended for further study. Based on IR-camera results localized temperature softening of the initial neck seems likely.

Numerical simulations in Abaqus using the SIMLab polymer model did not yield accurate results for the plastic response. A clear weakness of the model is the assumption of constant plastic dilatation, which does not account for the large change in volumetric strain response approaching failure for most test conditions. Updating the material model to include a variable plastic dilatation should significantly improve accuracy of the simulations. The model also seems sensitive to the interaction between choice of critical damage parameter and mesh density. Further sensitivity analysis of mesh density and integration method is recommended.

Contraction of cavitation-voids was reported as a possible explanation for the decline in volumetric strain in figure Figure 23. Although these voids are expected to from for all the temperatures and strain rates used in material testing, SEM testing was only performed at room temperature, using quasi-static initial strain rate and for a limited deformation range. This makes it difficult to discuss volumetric strain results below room temperature. Further SEM testing at lower temperatures and higher initial strain rates is recommended to study the phenomena of change in volumetric strain. SEM testing at the lowest initial temperature and highest initial strain rates might also reveal if the material crazes and whether or not it affects fracture.

8 Bibliography

1. Arruda, E.M., M.C. Boyce, and R. Jayachandran, *Effects of strain rate, temperature and thermomechanical coupling on the finite strain deformation of glassy polymers.* Mechanics of Materials, 1995. **19**(2): p. 193-212.

2. Richeton, J., et al., *Influence of temperature and strain rate on the mechanical behavior of three amorphous polymers: Characterization and modeling of the compressive yield stress.* International Journal of Solids and Structures, 2006. **43**(7–8): p. 2318-2335.

3. Estevez, R., M.G.A. Tijssens, and E. Van der Giessen, *Modeling of the competition between shear yielding and crazing in glassy polymers.* Journal of the Mechanics and Physics of Solids, 2000. **48**(12): p. 2585-2617.

4. Matsushige, K., S. Radcliffe, and E. Baer, *The pressure and temperature effects on brittle-to-ductile transition in PS and PMMA.* Journal of Applied Polymer Science, 1976. **20**(7): p. 1853-1866.

5. Chou, S., K. Robertson, and J. Rainey, *The effect of strain rate and heat developed during deformation on the stress-strain curve of plastics.* Experimental Mechanics, 1973. **13**(10): p. 422-432.

6. Jang, B., D.R. Uhlmann, and J. Vander Sande, *Ductile–brittle transition in polymers.* Journal of applied polymer science, 1984. **29**(11): p. 3409-3420.

7. AG, B. *Borcoat™ EA165E*. 2008 [cited 2016 02.05]; Available from: http://www.borealisgroup.com/en/polyolefins/products/Borcoat/Borcoat-EA165E/.

8. Jones, D.R.H. and M.F. Ashby, *Engineering Materials 2 : An Introduction to Microstructures and Processing*. 2012, Elsevier Science: Oxford.

9. Ehrenstein, G.W., *Polymeric materials : structure, properties, applications*. 2001, Munich: Hanser.

10. Sperling, L.H., *Introduction to Physical Polymer Science*. 4th ed. ed. Introduction to Physical Polymer Science, Fourth Edition. 2005, Hoboken: Wiley.

11. Materialscientist. *Spherulite*. 2010 [cited 2016 20.05]; Available from: https://en.wikipedia.org/wiki/File:Spherulite2.PNG.

12. Debenedetti, P.G. and F.H. Stillinger, *Supercooled liquids and the glass transition.* Nature, 2001. **410**(6825): p. 259-267.

13. Bowden, P. and R. Young, *Deformation mechanisms in crystalline polymers.* Journal of Materials Science, 1974. **9**(12): p. 2034-2051.

14. Galeski, A., *Strength and toughness of crystalline polymer systems.* Progress in Polymer Science, 2003. **28**(12): p. 1643-1699.

15. Wang, Y., et al., *Lamellar Thickness and Stretching Temperature Dependency of Cavitation in Semicrystalline Polymers.* PLoS ONE, 2014. **9**(5): p. e97234.

16. Vincent, P.I., *The necking and cold-drawing of rigid plastics.* Polymer, 1960. **1**: p. 7-19.

17. Séguéla, R., *On the Natural Draw Ratio of Semi-Crystalline Polymers: Review of the Mechanical, Physical and Molecular Aspects.* Macromolecular Materials and Engineering, 2007. **292**(3): p. 235-244.

18. Govaert, L.L.E., P.H.M.P. Timmermans, and W.A.M.M. Brekelmans, *The influence of intrinsic strain softening on strain localization in polycarbonate : modeling and experimental validation.* Journal of Engineering Materials and Technology : Transactions of the ASME, 2000. **122**(2): p. 177-4289.

19. Meijer, H.E.H. and L.E. Govaert, *Mechanical performance of polymer systems: The relation between structure and properties.* Progress in Polymer Science, 2005. **30**(8): p. 915-938.

20. Van Melick, H., L. Govaert, and H. Meijer, *On the origin of strain hardening in glassy polymers.* Polymer, 2003. **44**(8): p. 2493-2502.

21. Kinloch, A.J., *Fracture behaviour of polymers*. 2013: Springer Science & Business Media.

22. Dasari, A. and R.D.K. Misra, *The role of micrometric wollastonite particles on stress whitening behavior of polypropylene composites.* Acta Materialia, 2004. **52**(6): p. 1683-1697.

23. Pawlak, A., A. Galeski, and A. Rozanski, *Cavitation during deformation of semicrystalline polymers.* Progress in Polymer Science, 2014. **39**(5): p. 921-958.

24. Pawlak, A. and A. Galeski, *Plastic deformation of crystalline polymers: the role of cavitation and crystal plasticity.* Macromolecules, 2005. **38**(23): p. 9688-9697.

25. Siviour, C., et al. *Mechanical behaviour of polymers at high rates of strain*. in *Journal de Physique IV (Proceedings)*. 2006. EDP sciences.

26. Liu, Y. and R.W. Truss, *A study of tensile yielding of isotactic polypropylene.* Journal of Polymer Science Part B: Polymer Physics, 1994. **32**(12): p. 2037-2047.

27. SIMLab, *Theory Manual: SIMLab Polymers Model*. 2013: NTNU.

28. Caddell, R.M., R.S. Raghava, and A.G. Atkins, *Pressure dependent yield criteria for polymers.* Materials Science and Engineering, 1974. **13**(2): p. 113-120.

29. Johnson, G.R. and W.H. Cook. *A constitutive model and data for metals subjected to large strains, high strain rates and high temperatures*. in *Proceedings of the 7th International Symposium on Ballistics*. 1983. The Hague, The Netherlands.

30. Banerjee, B., *An evaluation of plastic flow stress models for the simulation of high-temperature and high-strain-rate deformation of metals.* arXiv preprint cond-mat/0512466, 2005.

31. Voce, E., *A practical strain-hardening function.* Metallurgia, 1955. **51**(307): p. 219-226.

32. Rittel, D., *On the conversion of plastic work to heat during high strain rate deformation of glassy polymers.* Mechanics of Materials, 1999. **31**(2): p. 131-139.

33. INSTRON. *5940 Series Single Column Table Top Systems for Low-Force Mechanical Testing*. 2016; Available from: http://www.instron.us/en-us/products/testing-systems/universal-testing-systems/electromechanical/5900/5940-single-column.

34. Fagerholt, E., *Field measurements in mechanical testing using close-range photogrammetry and digital image analysis.* 2012.

35. Naqui, S.I. and I.M. Robinson, *Tensile dilatometric studies of deformation in polymeric materials and their composites.* Journal of Materials Science, 1993. **28**(6): p. 1421-1429.

36. Parker, W.J., et al., *Flash Method of Determining Thermal Diffusivity, Heat Capacity, and Thermal Conductivity.* Journal of Applied Physics, 1961. **32**(9): p. 1679-1684.

37. Simulia, D.S., *Abaqus 6.12 documentation.* 2012.

9 Appendix

A Uniaxial tension tests

A.1 Benchmark curves

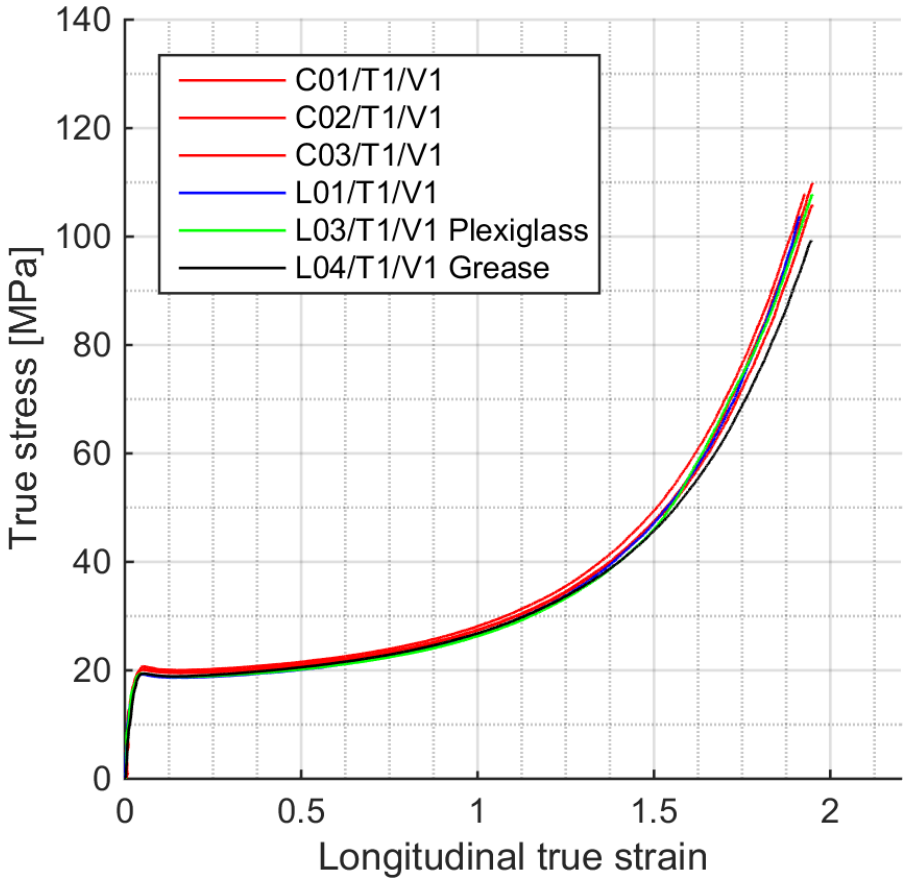

A.2 Stress curves - Categorized by initial strain rate

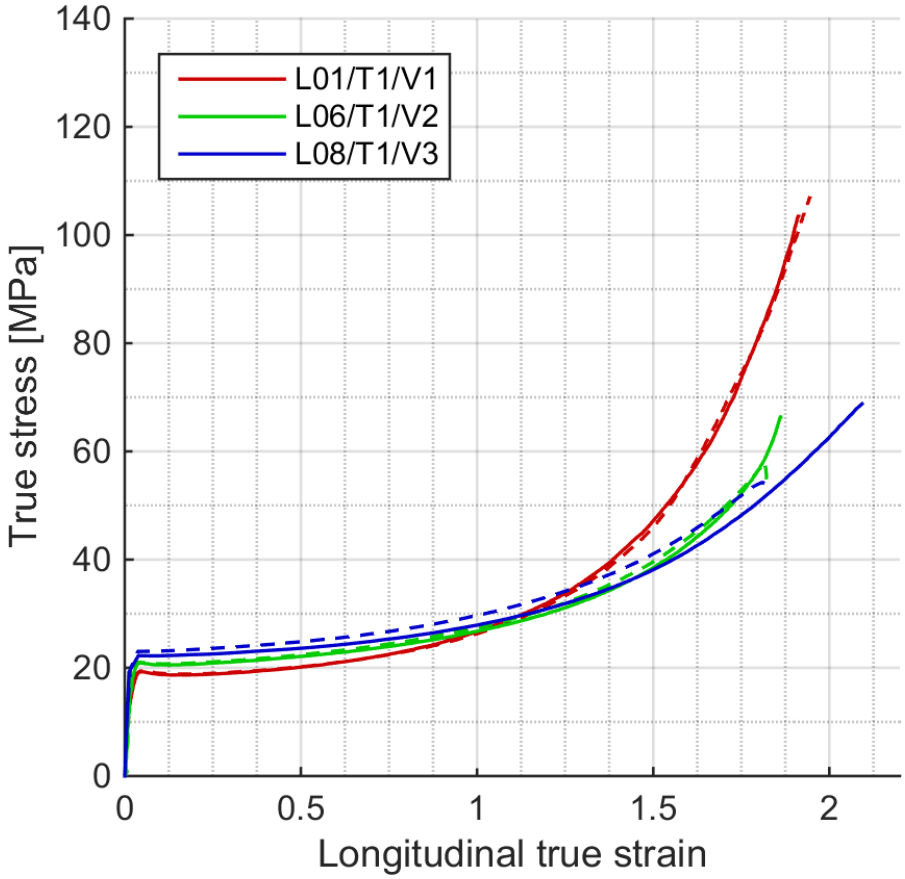

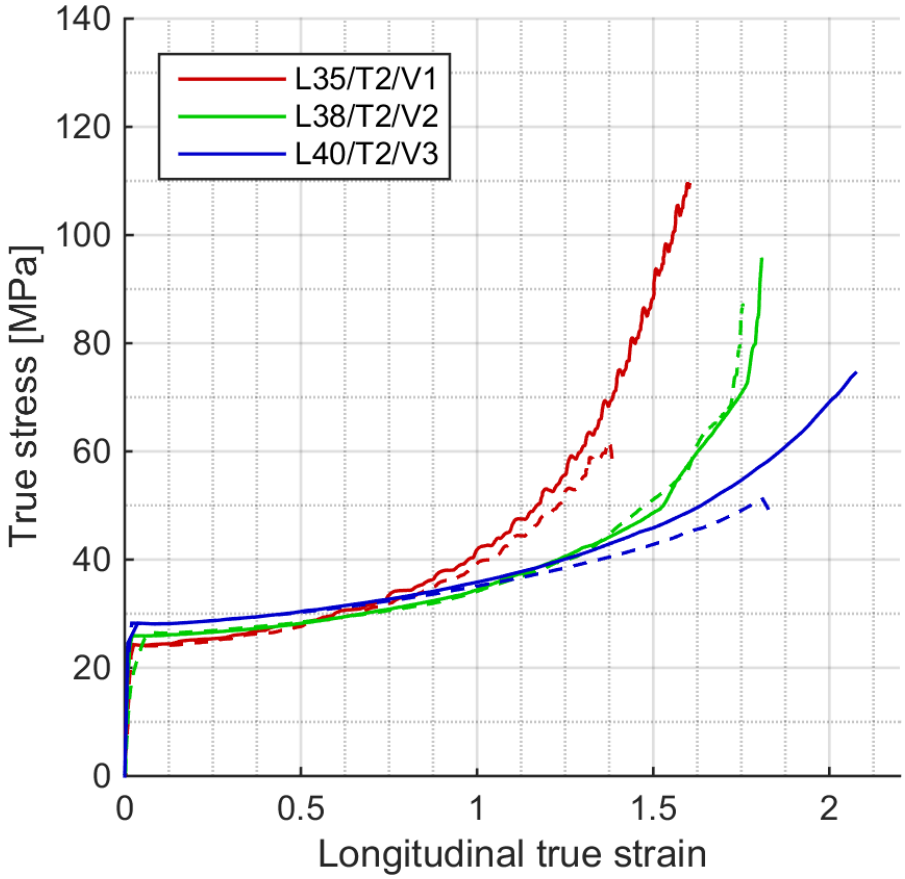

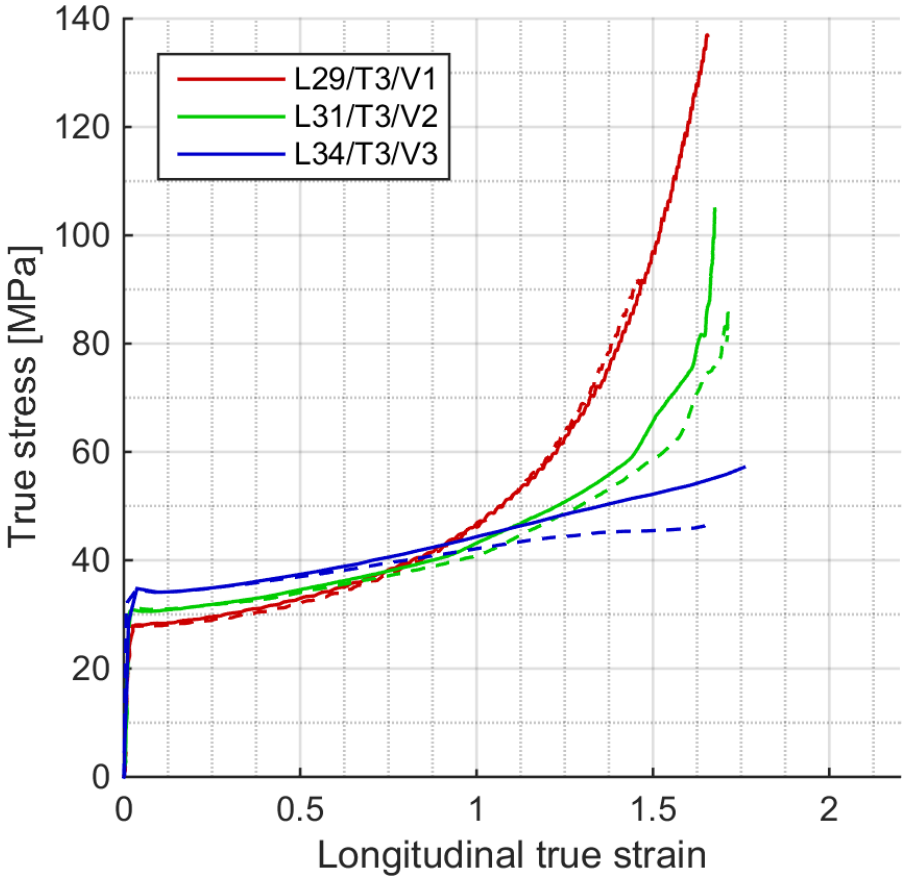
L29/T3/V1
L31/T3/V2
L34/T3/V3
True stress [MPa]
Longitudinal true strain
0
20
40
60
80
100
120
140
0
0.5
1
1.5
2

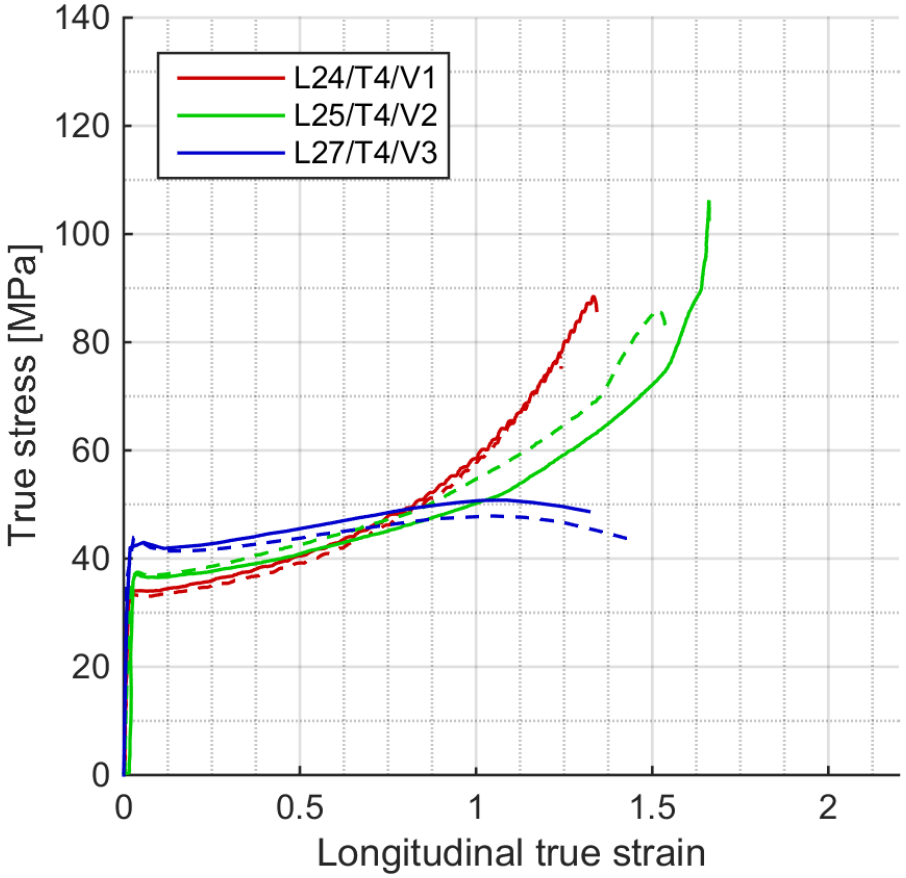
L24/T4/V1
L25/T4/V2
L27/T4/V3
True stress [MPa]
Longitudinal true strain
0
20
40
60
80
100
120
140
0
0.5
1
1.5
2

A.3 Stress curves – Categorized by initial temperature

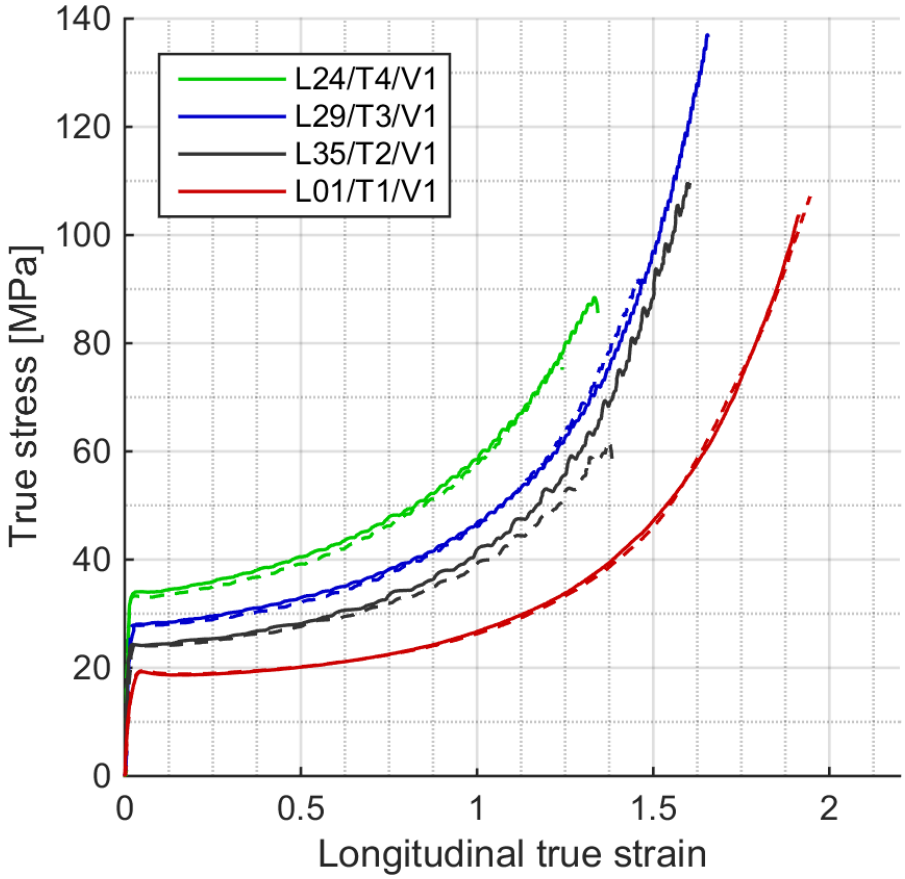

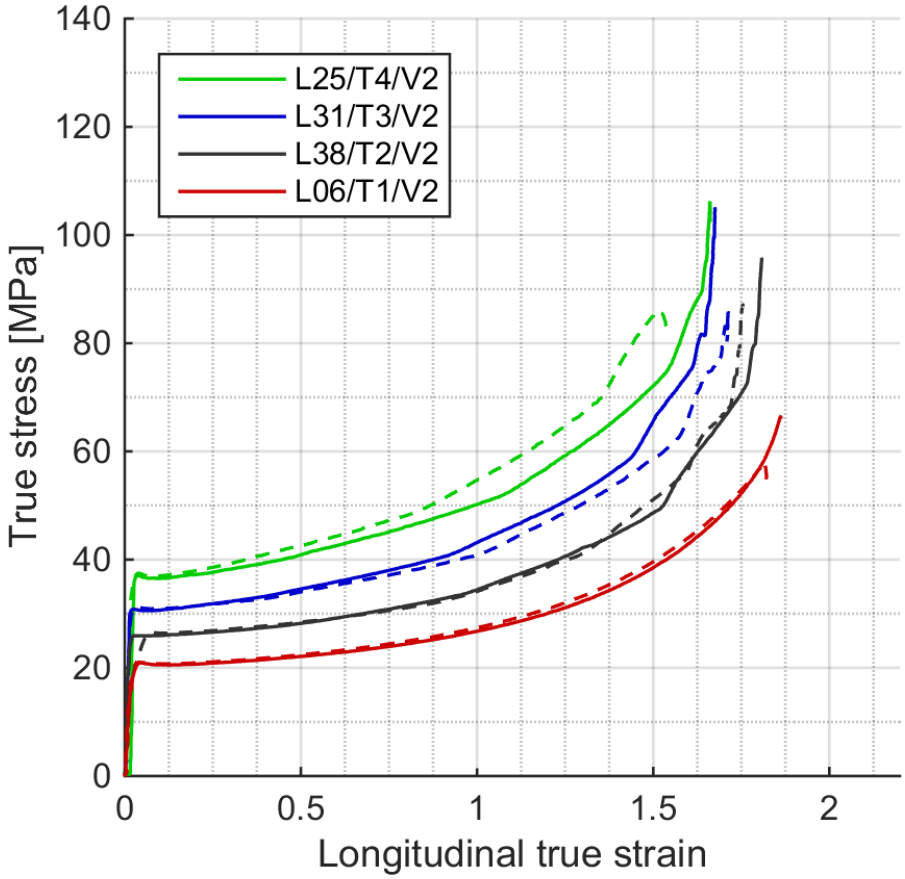

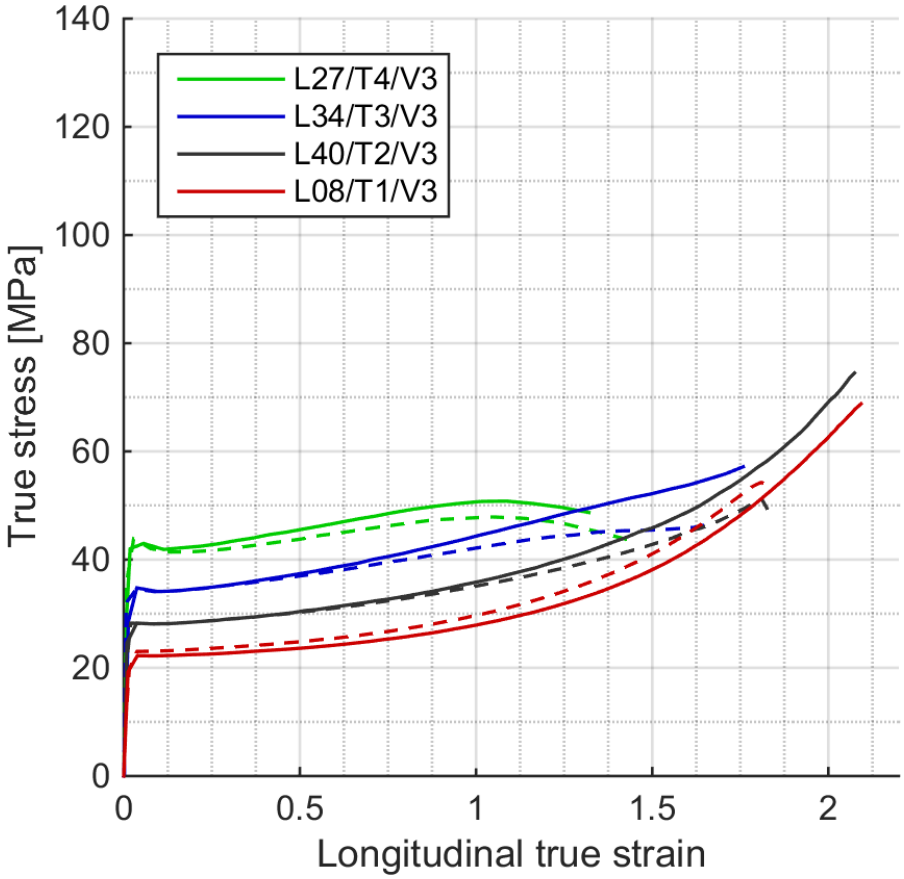

A.4 Yield stress, Young's modulus and rate sensitivity

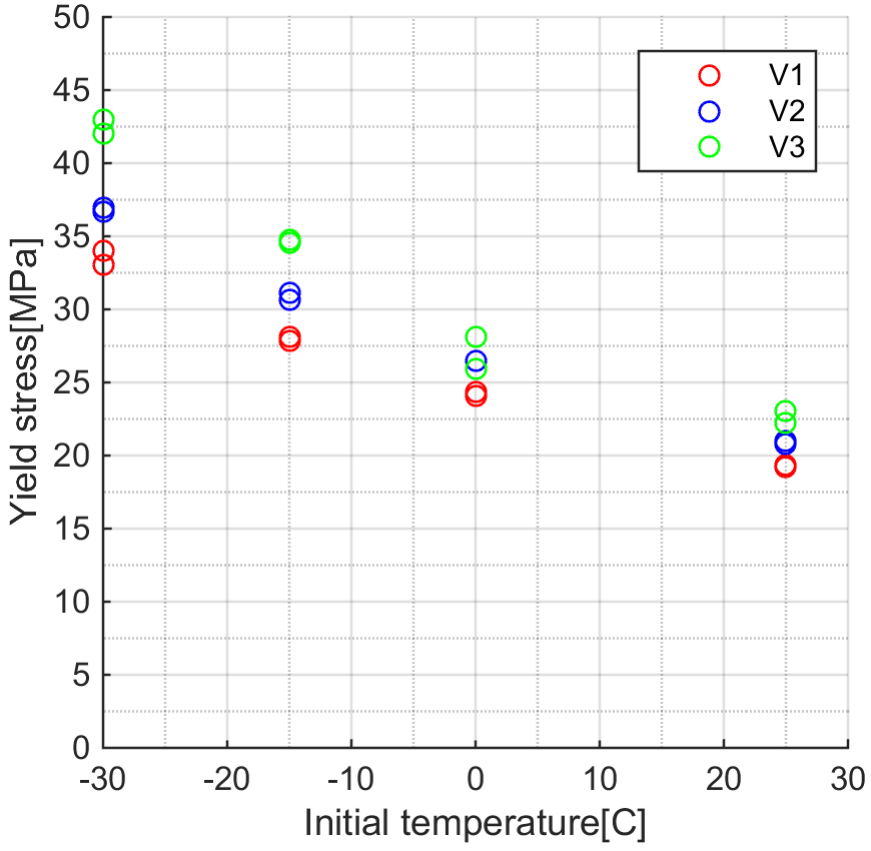

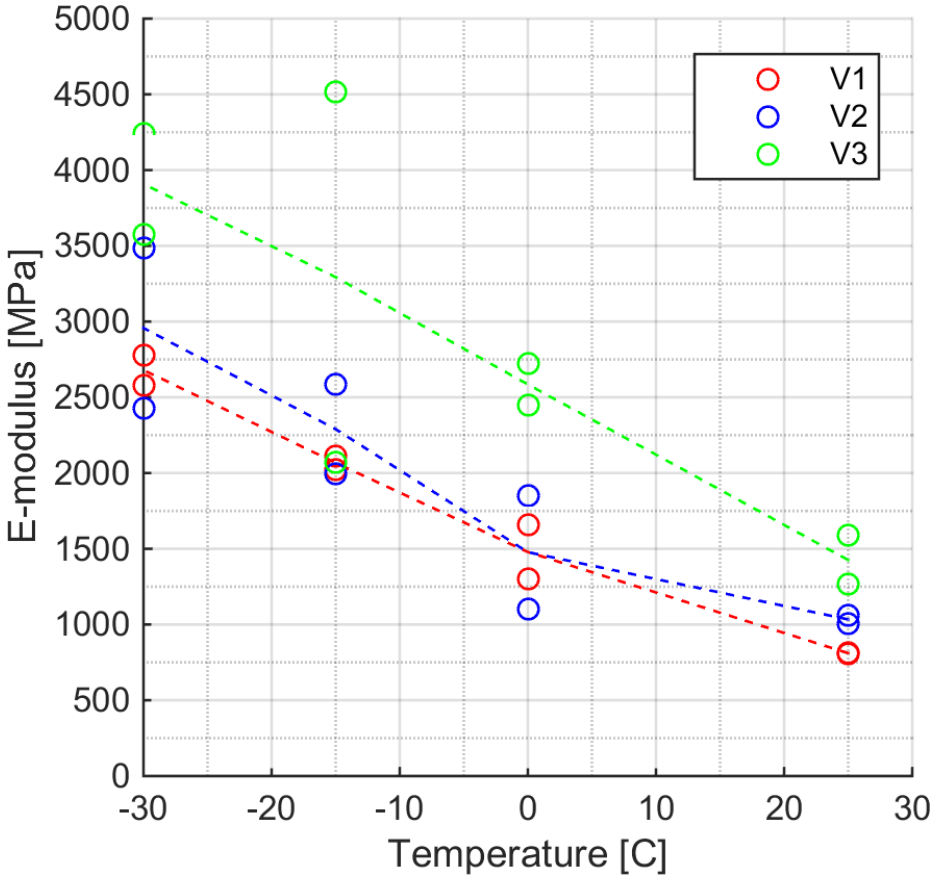
V1
V2
V3
E-modulus [MPa]
Temperature [C]
5000
4500
4000
3500
3000
2500
2000
1500
1000
500
0
-30
-20
-10
0
10
20
30

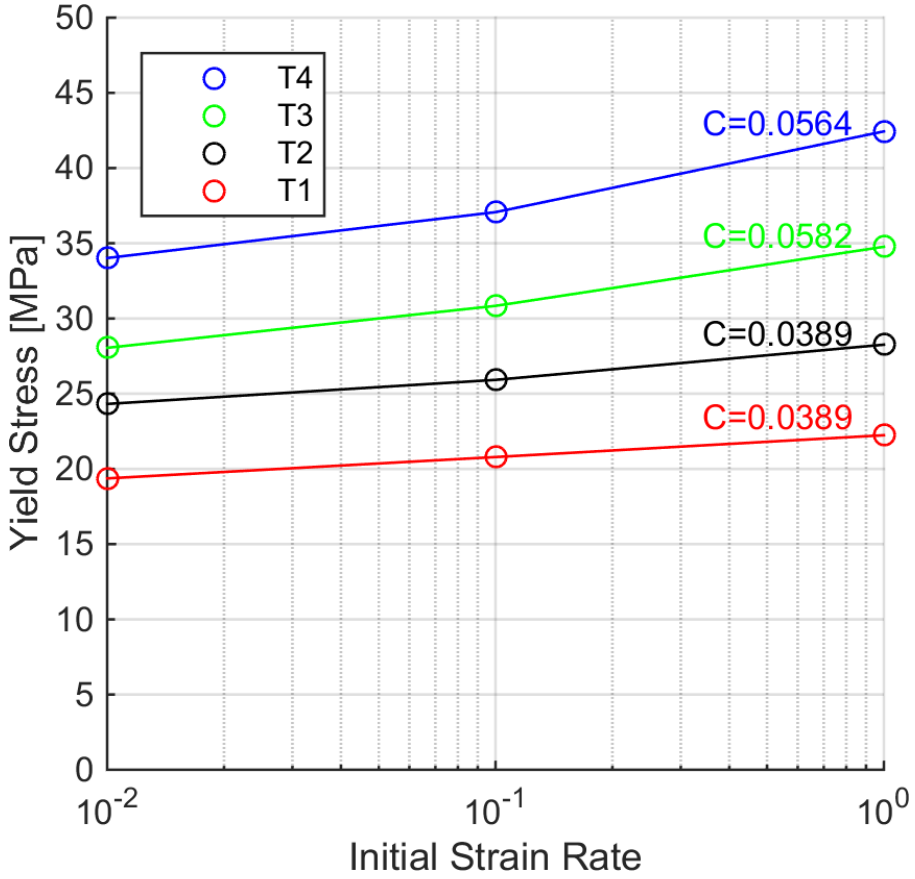
T4
T3
T2
T1
C=0.0564
C=0.0582
C=0.0389
C=0.0389
Yield Stress [MPa]
Initial Strain Rate
50
45
40
35
30
25
20
15
10
5
0
10-2
10-1
100

A.5 Strain curves – Camera specific strain, categorized by temperature

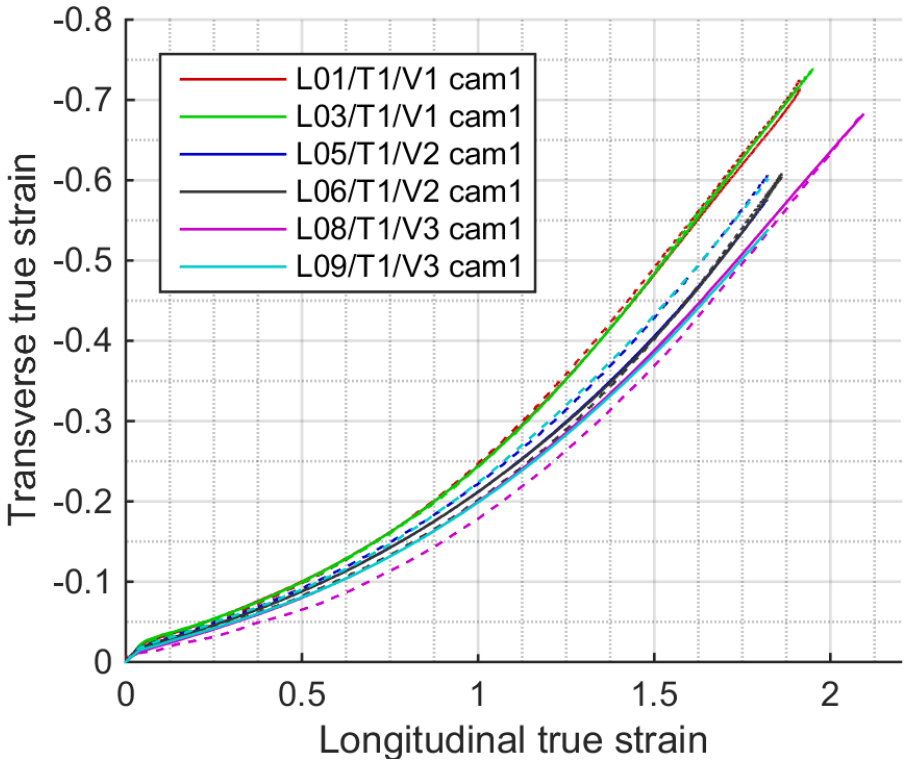

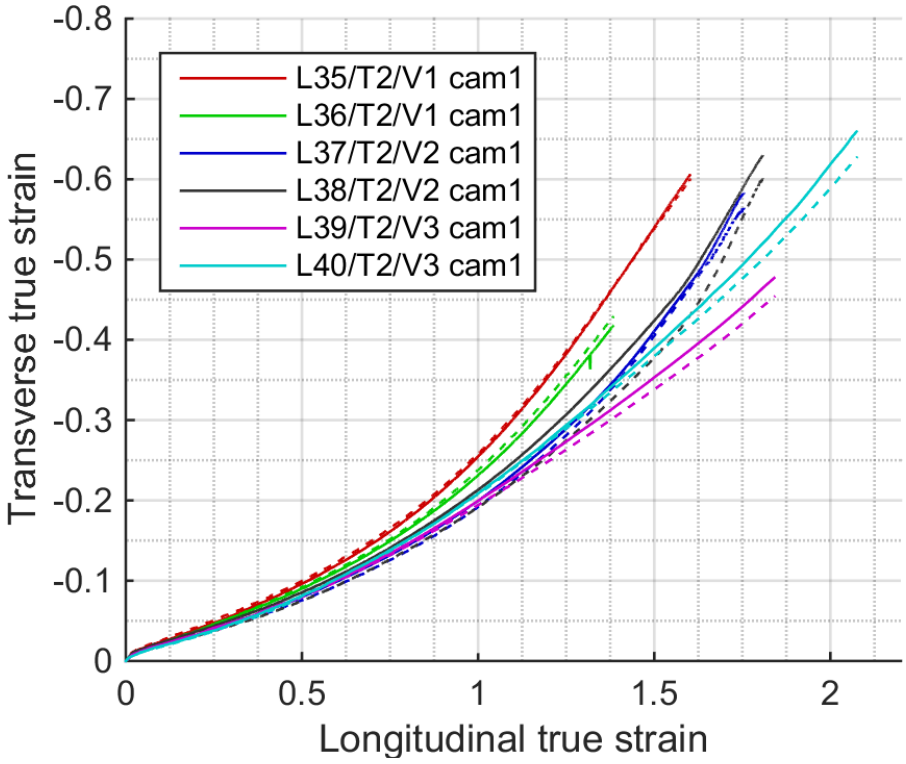

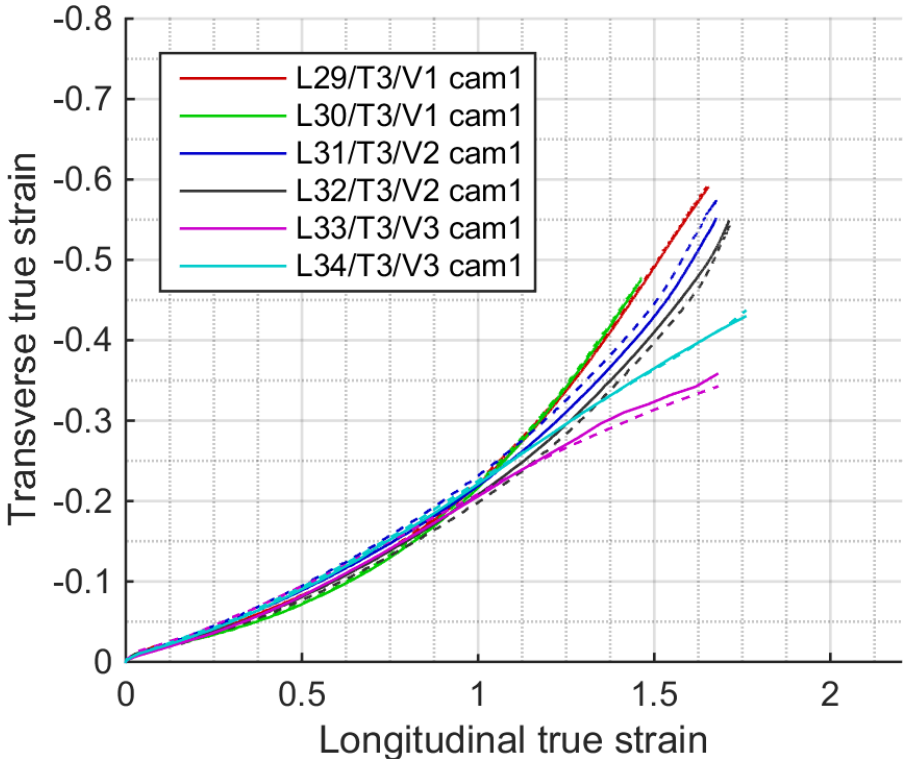
L29/T3/V1 cam1
L30/T3/V1 cam1
L31/T3/V2 cam1
L32/T3/V2 cam1
L33/T3/V3 cam1
L34/T3/V3 cam1
Transverse true strain
Longitudinal true strain
-0.8
-0.7
-0.6
-0.5
-0.4
-0.3
-0.2
-0.1
0
0
0.5
1
1.5
2

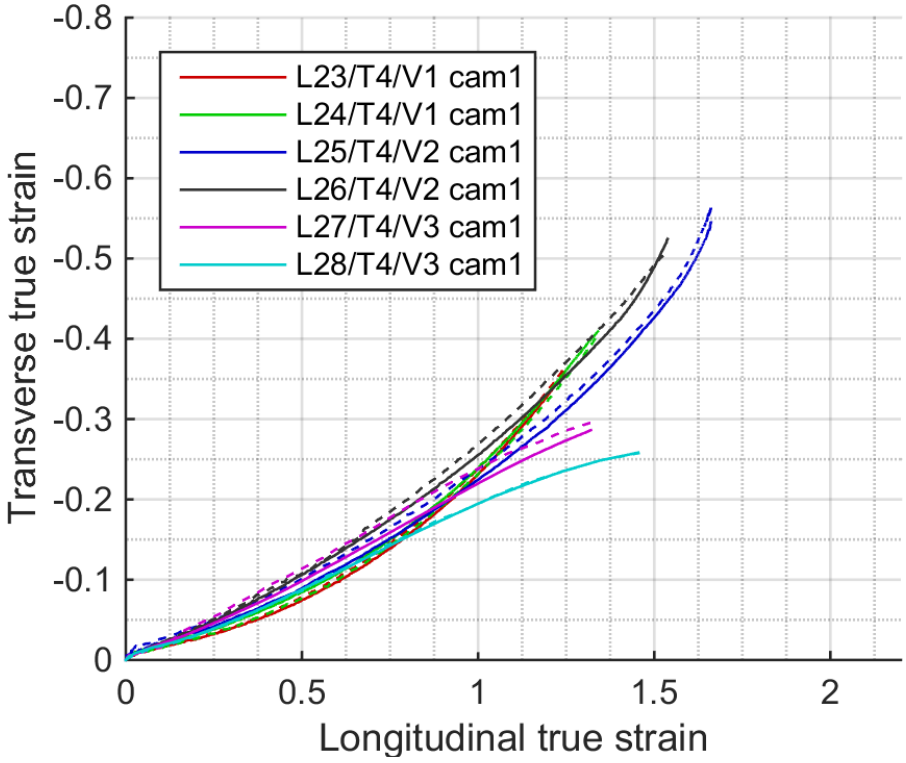
L23/T4/V1 cam1
L24/T4/V1 cam1
L25/T4/V2 cam1
L26/T4/V2 cam1
L27/T4/V3 cam1
L28/T4/V3 cam1
Transverse true strain
Longitudinal true strain
-0.8
-0.7
-0.6
-0.5
-0.4
-0.3
-0.2
-0.1
0
0
0.5
1
1.5
2

A.6 Strain curves – Volumetric strains

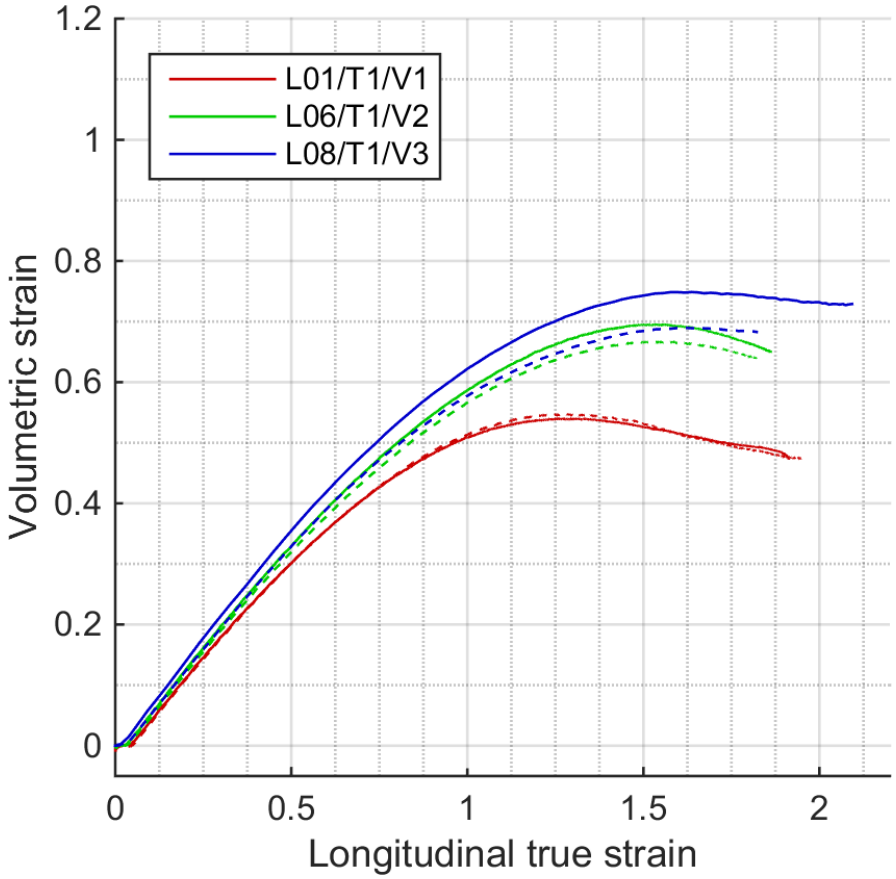

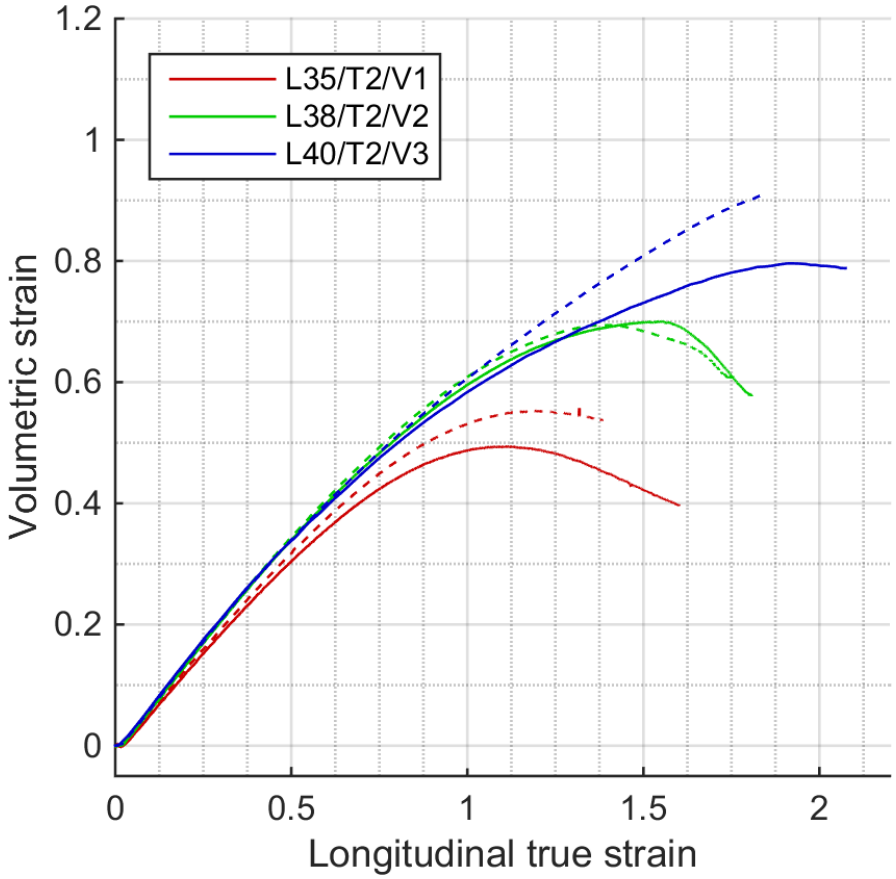

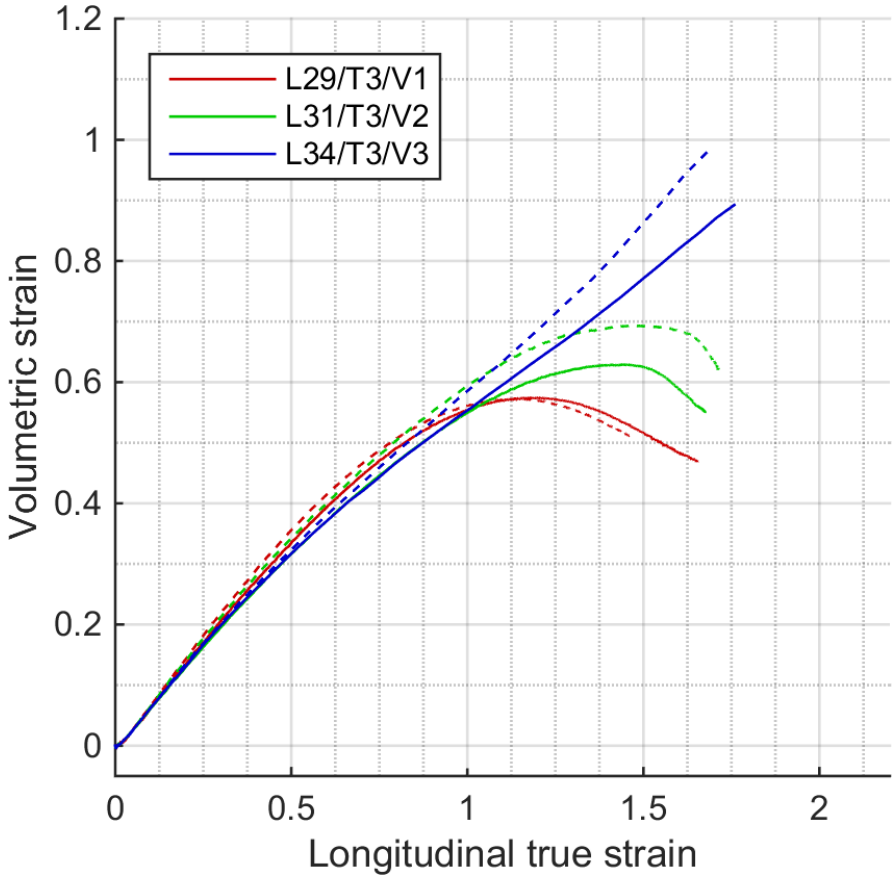
L29/T3/V1
L31/T3/V2
L34/T3/V3
Volumetric strain
Longitudinal true strain
0
0.2
0.4
0.6
0.8
1
1.2
0.5
1.5
2

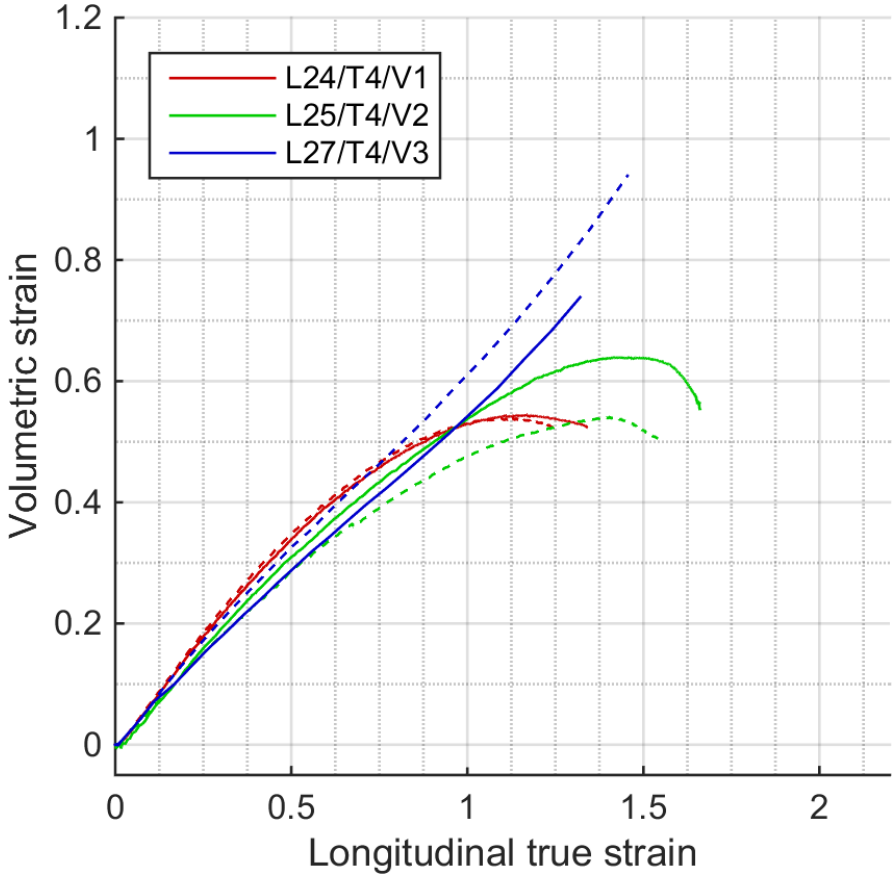
L24/T4/V1
L25/T4/V2
L27/T4/V3
Volumetric strain
Longitudinal true strain
0
0.2
0.4
0.6
0.8
1
1.2
0.5
1.5
2

A.7 Contraction ratio curves

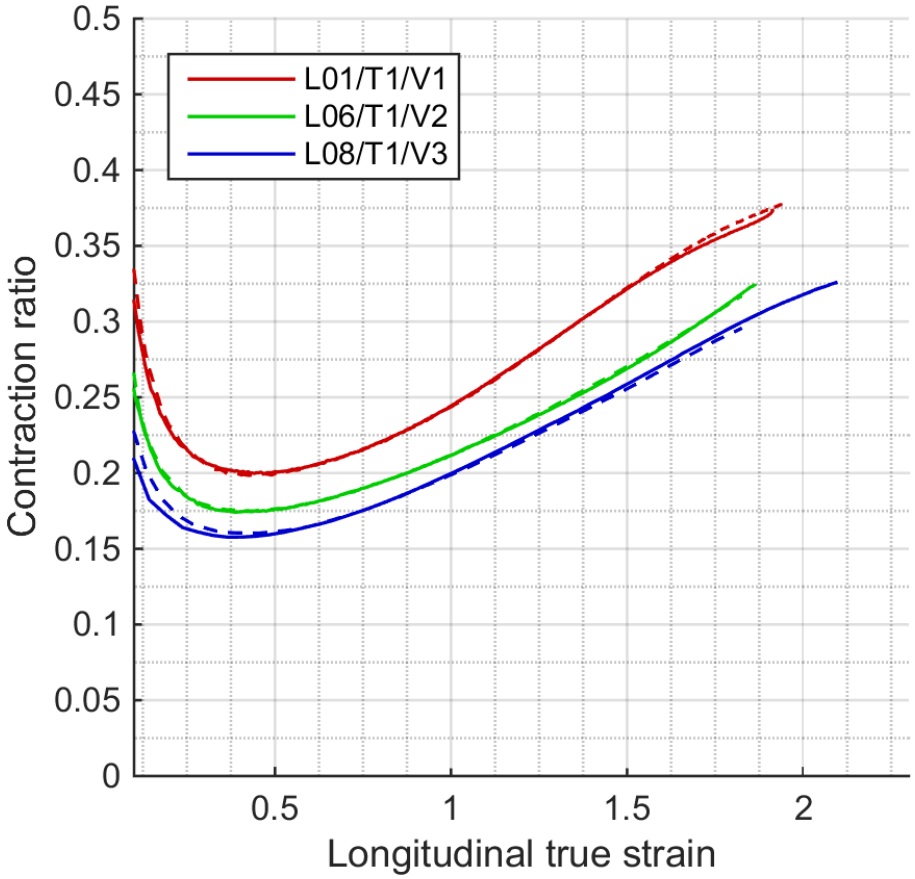

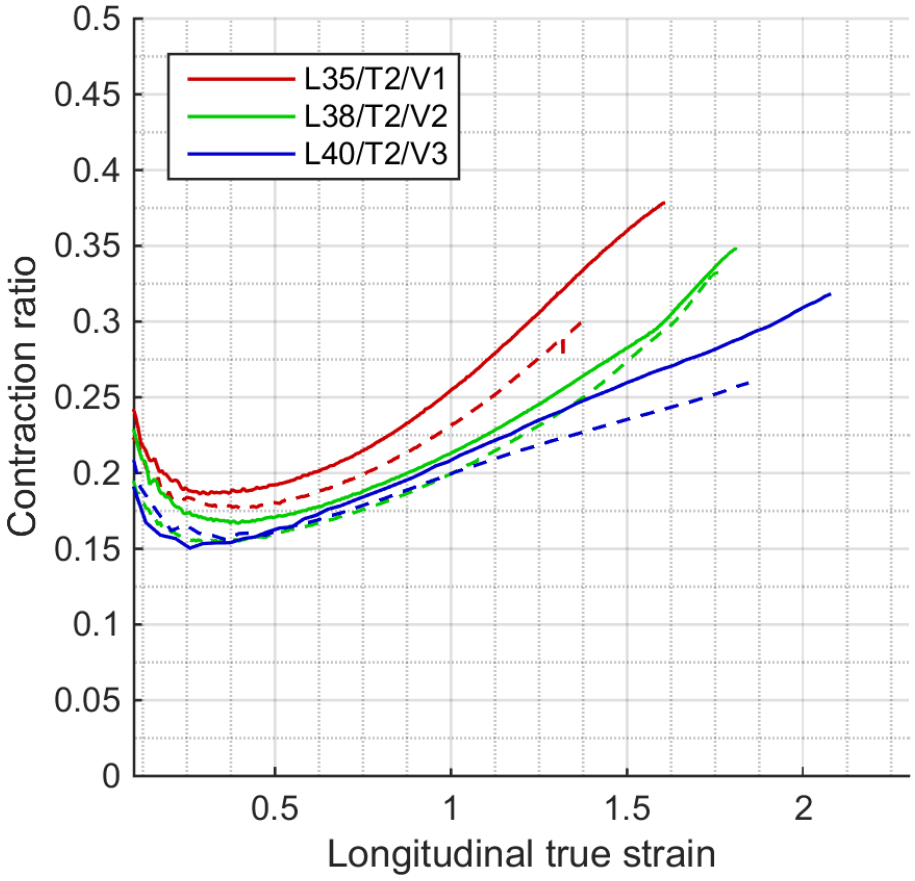

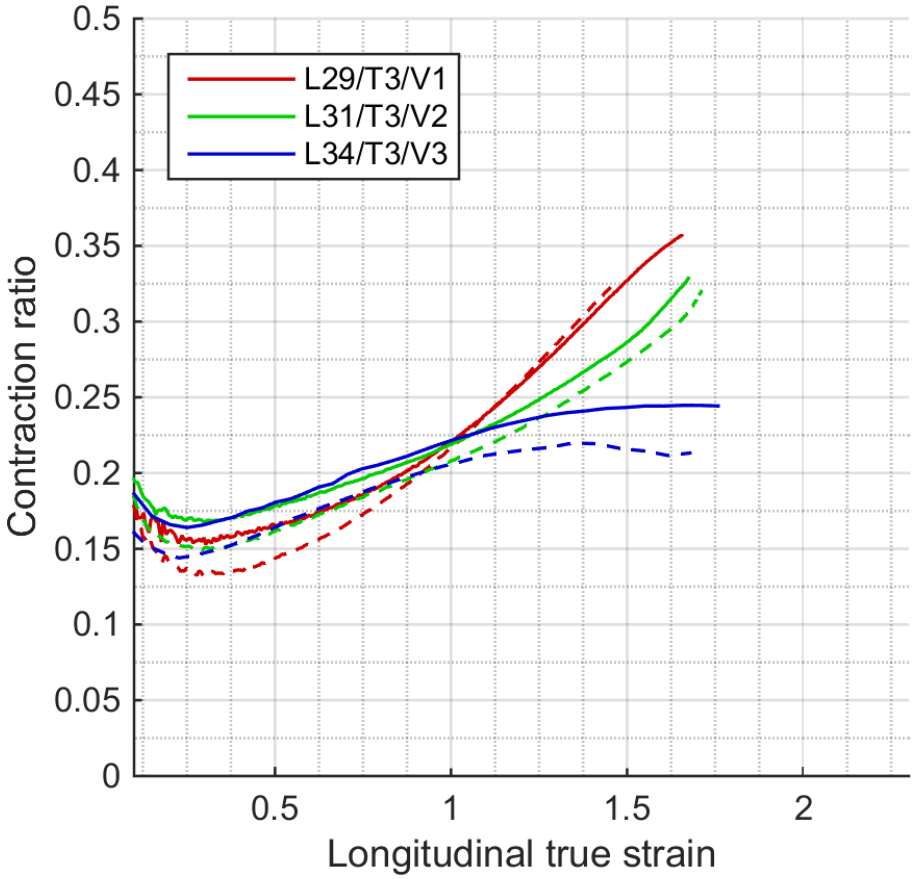
L29/T3/V1
L31/T3/V2
L34/T3/V3
Contraction ratio
Longitudinal true strain
0.5
0.45
0.4
0.35
0.3
0.25
0.2
0.15
0.1
0.05
0
0.5
1
1.5
2

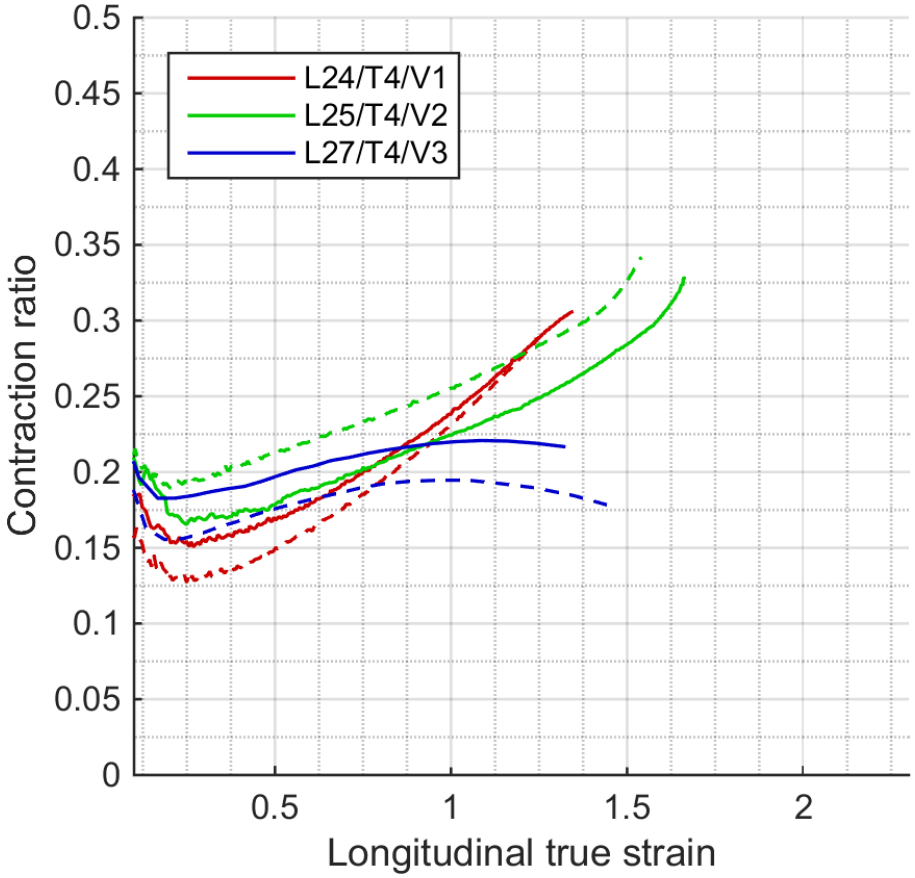
L24/T4/V1
L25/T4/V2
L27/T4/V3
Contraction ratio
Longitudinal true strain
0.5
0.45
0.4
0.35
0.3
0.25
0.2
0.15
0.1
0.05
0
0.5
1
1.5
2

B Compression tests curves

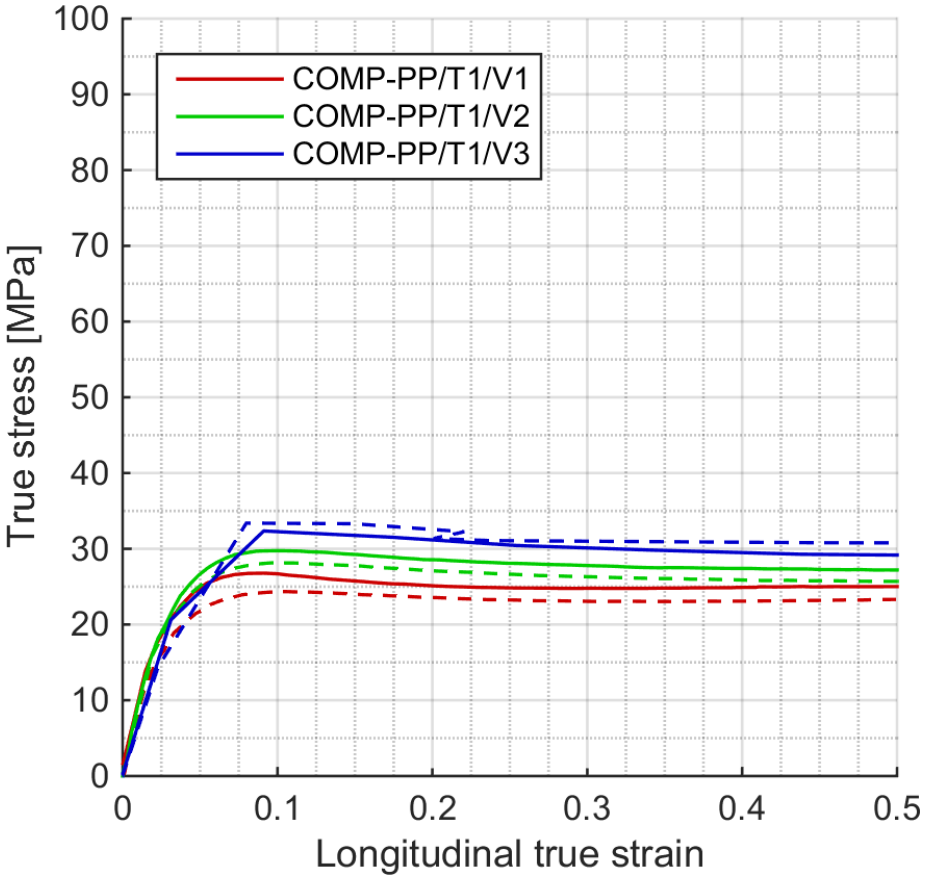

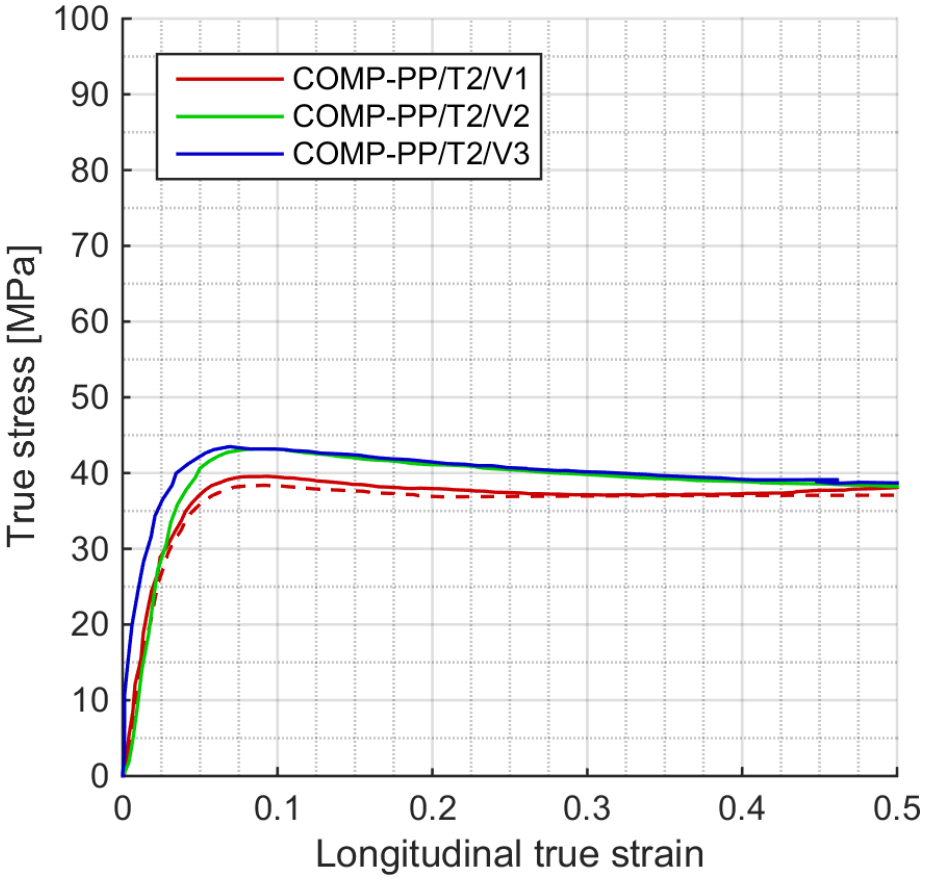

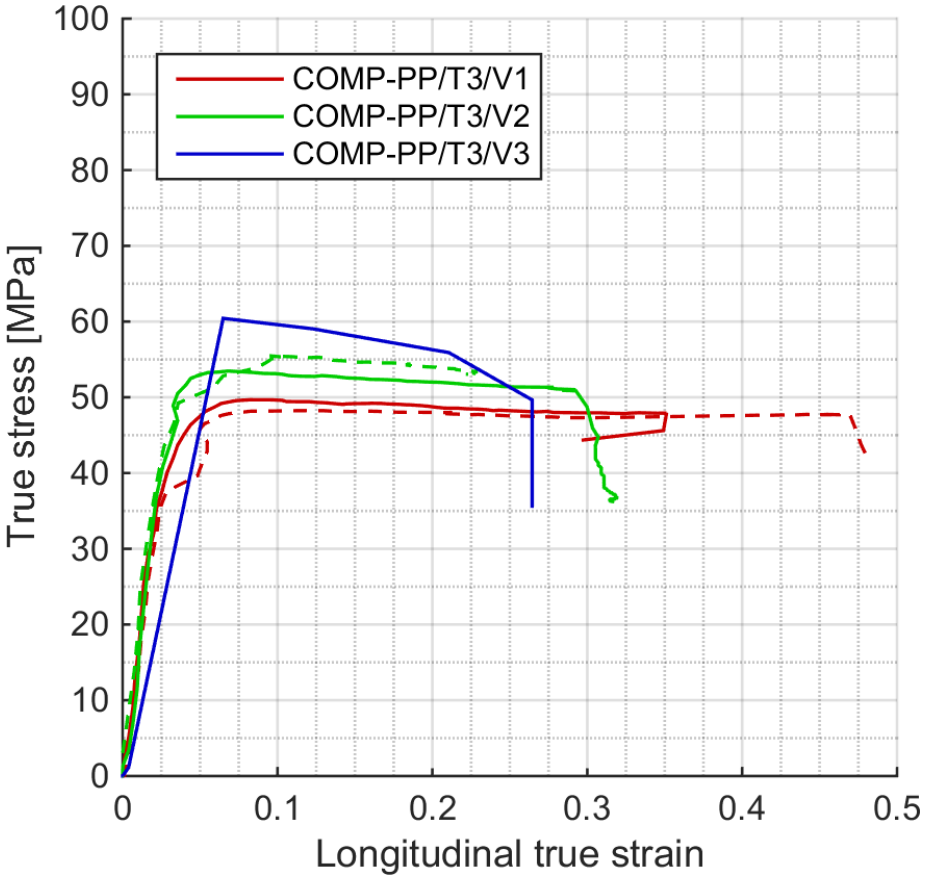
COMP-PP/T3/V1
COMP-PP/T3/V2
COMP-PP/T3/V3
True stress [MPa]
Longitudinal true strain
0
10
20
30
40
50
60
70
80
90
100
0
0.1
0.2
0.3
0.4
0.5

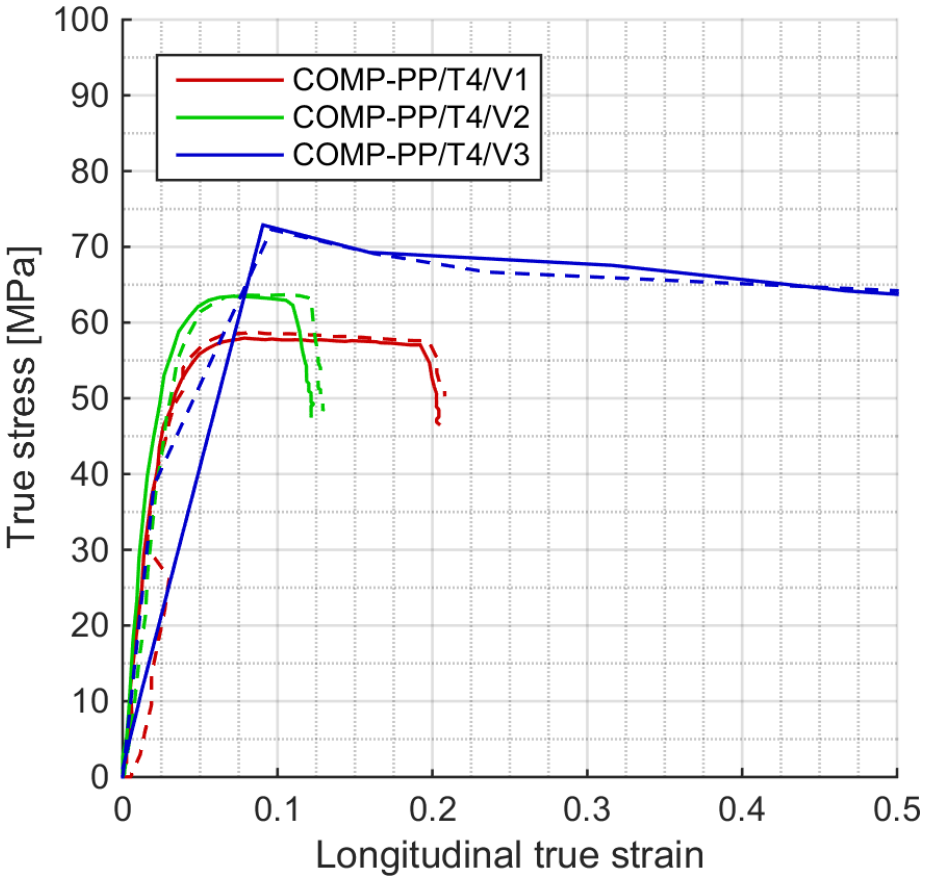
COMP-PP/T4/V1
COMP-PP/T4/V2
COMP-PP/T4/V3
True stress [MPa]
Longitudinal true strain
0
10
20
30
40
50
60
70
80
90
100
0
0.1
0.2
0.3
0.4
0.5

C Comparison of material testing and simulations

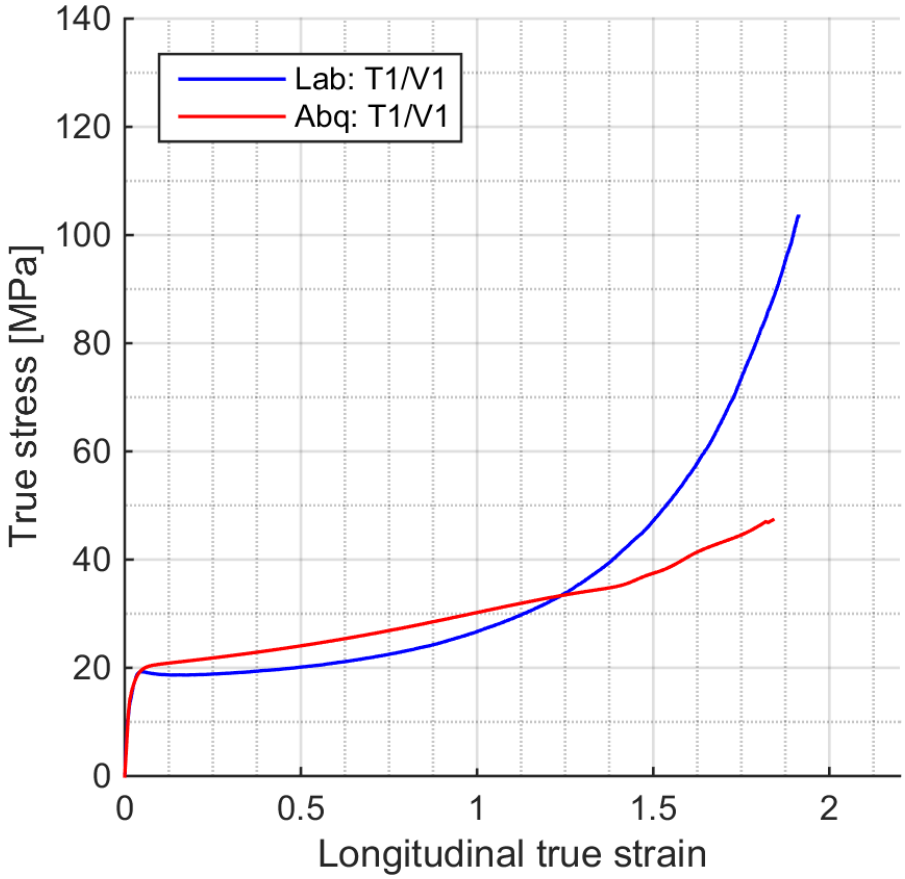

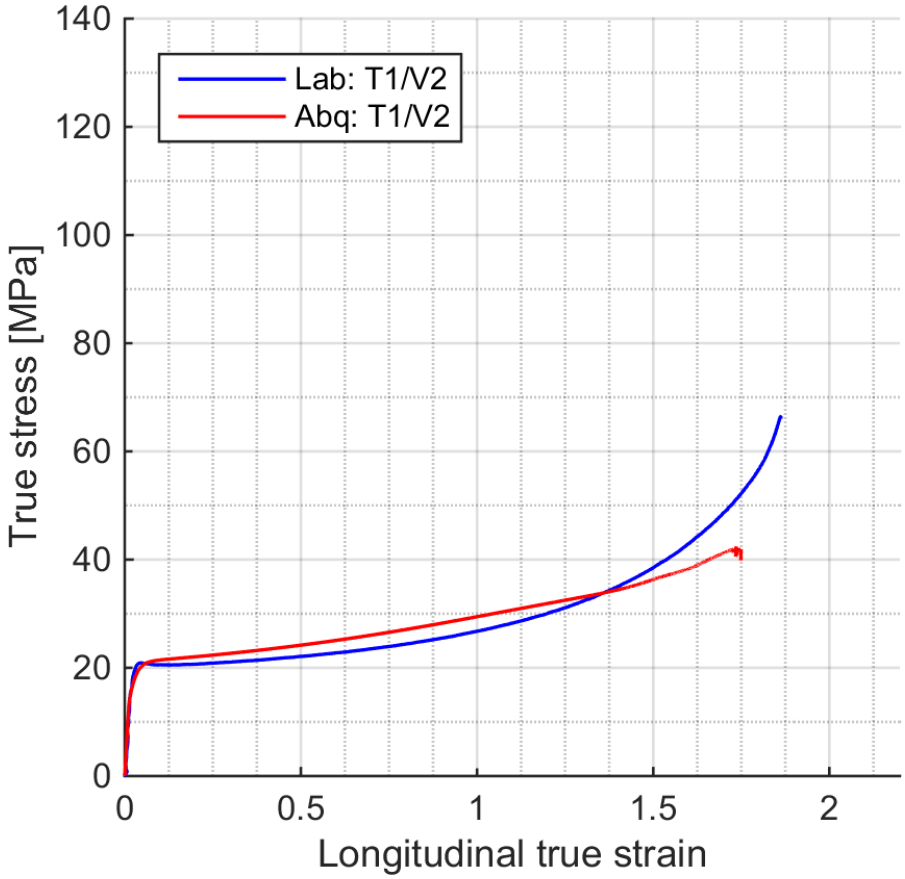

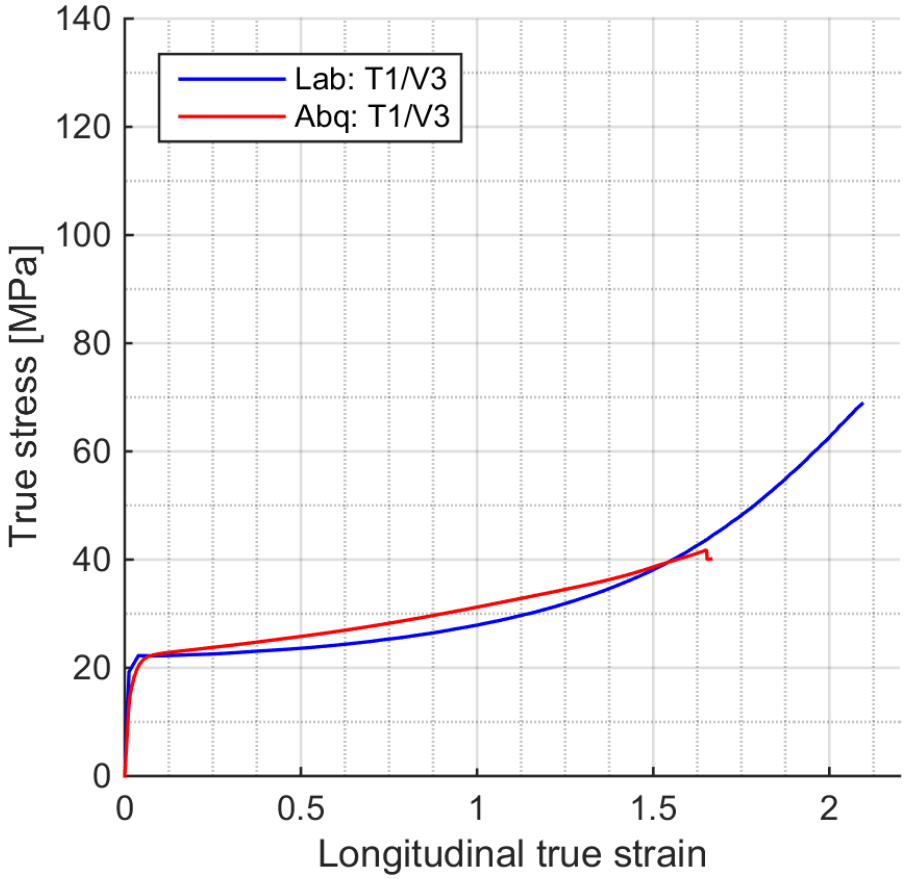
Lab: T1/V3
Abq: T1/V3
True stress [MPa]
Longitudinal true strain
0
20
40
60
80
100
120
140
0
0.5
1
1.5
2

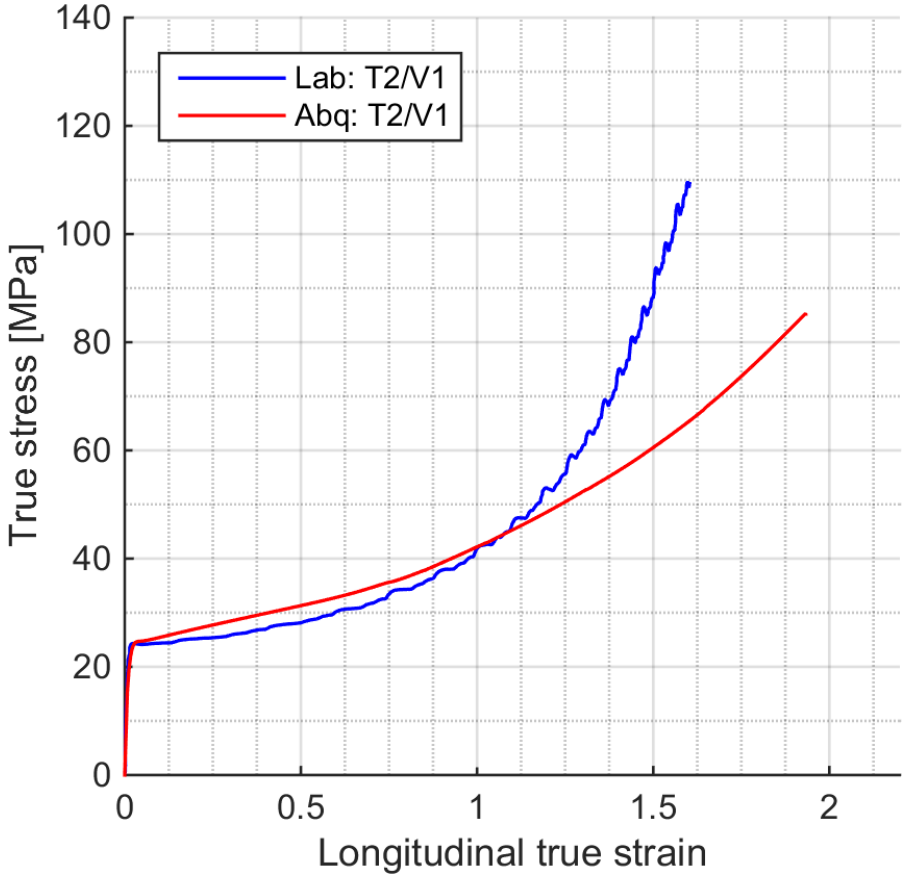
Lab: T2/V1
Abq: T2/V1
True stress [MPa]
Longitudinal true strain
0
20
40
60
80
100
120
140
0
0.5
1
1.5
2

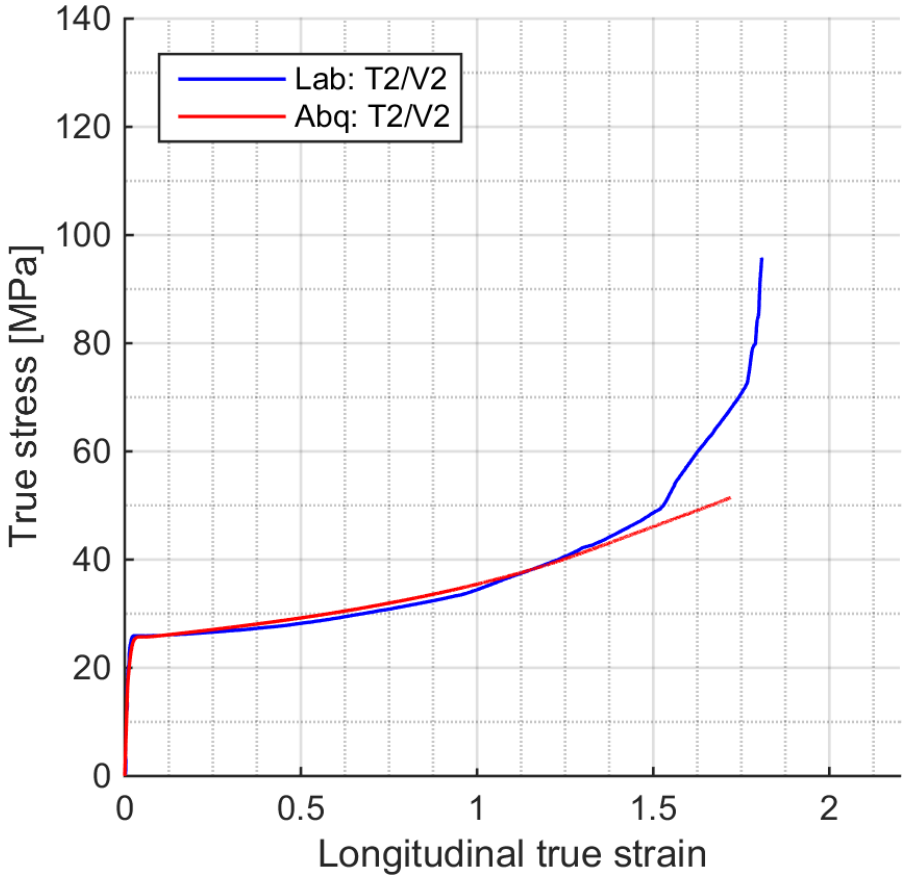
Lab: T2/V2
Abq: T2/V2
True stress [MPa]
Longitudinal true strain
0
20
40
60
80
100
120
140
0
0.5
1
1.5
2

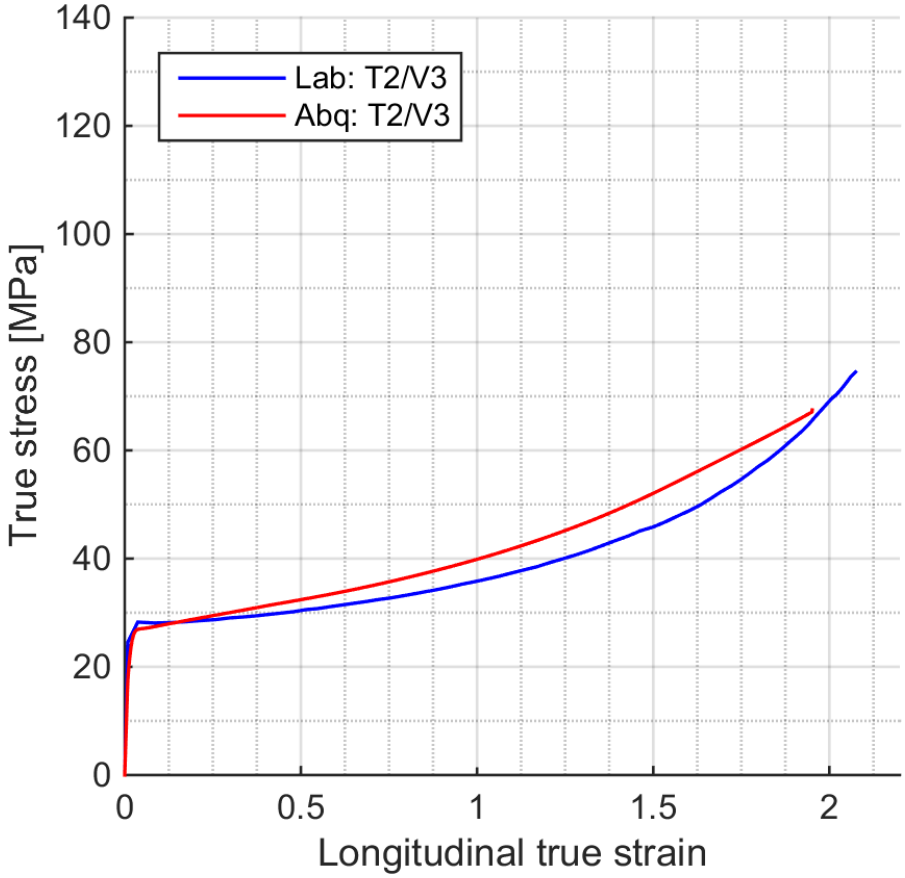
Lab: T2/V3
Abq: T2/V3
True stress [MPa]
Longitudinal true strain
0
20
40
60
80
100
120
140
0
0.5
1
1.5
2

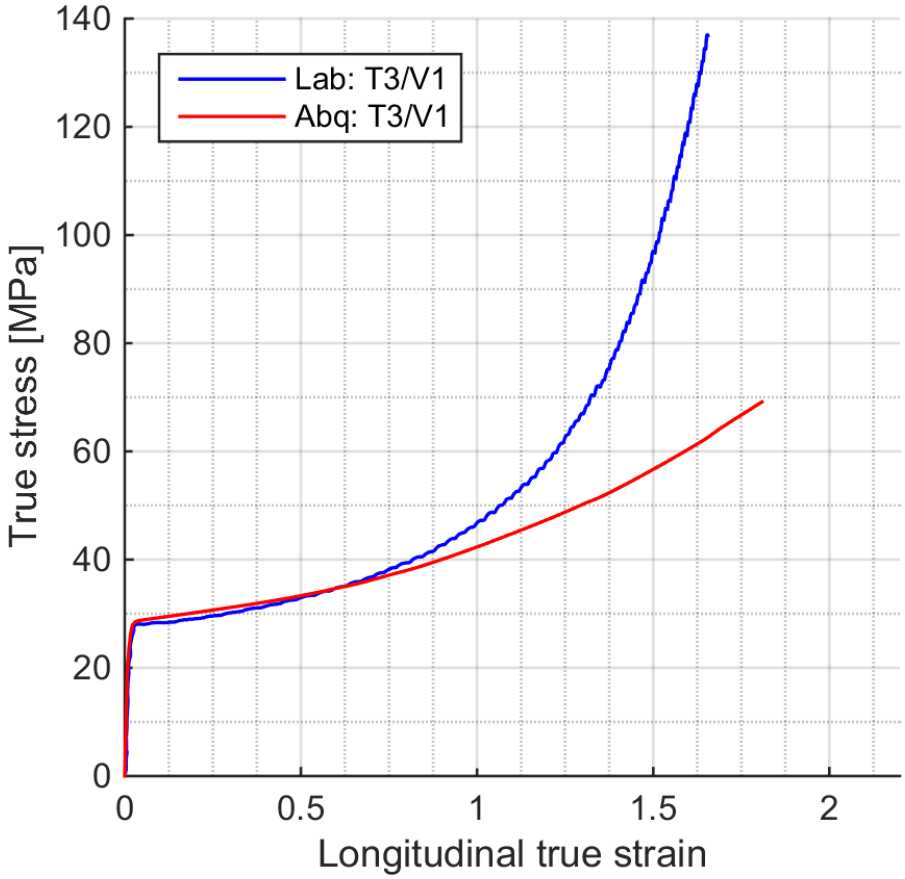
Lab: T3/V1
Abq: T3/V1
True stress [MPa]
Longitudinal true strain
0
20
40
60
80
100
120
140
0
0.5
1
1.5
2

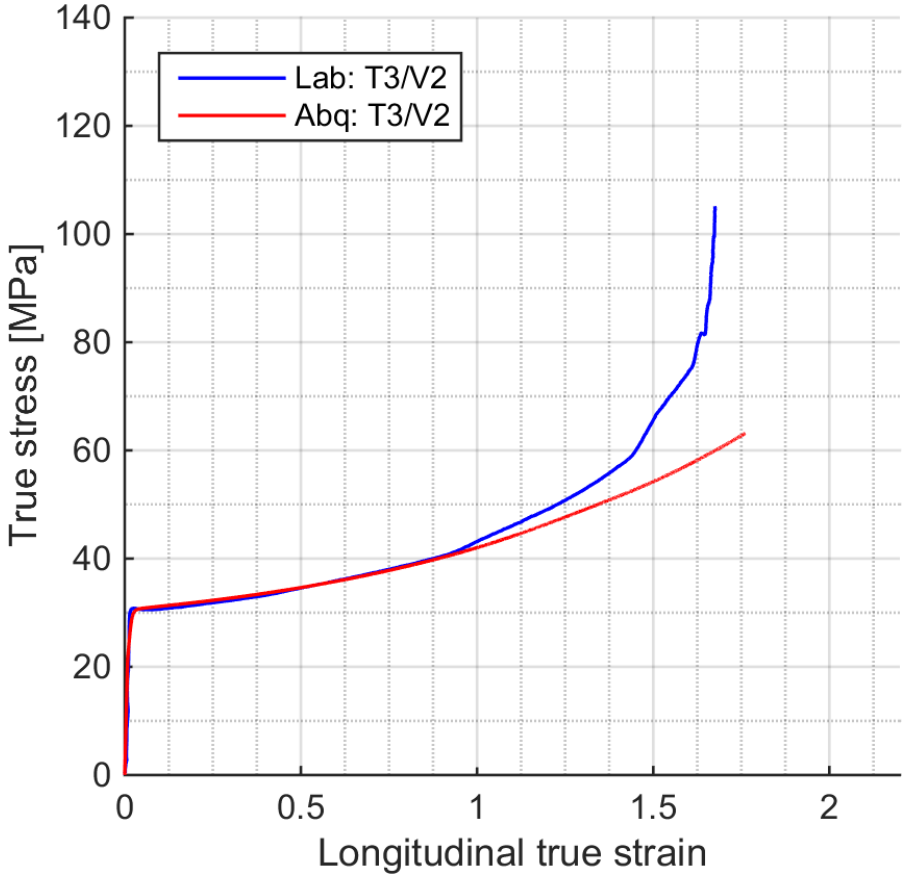
Lab: T3/V2
Abq: T3/V2
True stress [MPa]
Longitudinal true strain
0
20
40
60
80
100
120
140
0
0.5
1
1.5
2

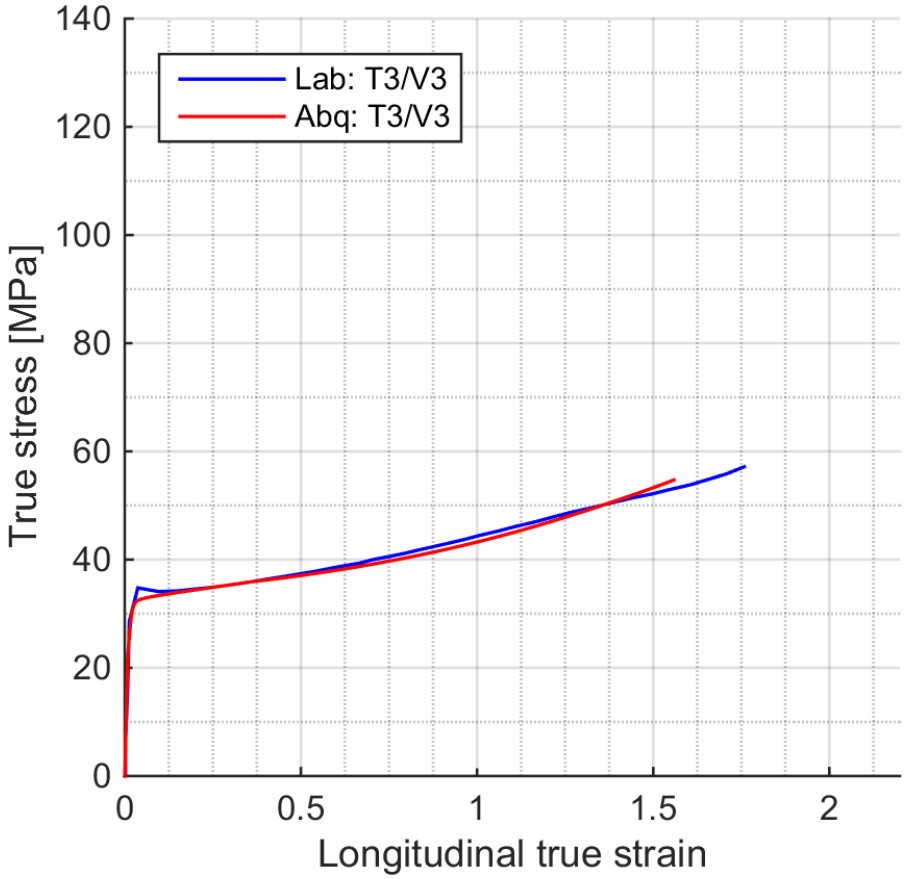
Lab: T3/V3
Abq: T3/V3
True stress [MPa]
Longitudinal true strain
0
20
40
60
80
100
120
140
0
0.5
1
1.5
2

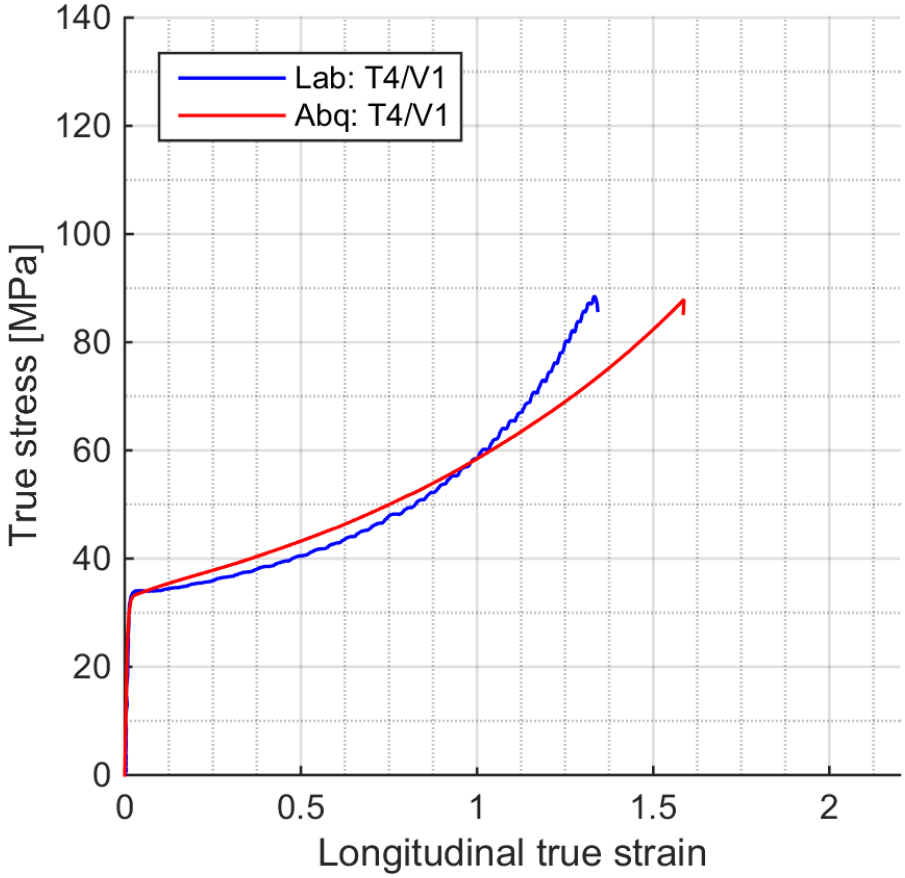
Lab: T4/V1
Abq: T4/V1
True stress [MPa]
Longitudinal true strain
0
20
40
60
80
100
120
140
0
0.5
1
1.5
2

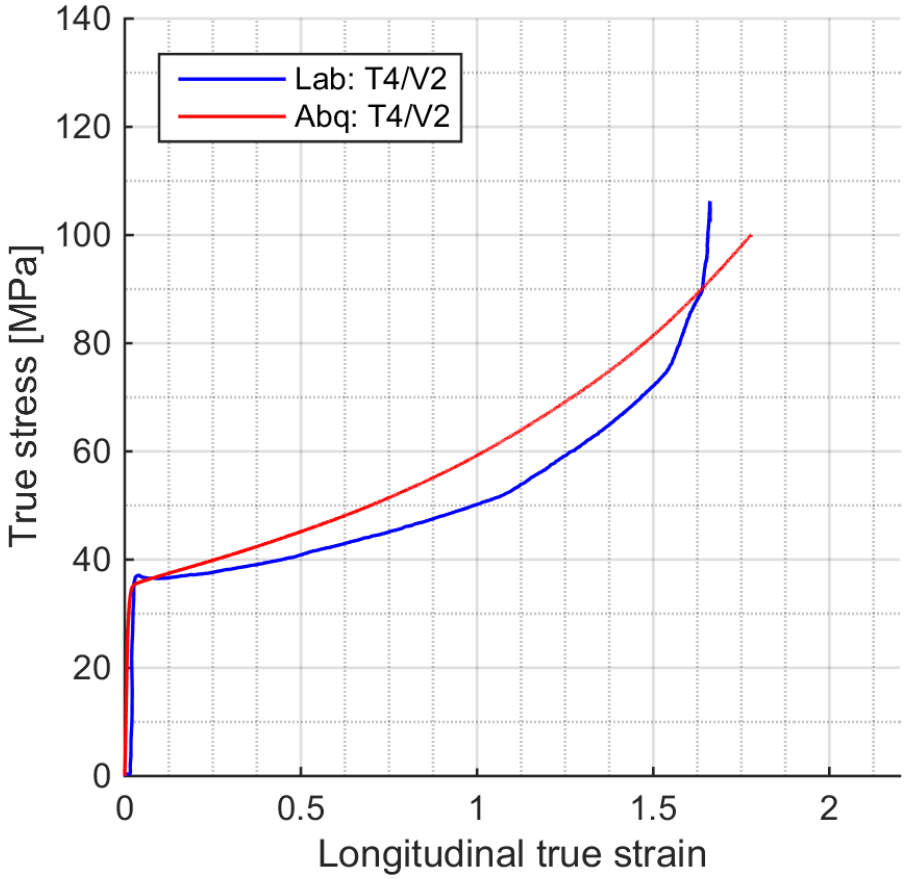
Lab: T4/V2
Abq: T4/V2
True stress [MPa]
Longitudinal true strain
0
20
40
60
80
100
120
140
0
0.5
1
1.5
2

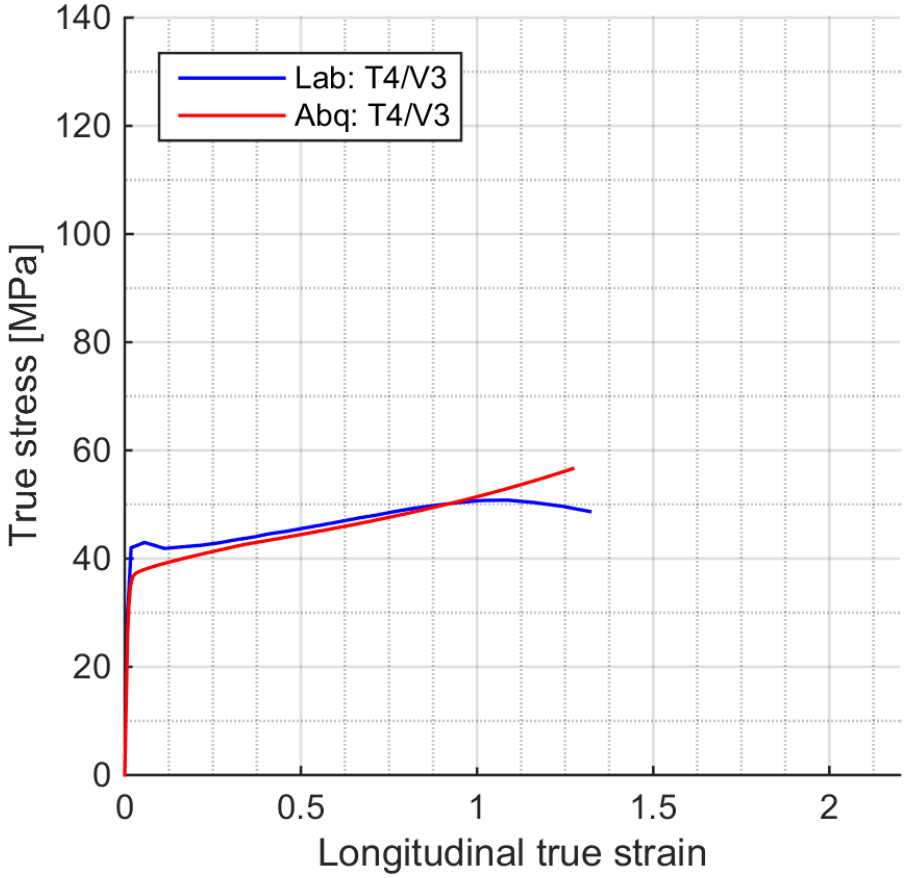
Lab: T4/V3
Abq: T4/V3
True stress [MPa]
Longitudinal true strain
0
20
40
60
80
100
120
140
0
0.5
1
1.5
2

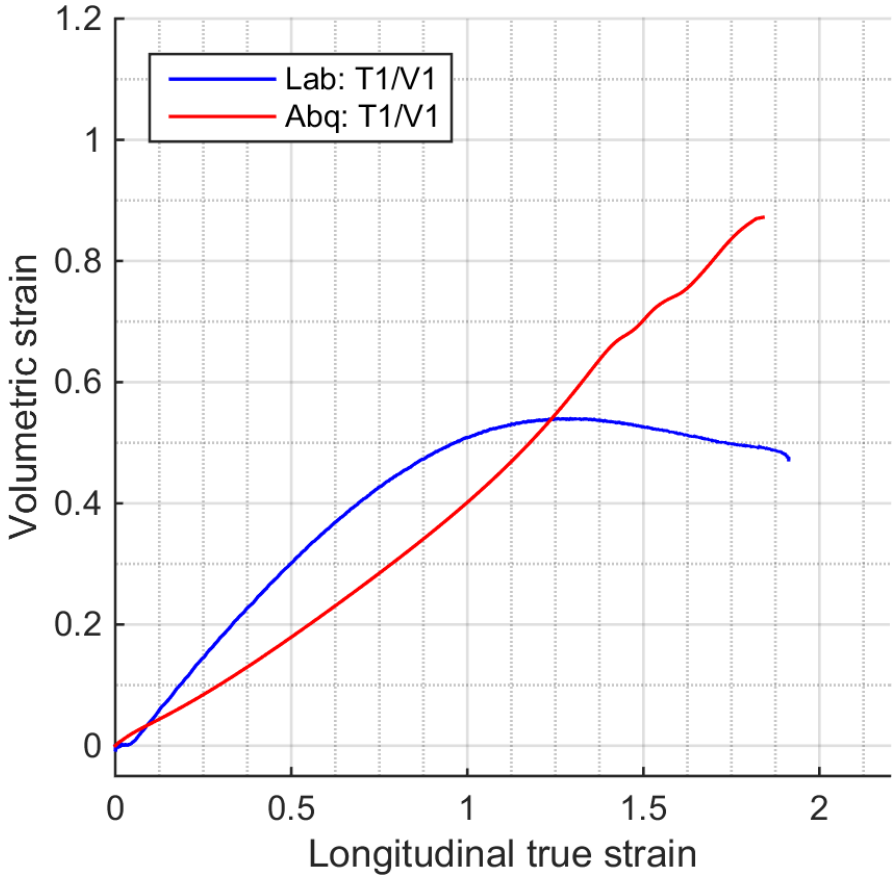
Lab: T1/V1
Abq: T1/V1
Volumetric strain
Longitudinal true strain
0
0.2
0.4
0.6
0.8
1
1.2
0.5
1.5
2

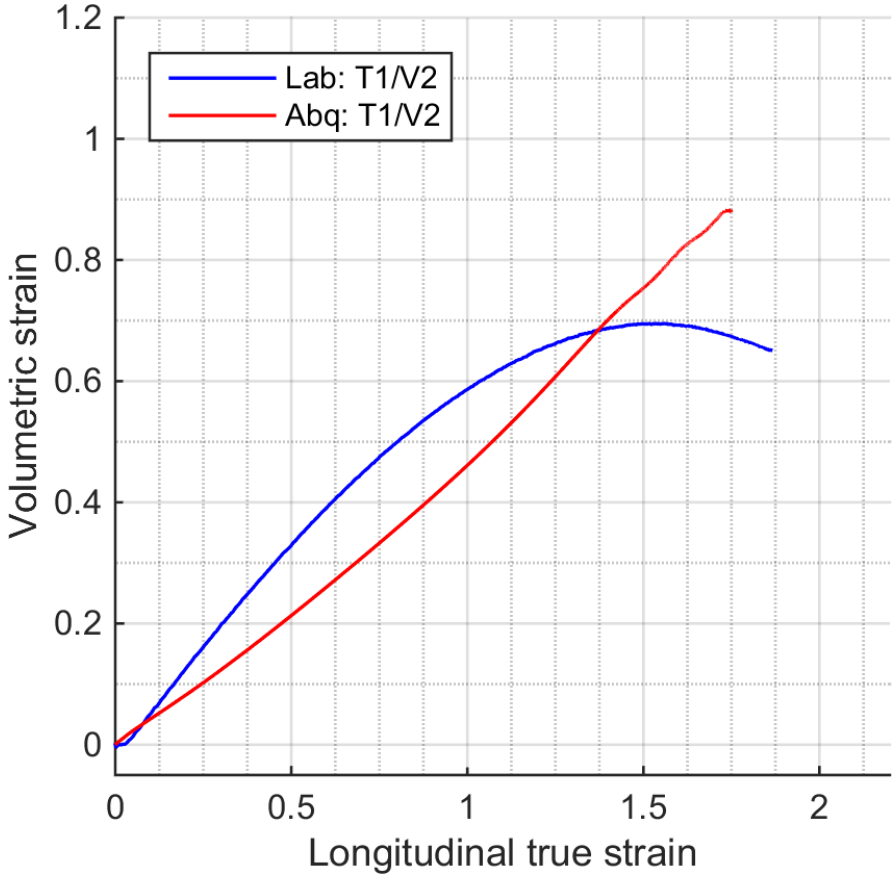
Lab: T1/V2
Abq: T1/V2
Volumetric strain
Longitudinal true strain
0
0.2
0.4
0.6
0.8
1
1.2
0.5
1.5
2

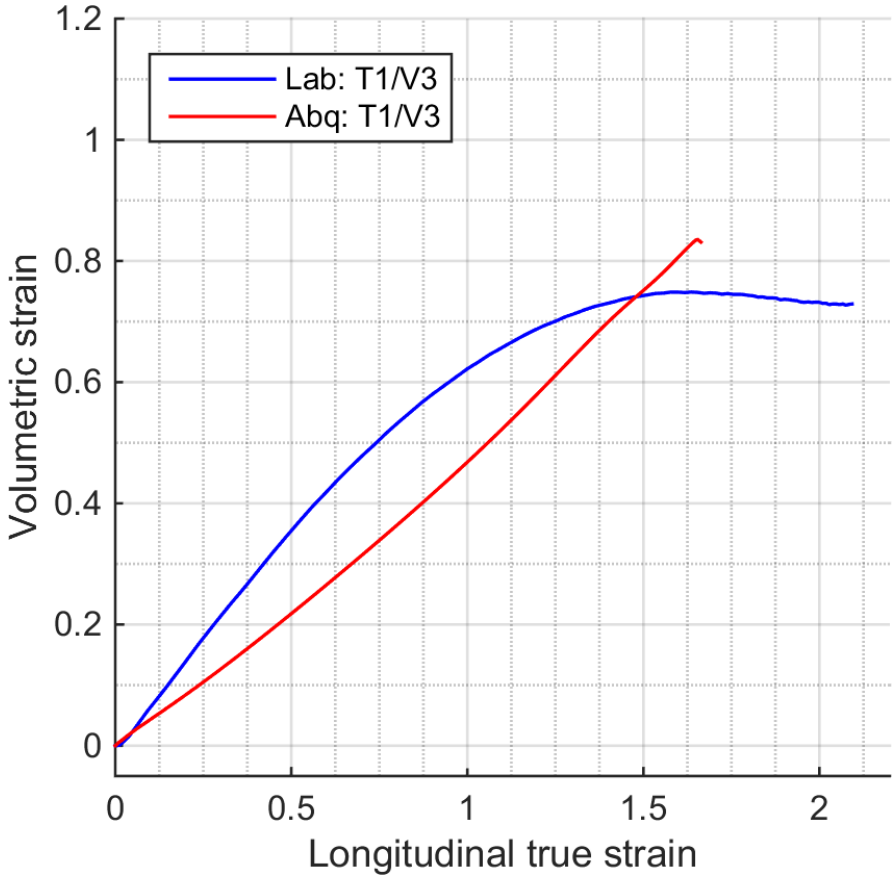
Lab: T1/V3
Abq: T1/V3
Volumetric strain
Longitudinal true strain
0
0.2
0.4
0.6
0.8
1
1.2
0.5
1.5
2

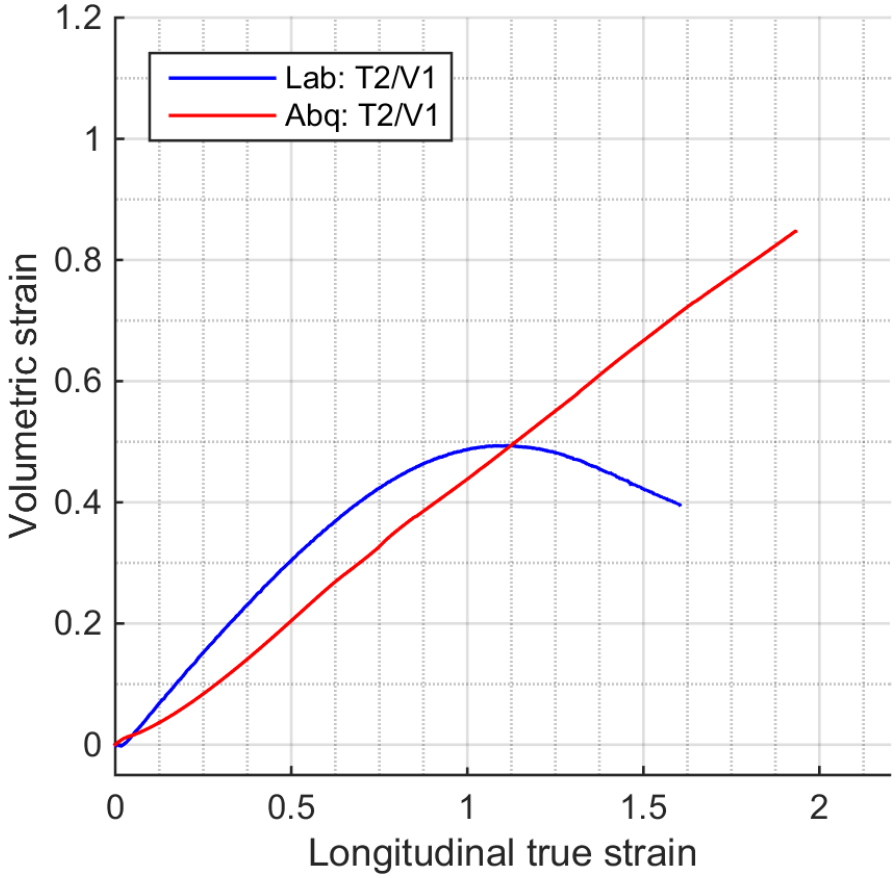
Lab: T2/V1
Abq: T2/V1
Volumetric strain
Longitudinal true strain
0
0.2
0.4
0.6
0.8
1
1.2
0.5
1.5
2

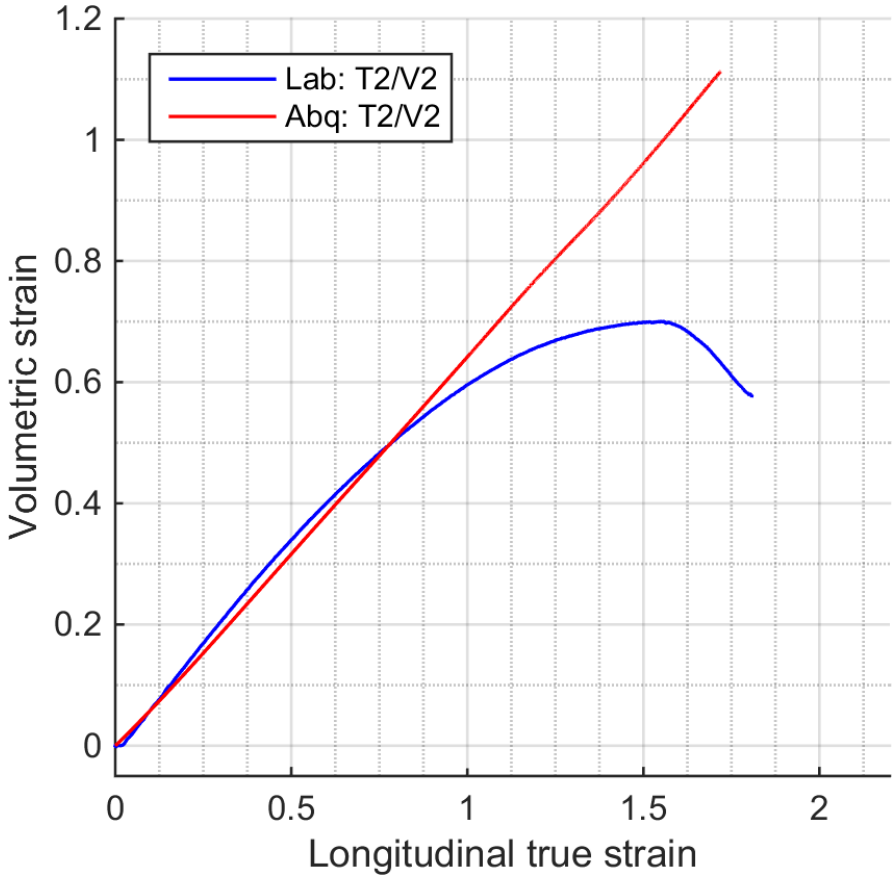
Lab: T2/V2
Abq: T2/V2
Volumetric strain
Longitudinal true strain
0
0.2
0.4
0.6
0.8
1
1.2
0
0.5
1
1.5
2

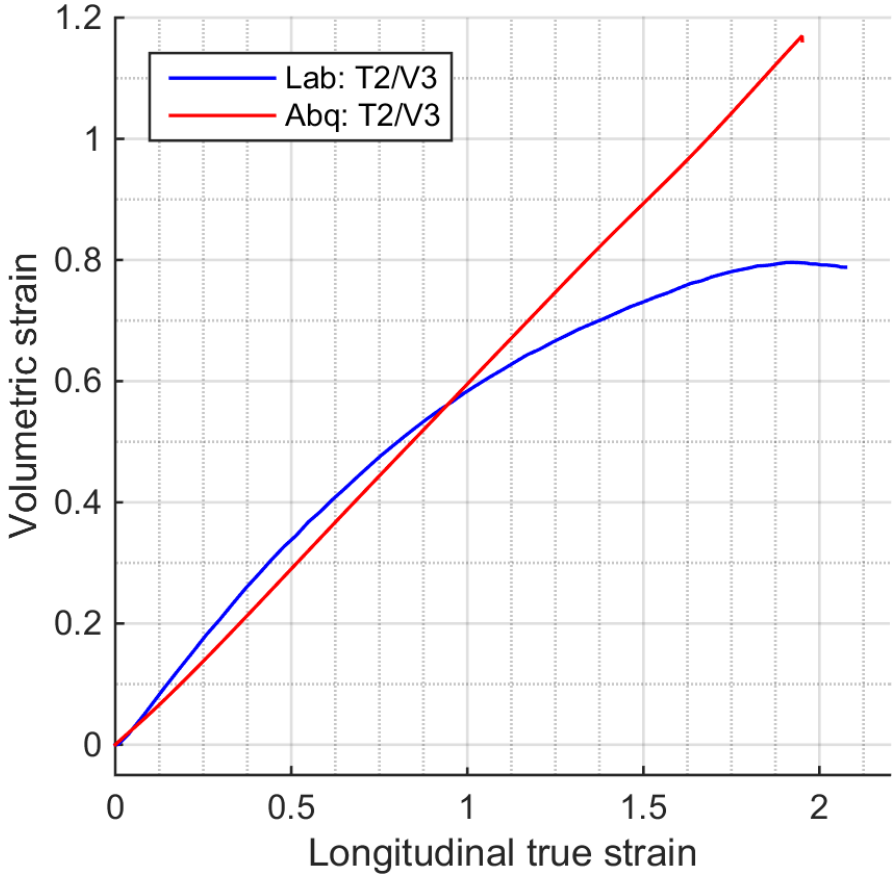
Lab: T2/V3
Abq: T2/V3
Volumetric strain
Longitudinal true strain
0
0.2
0.4
0.6
0.8
1
1.2
0
0.5
1
1.5
2

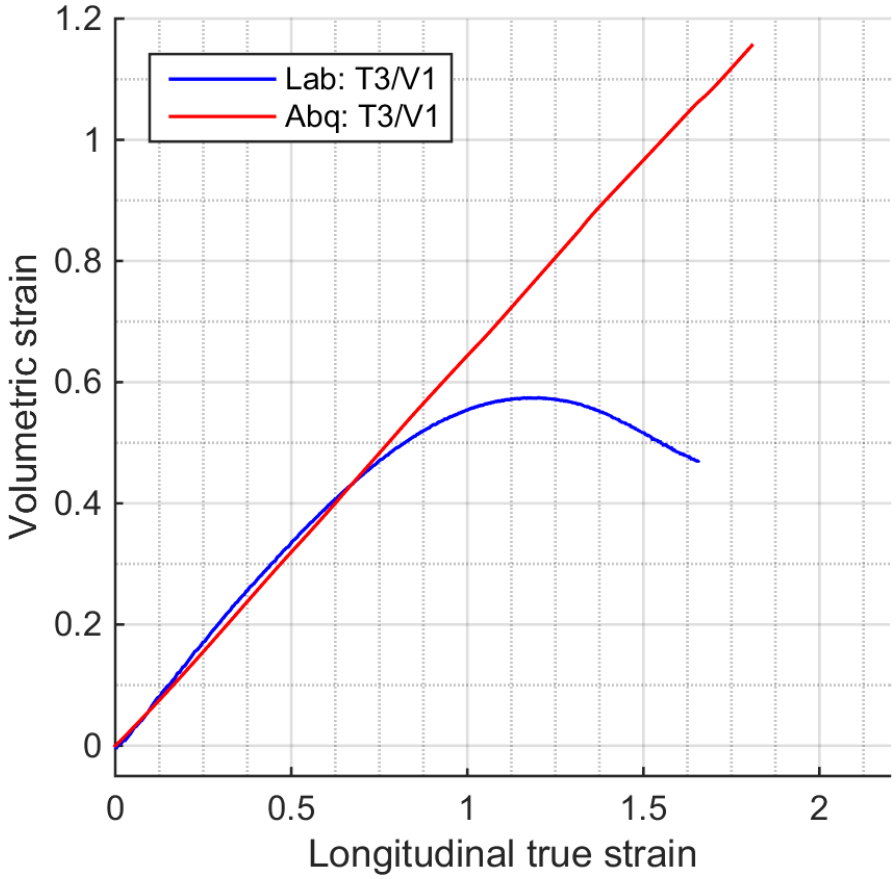
Lab: T3/V1
Abq: T3/V1
Volumetric strain
Longitudinal true strain
0
0.2
0.4
0.6
0.8
1
1.2
0
0.5
1
1.5
2

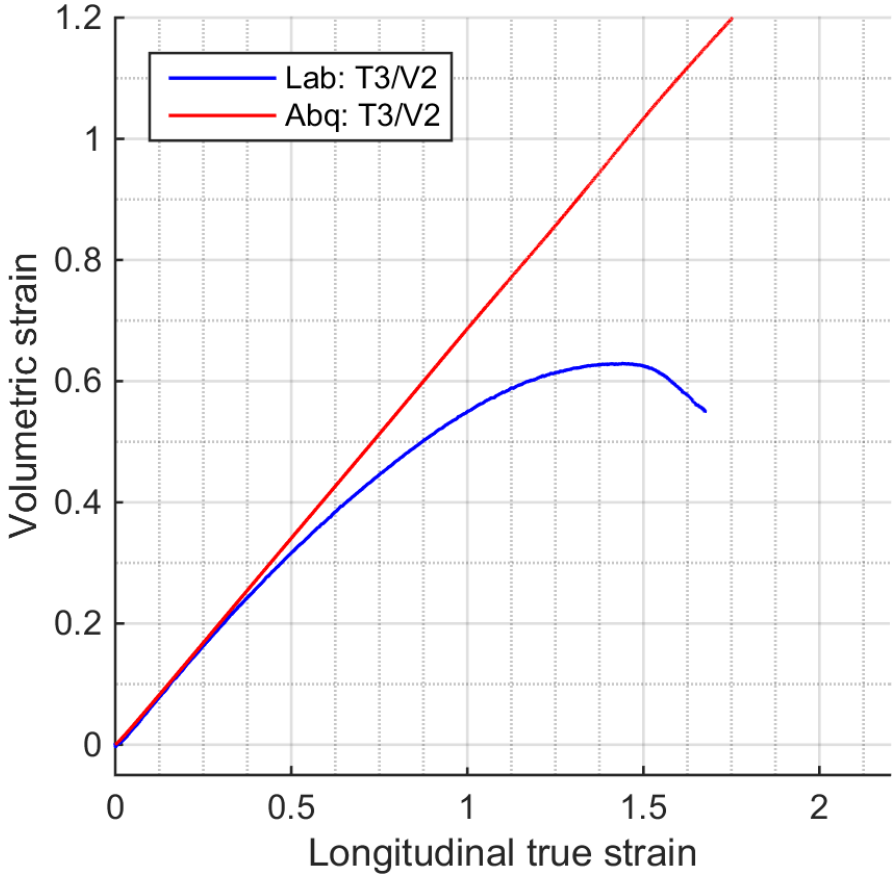
Lab: T3/V2
Abq: T3/V2
Volumetric strain
Longitudinal true strain
0
0.2
0.4
0.6
0.8
1
1.2
0
0.5
1
1.5
2

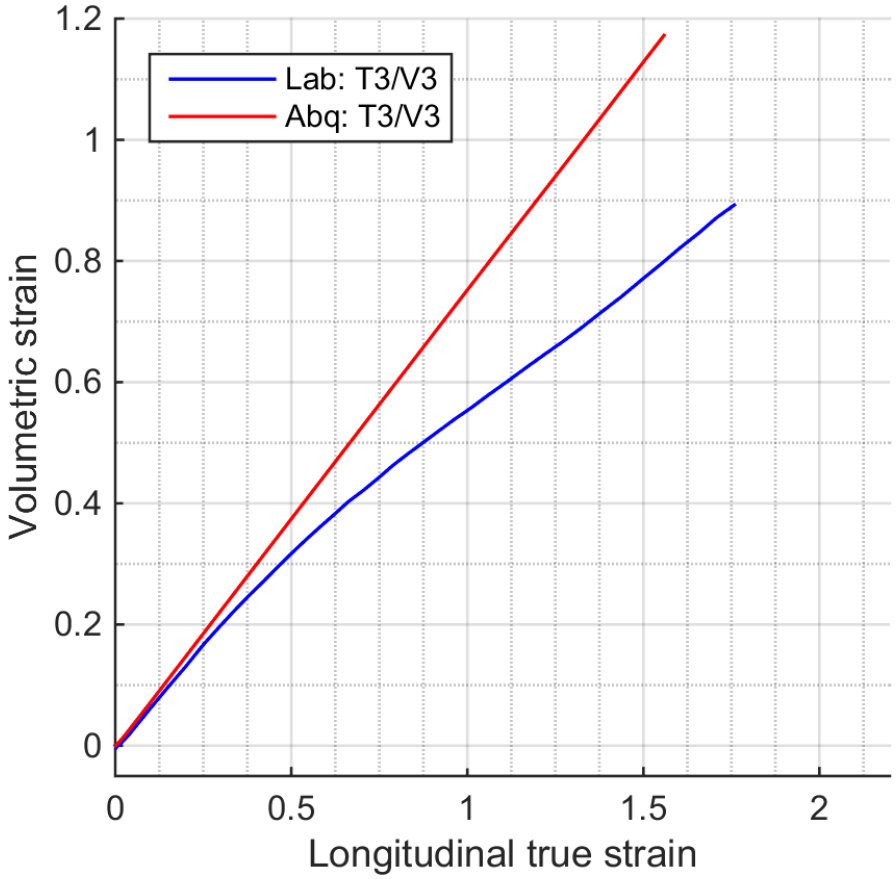
Lab: T3/V3
Abq: T3/V3
Volumetric strain
Longitudinal true strain
0
0.2
0.4
0.6
0.8
1
1.2
0
0.5
1
1.5
2

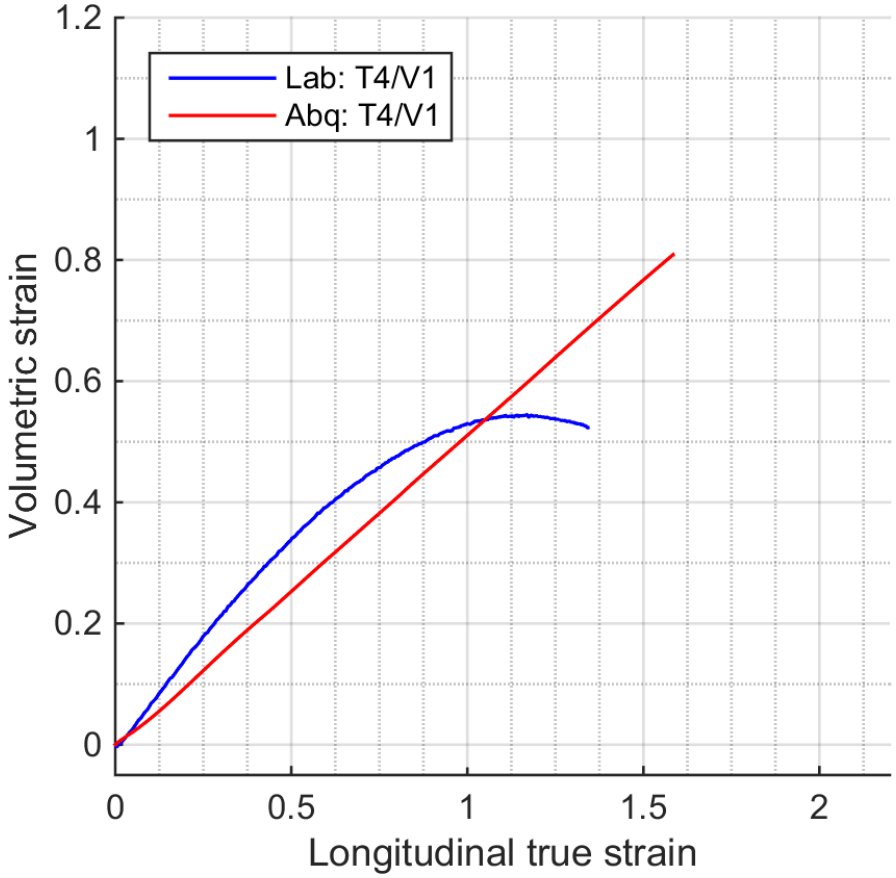
Lab: T4/V1
Abq: T4/V1
Volumetric strain
Longitudinal true strain
0
0.2
0.4
0.6
0.8
1
1.2
0
0.5
1
1.5
2

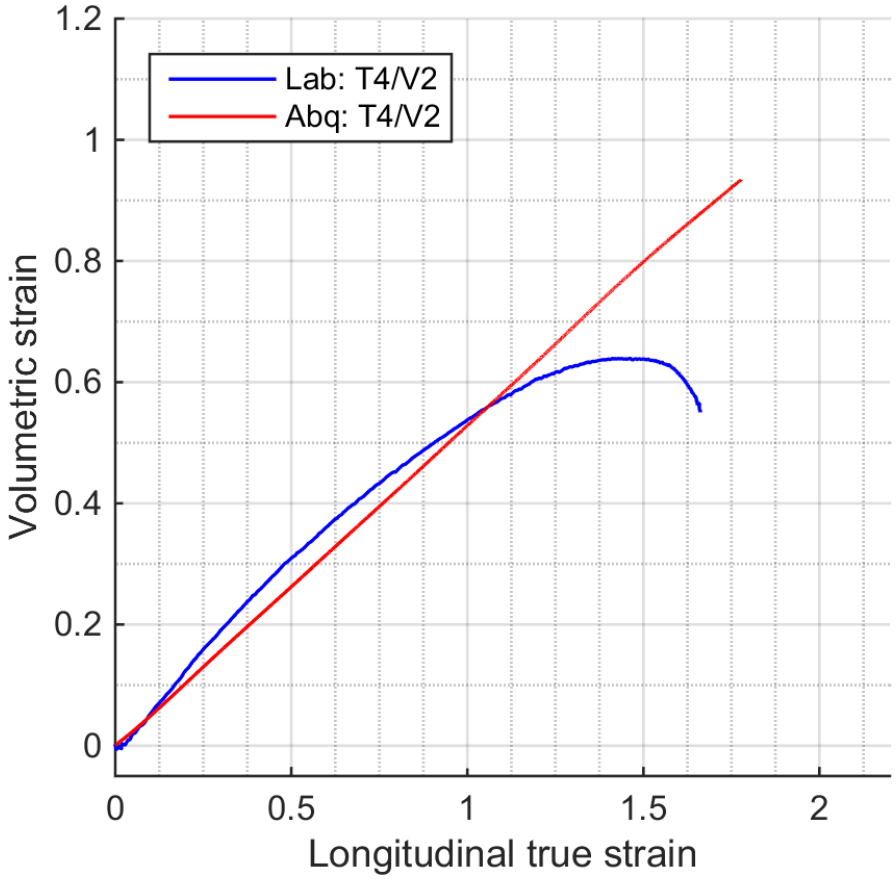
Lab: T4/V2
Abq: T4/V2
Volumetric strain
Longitudinal true strain
0
0.2
0.4
0.6
0.8
1
1.2
0
0.5
1
1.5
2

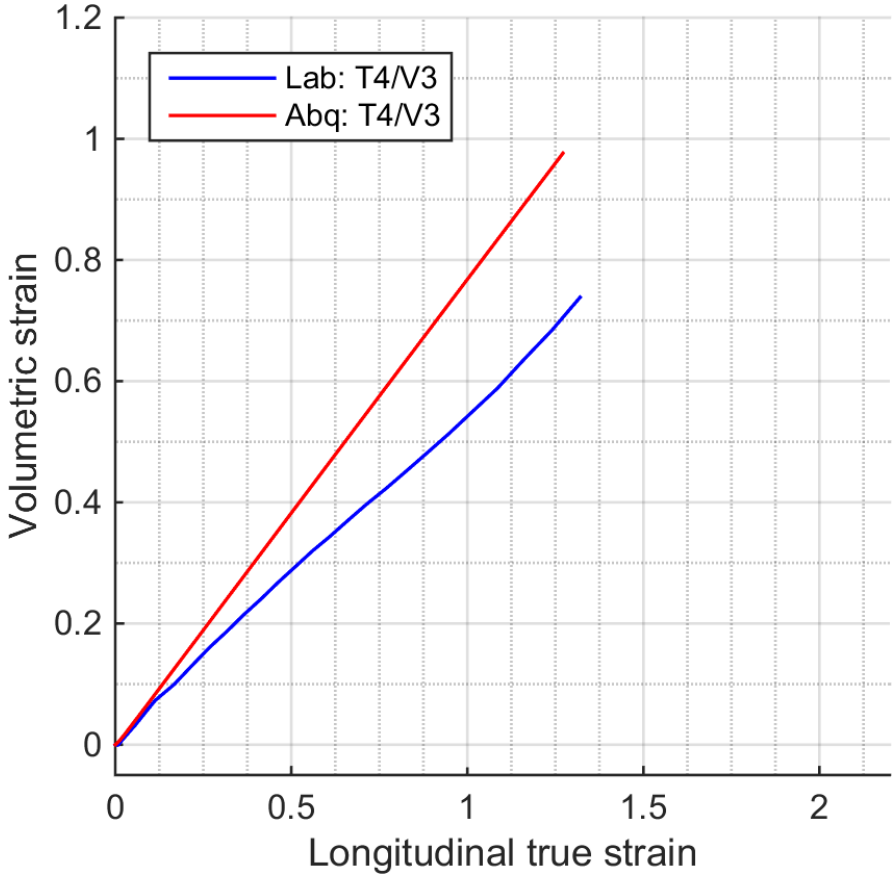
Lab: T4/V3
Abq: T4/V3
Volumetric strain
Longitudinal true strain
0
0.2
0.4
0.6
0.8
1
1.2
0
0.5
1
1.5
2